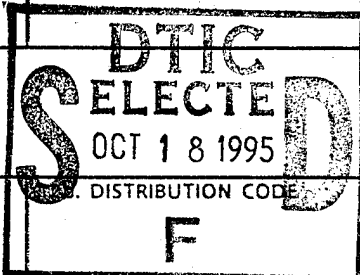
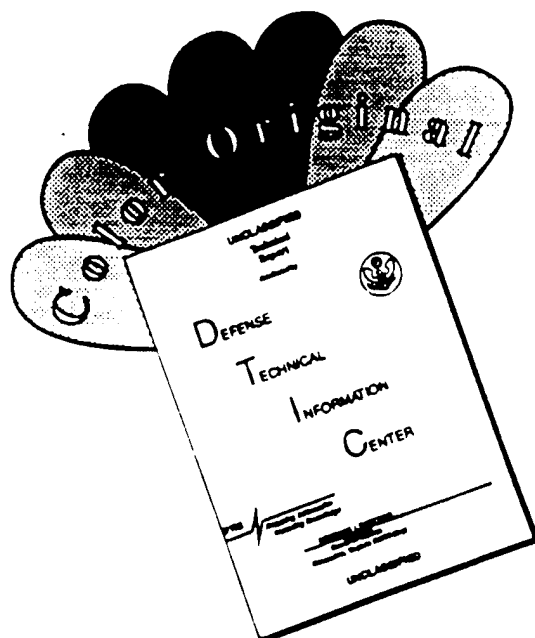


REPORT DOCUMENTATION PAGE			Form Approved OMB No. 0704-0188	
Public reporting burden for this collection of information is estimated to average 1 hour per response, including the time for reviewing instructions, searching existing data sources, gathering and maintaining the data needed, and completing and reviewing the collection of information. Send comments regarding this burden estimate or any other aspect of this collection of information, including suggestions for reducing this burden, to Washington Headquarters Services, Directorate for Information Operations and Reports, 1215 Jefferson Davis Highway, Suite 1204, Arlington, VA 22202-4302, and to the Office of Management and Budget, Paperwork Reduction Project (0704-0188), Washington, DC 20503.				
1. AGENCY USE ONLY (Leave blank)		2. REPORT DATE 10 Sep 95		3. REPORT TYPE AND DATES COVERED
4. TITLE AND SUBTITLE Statistics for the Global Applicability of Retrieval Algorithms for Geophysical Parameters Using The SSM/I			5. FUNDING NUMBERS	
6. AUTHOR(S) John Francis Polander				
7. PERFORMING ORGANIZATION NAME(S) AND ADDRESS(ES) AFIT Students Attending: Texas A&M University			8. PERFORMING ORGANIZATION REPORT NUMBER 95-089	
9. SPONSORING/MONITORING AGENCY NAME(S) AND ADDRESS(ES) DEPARTMENT OF THE AIR FORCE AFIT/CI 2950 P STREET, BLDG 125 WRIGHT-PATTERSON AFB OH 45433-7765			10. SPONSORING/MONITORING AGENCY REPORT NUMBER	
11. SUPPLEMENTARY NOTES				
12a. DISTRIBUTION/AVAILABILITY STATEMENT Approved for Public Release IAW AFR 190-1 Distribution Unlimited BRIAN D. GAUTHIER, MSgt, USAF Chief of Administration				
13. ABSTRACT (Maximum 200 words) <p>"Original contains color plates: All DTIC reproductions will be in black and white"</p> <p>19951017 147</p> <p>DTIC QUALITY INSPECTED 8</p>				
14. SUBJECT TERMS			15. NUMBER OF PAGES 91	
			16. PRICE CODE	
17. SECURITY CLASSIFICATION OF REPORT	18. SECURITY CLASSIFICATION OF THIS PAGE	19. SECURITY CLASSIFICATION OF ABSTRACT	20. LIMITATION OF ABSTRACT	

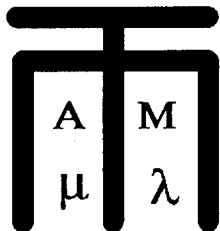
DISCLAIMER NOTICE



THIS DOCUMENT IS BEST QUALITY AVAILABLE. THE COPY FURNISHED TO DTIC CONTAINED A SIGNIFICANT NUMBER OF COLOR PAGES WHICH DO NOT REPRODUCE LEGIBLY ON BLACK AND WHITE MICROFICHE.

TEXAS A&M UNIVERSITY

**DEPARTMENT OF
METEOROLOGY**



MICROWAVE REMOTE SENSING GROUP

**STATISTICS FOR THE GLOBAL APPLICABILITY OF
RETRIEVAL ALGORITHMS FOR
GEOPHYSICAL PARAMETERS USING THE SSM/I**

A Thesis

by

JOHN FRANCIS POLANDER

**STATISTICS FOR THE GLOBAL APPLICABILITY OF
RETRIEVAL ALGORITHMS FOR GEOPHYSICAL
PARAMETERS USING THE SSM/I**

A Thesis

by

JOHN FRANCIS POLANDER

Submitted to the Office of Graduate Studies of
Texas A&M University
in partial fulfillment of the requirements for the degree of

MASTER OF SCIENCE

Accession For	
NTIS CRA&I	<input checked="checked" type="checkbox"/>
DTIC TAB	<input type="checkbox"/>
Unannounced	<input type="checkbox"/>
Justification	
By	
Distribution /	
Availability Codes	
Dist	Avail and/or Special
A-1	

August 1995

Major Subject: Meteorology

STATISTICS FOR THE GLOBAL APPLICABILITY OF
RETRIEVAL ALGORITHMS FOR GEOPHYSICAL
PARAMETERS USING THE SSM/I

A Thesis

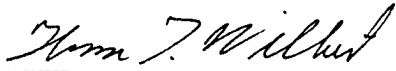
by

JOHN FRANCIS POLANDER

Submitted to Texas A&M University
in partial fulfillment of the requirements
for the degree of

MASTER OF SCIENCE

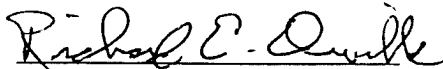
Approved as to style and content by:



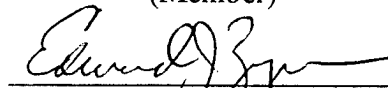
Thomas T. Wilheit
(Chair of Committee)



William H. Bassichis
(Member)



Richard E. Orville
(Member)



Edward J. Zipser
(Head of Department)

August 1995

Major Subject: Meteorology

ABSTRACT

Statistics for the Global Applicability of Retrieval Algorithms
for Geophysical Parameters Using the SSM/I. (August 1995)

John Francis Polander, B.S., Texas A&M University

Chair of Advisory Committee: Dr. Thomas T. Wilheit

Brightness temperatures (T_B), measured by the SSM/I (Special Sensor Microwave Imager) at 85.5 GHz (vertical and horizontal polarization) during August - November 1987 and January - March 1993, are examined over the Earth's oceans between 60° N and 60° S. Collected data are placed into regions of dimension 5° latitude by 5° longitude. For each region, an absorption and scattering regime is identified based upon the frequency of occurrence between the average brightness temperature $((T_{B85V} + T_{B85H})/2)$ and the polarization difference $(T_{B85V} - T_{B85H})$. A global distribution of sensitivities is then constructed which allows us to determine how often our new and improved algorithms can be used for computing various geophysical parameters: cloud liquid water (CLW), precipitable water (PW), sea surface temperature (SST), and sea surface wind speed (WS). Results indicate the algorithms can be applied 75-90 % of the time over the majority of the Earth's oceans. These algorithms will serve as a simulation study for the performance of the Multi-frequency Imaging Microwave Radiometer (MIMR) which is scheduled for launch in the year 2000.

Additionally, a quantitative assessment of CLW distributions for nonprecipitating clouds is presented over selected oceanic regions. This gives insight into the amount and variability of CLW present in clouds within the radiometer's field of view. The results indicate little variability in subtropical regions with a median value around .05 kg/m². Increased variability and higher

median values (.07-.11 kg/ m²) are characteristic of the remaining oceanic regions. The only exceptions are along the ITCZ, SPCZ, and monsoon regions, where frequent precipitation and dense clouds render the atmosphere sufficiently opaque, leading to unreliable results.

ACKNOWLEDGMENTS

I want to thank Dr. Wilheit for his constant support and technical guidance throughout my entire study. His ability and willingness to review and critique my work in a timely manner proved critical to my successfully completing all phases of research required for my degree. I also thank Dr. Orville for sharing his time and suggestions, many of which have been incorporated into this final product. I also thank Dr. Bassichis for his time, support, and encouragement of this 'black hat'.

I am indebted to many members of the Microwave Remote Sensing Group. Special thanks to Ye Hong and Jeff Tesmer who were both instrumental in assisting me with learning how to program in C. I owe many thanks to David Kohn and Clay Blankenship for their ideas and suggestions, especially during the initial phases of my research when just getting started seemed an impossible task. Alex Wang and other members were always there to answer any questions that arose on the spot.

Finally, my deepest and warmest gratitude to my wife, Cindy, and daughters, Emily and Ellyn, for their total understanding and complete faith in me through all my ordeals.

Funding for my education and the bulk of my research was provided by the United States Air Force. Partial funding was provided by NASA, contract number NAS5-3259.

TABLE OF CONTENTS

CHAPTER	Page
I INTRODUCTION AND BACKGROUND.....	1
1. Introduction.....	1
2. SSM/I and MIMR descriptions.....	3
3. Previous work.....	7
4. Research objectives.....	11
II DATA.....	12
III ABSORPTION VS. SCATTERING OVER THE OCEANS.....	14
1. The absorption branch.....	14
2. The scattering branch.....	16
3. Separation of the branches.....	17
4. Physical justification for branch separation method.....	22
IV GLOBAL SENSITIVITY STUDY.....	30
1. Sensitivity percentile thresholds.....	30
2. Global sensitivity distributions.....	31
V REGIONAL SENSITIVITY STUDY.....	51
1. Enlarging the T_B 85 GHz FOV.....	51
2. Effects of enlarging the FOV.....	57
VI DISTRIBUTION OF CLOUD LIQUID WATER.....	76
1. Multi-frequency retrieval algorithm.....	76
2. Regional cloud liquid water distributions.....	76
VII CONCLUSIONS AND RECOMMENDATIONS.....	82
1. Sensitivity distribution results.....	83
2. Cloud liquid water distribution results.....	84
3. Recommendations for future work.....	84
REFERENCES.....	87

APPENDIX	Page
A SCHEMATIC OF THE SSM/T'S CHANNEL\FREQUENCY POLARIZATIONS.....	89
B LIST OF ACRONYMS.....	90
VITA.....	91

LIST OF TABLES

TABLE	Page
1. Intercomparison of MIMR and SSM/I performance.....	6
2. Dynamic temperature range necessary for application of physical model to statistics.....	29
3. 4 - parameter algorithm sensitivities as a function of polarization difference.....	52
4. Typical global cloud liquid water values.....	85

LIST OF FIGURES

FIGURE	Page
1. SSM/I-observed average brightness temperature vs. polarization at 85 GHz for August 1987 - ITCZ box	10
2. Ocean surface reflectivity as a function of incidence angle and polarization for 85 GHz and surface temperature of 288 K.....	15
3. Result of applying branch separation method to figure 1.....	18
4. SSM/I-observed average brightness temperature vs. polarization at 85 GHz for August 1987 - midlatitude box.....	20
5. SSM/I-observed average brightness temperature vs. polarization at 85 GHz for August 1987 - subtropical high box.....	21
6. SSM/I-observed average brightness temperature vs. polarization at 85 GHz for February 1993 - Hudson Bay region.....	23
7. Two-component (single layer atmosphere and surface) radiative transfer model (a) and effects on brightness temperatures as a result of varying optical depth (τ) (b).....	24
8. Intercomparison of the physical model and the statistical method to identify the absorption branch of a February 1993, ITCZ box.....	26
9. Intercomparison of the physical model and the statistical method to identify the absorption branch of a February 1993, midlatitude box.....	27
10. Global sensitivity map depicting 85 GHz polarization difference values for August 1987 at the 10th percentile threshold.....	32
11. Global sensitivity map depicting 85 GHz polarization difference values for August 1987 at the 50th percentile threshold.....	33
12. Global sensitivity map depicting 85 GHz polarization difference values for August 1987 at the 75th percentile threshold.....	34
13. Global sensitivity map depicting 85 GHz polarization difference values for August 1987 at the 90th percentile threshold.....	35

FIGURE	Page
14. Statistics displaying the latitudinal variability of the sensitivity distributions for August 1987 at the 10th (top) and 50th percentile (bottom) thresholds.....	38
15. Statistics displaying the latitudinal variability of the sensitivity distributions for August 1987 at the 75th (top) and 90th percentile (bottom) thresholds.....	39
16. Intercomparison of the global sensitivity distributions at the 10th percentile threshold for August 1987 (top) and February 1993 (bottom).....	41
17. Intercomparison of the global sensitivity distributions at the 50th percentile threshold for August 1987 (top) and February 1993 (bottom).....	42
18. Intercomparison of the global sensitivity distributions at the 75th percentile threshold for August 1987 (top) and February 1993 (bottom).....	43
19. Intercomparison of the global sensitivity distributions at the 90th percentile threshold for August 1987 (top) and February 1993 (bottom).....	44
20. Statistics comparing the latitudinal variability of the sensitivity distributions for August 1987 (top) and February 1993 (bottom) at the 10th percentile threshold.....	45
21. Statistics comparing the latitudinal variability of the sensitivity distributions for August 1987 (top) and February 1993 (bottom) at the 50th percentile threshold.....	46
22. Statistics comparing the latitudinal variability of the sensitivity distributions for August 1987 (top) and February 1993 (bottom) at the 75th percentile threshold.....	47
23. Statistics comparing the latitudinal variability of the sensitivity distributions for August 1987 (top) and February 1993 (bottom) at the 90th percentile threshold.....	48

FIGURE	Page
24. Simplified scan geometry of the SSM/I with relative FOV's for 37 and 85 GHz	54
25. Simplified scan geometry of the SSM/I with relative FOV's for 22 and 85 GHz	55
26. Simplified scan geometry of the SSM/I with relative FOV's for 6, 10, 19 and 85 GHz	56
27. Global sensitivity maps depicting groups of 4, T_B 85 GHz observations and their resulting polarization difference values at the 10th (top) and 50th percentile (bottom) thresholds for August 1987.....	58
28. Global sensitivity maps depicting groups of 4, T_B 85 GHz observations and their resulting polarization difference values at the 75th (top) and 90th (bottom) percentile thresholds for August 1987.....	59
29. Global sensitivity maps depicting groups of 16, T_B 85 GHz observations and their resulting polarization difference values at the 10th (top) and 50th (bottom) percentile thresholds for August 1987.....	60
30. Global sensitivity maps depicting groups of 16, T_B 85 GHz observations and their resulting polarization difference values at the 75th (top) and 90th (bottom) percentile thresholds for August 1987.....	61
31. Global sensitivity maps depicting groups of 64, T_B 85 GHz observations and their resulting polarization difference values at the 10th (top) and 50th (bottom) percentile thresholds for August 1987.....	62
32. Global sensitivity maps depicting groups of 64, T_B 85 GHz observations and their resulting polarization difference values at the 75th (top) and 90th (bottom) percentile thresholds for August 1987.....	63

FIGURE	Page
33. Latitudinal variability of the T_B 85 GHz polarization differences at the 10th percentile threshold for August 1987 (all T_B 85 observations (top) and groups of 4 (bottom)).....	65
34. Latitudinal variability of the T_B 85 GHz polarization differences at the 10th percentile threshold for August 1987 (groups of 16 (top) and 64 observations (bottom)).....	66
35. Latitudinal variability of the T_B 85 GHz polarization differences at the 50th percentile threshold for August 1987 (all T_B 85 observations (top) and groups of 4 (bottom)).....	67
36. Latitudinal variability of the T_B 85 GHz polarization differences at the 50th percentile threshold for August 1987 (groups of 16 (top) and 64 observations (bottom)).....	68
37. Latitudinal variability of the T_B 85 GHz polarization differences at the 75th percentile threshold for August 1987 (all T_B 85 observations (top) and groups of 4 (bottom)).....	69
38. Latitudinal variability of the T_B 85 GHz polarization differences at the 75th percentile threshold for August 1987 (groups of 16 (top) and 64 observations (bottom)).....	70
39. Latitudinal variability of the T_B 85 GHz polarization differences at the 90th percentile threshold for August 1987 (all T_B 85 observations (top) and groups of 4 (bottom)).....	71
40. Latitudinal variability of the T_B 85 GHz polarization differences at the 90th percentile threshold for August 1987 (groups of 16 (top) and 64 observations (bottom)).....	72
41. Regional analysis comparing resolution effects on sensitivity distributions as a function of climate regime.....	74
42. Regional cloud liquid water distributions (amount of CLW vs. percent of time found) in a high latitude box (top) and midlatitude box (bottom) in August 1987.....	78

FIGURE	Page
43. Regional cloud liquid water distributions (amount of CLW vs. percent of time found) in a subtropical high box (top) and a tropical box (bottom) in August 1987.....	79

CHAPTER I

INTRODUCTION AND BACKGROUND

1. Introduction

Water vapor and liquid water are strong absorbers and emitters of radiation. Ice, on the other hand, can be a strong scatterer of electromagnetic energy in the visible and microwave wavelengths. Ice also absorbs and emits radiation in the infrared spectrum. Gunn and East (1954) demonstrated the dominance of scattering versus absorption of radiation by ice particles at a given wavelength. The theory works well and is relatively simple for Rayleigh scatterers when $r_{ice} \ll \lambda$, where r_{ice} is the radius of ice particles and λ is the wavelength. Such is the case for 85.5 GHz. It is also applicable when $r_{ice} > \lambda$, which includes the Mie scattering regime and geometric optics. In those instances, the mathematical computations become somewhat more cumbersome, but the principal results are unchanged.

With the advent of computer and space age technology, research scientists are now capable of retrieving vast quantities of data from satellites carrying radiometric instruments such as the Special Sensor Microwave/Imager (SSM/I). These instruments utilize passive remote sensing as a means of measuring the upwelling radiation from the Earth's surface and atmosphere and relating it in terms of brightness temperatures (T_B). In particular, microwave radiometry provides information in almost all types of weather regimes as opposed to infrared and visible (Filiberti et al. 1994). Because microwave radiation is absorbed 10 to 100 times more by liquid water clouds than by ice clouds, we can deduce cloud liquid water content assuming the effects of water vapor are taken into account (Alishouse et al.

1990).

The primary focus of this study is to determine how often and over how much of the Earth's ocean surface we will be able to accurately measure various geophysical parameters using the Multi-frequency Imaging Microwave Radiometer (MIMR). These parameters include sea surface temperature (SST), surface wind speed (WS), cloud liquid water (CLW), and precipitable water (PW) sometimes referred to as columnar water vapor or total integrated water vapor.

Obtaining accurate retrievals of SST, WS, CLW, and PW is extremely important since conventional observations over the oceans are very sparse and in most places nonexistent. Passive microwave radiometry provides the means to access data from otherwise inaccessible oceanic regions.

The major drawback to obtaining accurate retrievals occurs in the presence of precipitation. Regions containing significant precipitation or dense clouds render the retrievals unreliable (Goodberlet et al. 1989). Conversely, in the presence of thin clouds or clear skies, the retrievals can be made to produce better results (Nelkin 1992). Therefore, the elimination of data associated with rain and knowing where the clouds are thin are of prime importance and somewhat problematic.

To solve this problem, a filter is created based on 85-90 GHz polarization differences ($T_{B85V} - T_{B85H}$) to eliminate observations which likely contain rain and, if desired, excessively thick clouds. The remaining observations are associated with a range of atmospheric opacities which are described in terms of their 85 GHz polarization differences. A large ΔT_B (typically > 25 K) indicates a relatively clear atmosphere (thin or no clouds) while a small ΔT_B (< 10 K) is associated with a nearly opaque atmosphere (thick clouds and possible rain).

The filter is also used to select algorithms and to determine how often the more sensitive algorithms, for a given parameter, can be used. For example, selecting an algorithm to retrieve the value of a specific parameter (i.e. SST) involves several steps. First, all the 85-90 GHz observations, within the radiometer's lowest frequency channel (6.8 GHz in this example) field of view (FOV), are collected. Then, the pair

(T_{B85V} , T_{B85H}) of observations with the smallest ΔT_B in that FOV is identified. This pair is associated with the most problematic part of the FOV: the region with the most opaque atmosphere.

After identifying the pair of observations with the smallest ΔT_B , an algorithm can be selected that is consistent with this ΔT_B value. Specifically, this will be the most sensitive algorithm than can be safely used while remaining compatible with the most opaque portion of the atmosphere within the FOV.

Finally, some understanding can be gained regarding the ΔT_B distributions in terms of the amount and distribution of cloud liquid water in nonprecipitating clouds.

2. SSM/I and MIMR descriptions

The first launch of the SSM/I (July 1987) was aboard the Defense Meteorological Satellite Program (DMSP) satellite designated F-8. Three additional instruments are currently in operation on DMSP satellites designated F-10, F-11, and F-13. A fifth SSM/I aboard the recently launched DMSP F-12 platform will soon provide additional data. However, technical difficulties are currently precluding it from operational use.

The SSM/I's operate in a near-polar, sun-synchronous, circular orbit at an altitude of 833 km. Their orbital inclination is 98.8° (i.e., 81.2° retrograde) with an orbital period of 102 minutes. The conical scan from the SSM/I covers a swath of approximately 1400 km. Depending on the frequency, the instantaneous spatial resolution varies from 69×43 km at 19.35 GHz to 15×13 km at 85.5 GHz.

The SSM/I measures the upwelling radiation from the Earth's surface and atmosphere. If scattering is not considered and horizontal homogeneity is assumed then by integrating the Equation of Radiative Transfer (ERT) and using the Rayleigh-Jeans approximation, a brightness temperature (T_B) can be expressed as:

$$\begin{aligned}
T_B = & \underbrace{\int_0^{\infty} T(h) e^{-\tau(h,\infty)} \gamma(h) \frac{dh}{\cos(\theta)}}_{(A)} + \underbrace{(1-r) e^{-\tau(0,\infty)} T_s}_{(B)} \\
& + \underbrace{r e^{-\tau(0,\infty)} \int_0^{\infty} T(h) e^{-\tau(0,h)} \gamma(h) \frac{dh}{\cos(\theta)}}_{(C)} + \underbrace{r e^{-2\tau(0,\infty)} T_{cb}}_{(D)}
\end{aligned}$$

where

$$\tau(a, b) \equiv \int_a^b \gamma(h') \frac{dh'}{\cos(\theta)}$$

T_B is the brightness temperature measured by the SSM/I and exiting the atmosphere at the incidence angle θ (average of 53.1° for the SSM/I). $T(h)$ and $\gamma(h)$ are the thermometric temperature and absorption coefficient at height h . The reflectivity and earth's surface temperature are r and T_s , respectively. Applying a derivation of Kirchoff's Law (reflectivity (r_λ) + emissivity (ϵ_λ) = 1), the quantity $(1-r)$ denotes the surface emissivity while T_{cb} is the brightness temperature of the cosmic background (2.7 K). The absorption coefficient (γ) times the layer thickness is the optical depth (τ) between points a and b .

Term A denotes the upwelling radiation from each incremental atmospheric layer and attenuated by intervening layers. Term B denotes the surface emission attenuated by the atmosphere. Terms C and D result from the radiation reflected off the surface. Term C denotes the downwelling emission attenuated by the segment of the atmosphere between the emitting layer and the surface and by the entire atmosphere on the way back up to the sensor. Term D denotes the attenuation of the cosmic background (2.7 K) from its downward and upward pass through the atmosphere and reflection off the surface (Wilheit et al. 1994).

The SSM/I is a passive microwave radiometer which measures brightness temperatures at four frequencies: 19.35, 22.235, 37.0, and 85.5 GHz in both horizontal

(H) and vertical (V) polarization (from this point on, frequencies and their polarizations will be referred to by their integer value followed by a "V" or "H" if applicable). The exception is at 22 GHz where only the vertical polarization is measured. This totals seven separate channels.

The SSM/I spins about the vertical axis with a rotation period of 1.9 seconds. Observations are taken in a 102.4° portion of the rotation with the SSM/I pointed in the aft direction aboard the F8 satellite (forward direction for all others). The 102.4° arc is centered on the satellite subtrack and covers a 1394 km wide swath given an orbital height of 833 km. During each scan, within the 102.4° arc, both 85 GHz channels are sampled 128 times. The distance between samples along and between scans is approximately 12.5 km. The integration period for a single sample is 3.89 ms. This results in the 85 GHz channels having, at the Earth's surface, an effective resolution of approximately 15 km.

The channels at the lower three frequencies (19, 22, 37) are sampled every other scan. The scans where all channels are sampled are designated 'A-scans'. The scans which contain only the 85 GHz observations are designated 'B-scans'. The lower channels are sampled 64 times along an A-scan (vs. 128 for 85 GHz) with an integration period of 7.95 ms.

Channel resolution varies as a function of frequency, antenna size, and altitude. Taking into account the integration period, the effective resolutions of the lower three frequencies are approximately 69 km (along-track) x 50 km (cross-track) at 19 GHz, 60 km x 47 km at 22 GHz, and 37 km x 38 km at 37 GHz.

Additional details on the sensor design of the SSM/I and specifics for computing brightness temperatures are located in the *User's Manual-SSM/I Antenna Temperature Tapes* (Wentz 1988) and the *SSM/I User's Guide* (Hollinger et al. 1987). Appendix A is a schematic showing how the SSM/I views the polarizations.

The Multi-frequency Imaging Microwave Radiometer (MIMR) is a planned future passive microwave instrument that will measure brightness temperatures over

TABLE 1. Intercomparison of MIMR and SSM/I performance. (Values taken from the MIMR interim report, 15 November 1994, draft 0).

Performances	MIMR EOS-PM	MIMR METOP	SSM/I
Altitude (kms)	705	824	833
Incidence angle	50	55	53.1
Channels (GHz)	6.8 / 10.65 / 18.7 23.8 / 36.5 / 89.0	Same as EOS-PM	19.35 / 22.235 37.0 / 85.5
Sensitivity (K)			
@ 6.8 GHz	0.2	Same as	-
@ 19 GHz	0.5	EOS-PM	0.8
@ 89 GHz	0.7		1.1
Footprint size (kms)			
@ 6.8 GHz	60	85	-
@ 19 GHz	22	31	69
@ 89 GHz	4.9	6.8	15
Swath (kms)	1230	1600	1394
Antenna size (m)	1.6	1.6	0.61

12 channels (6 frequencies) ranging from 6.8 to 89 GHz. It is being considered for launch at the turn of the century on two separate platforms: the METOP and US EOS-PM satellites. See Table 1 for a comparison of SSM/I and MIMR performance features.

3. Previous work

Recent research has been conducted for developing algorithms to estimate sea surface and atmospheric parameters, specifically SST, WS, CLW, and PW. Several studies were conducted which discussed the development and the improvement of algorithms used to calculate WS (Wilheit 1979; Goodberlet et al. 1989) and both WS and direction simultaneously (Wentz 1992). Microwave emission from the ocean varies according to the sea surface state, i.e., its roughness and foam coverage. Calm seas are characterized by a relatively smooth surface which is highly reflective (low emissivity) and is associated with a highly polarized emission, assuming the satellite's view angle is far away from nadir (as with the SSM/I). The Fresnel relations from electromagnetic theory (Griffiths 1989) become applicable and state that the reflectivity for horizontally polarized radiation is greater than for the vertical; therefore, the horizontally polarized brightness temperature is always less than the vertical. If the sea surface becomes rough, the polarizations become mixed so that the difference (ΔT_B) decreases (Wentz 1992).

Sea foam and roughness are mechanisms that contribute to the variability of surface emissivity and reflectivity. Wilheit (1979) used a quantitative model to describe their effects on the microwave emissivity of the ocean surface. He compared his model with observations obtained from the electrically scanned microwave radiometer (ESMR) aboard Nimbus-6. He found excellent agreement between the observations and his model's predictions concerning the roughness effect but considerably more spread in the foam-effect results.

Goodberlet et al. (1989) used the "D-matrix" approach within their algorithm for retrieving WS measurements. This approach attempts to find a linear relationship

between observed brightness temperatures and geophysical parameters. As is the case for retrieving any of the environmental parameters, any rain in the FOV of the radiometer must be taken into account. They developed a rain flag criterion for their algorithm that is sensitive to rain rates below 1 mm hr^{-1} (rain flag "1"). As the rain intensity increases, rain flags 2 and 3 appear to reveal areas of heavy precipitation. It follows that as the rain rate increases, the accuracy of their retrievals decreases.

The determination of cloud liquid water over the oceans using microwave measurements has been largely neglected (Bauer and Schluessel 1993; Wilheit, personal communication). Alishouse et al. (1990) developed a purely statistical method to determine CLW and found no significant correlation between observed SSM/I brightness temperatures and the surface-based CLW calculations when retrievals were performed over land or snow. However, they found a high correlation for ocean-based retrievals. Greenwald et al. (1993) employed a simple physical model which used the 19 and 37-GHz channels of the SSM/I to retrieve CLW estimates over the oceans. They compared their physically based model to the model developed by Alishouse et al. They found that the Alishouse et al. model underestimated the liquid water path by roughly a factor of 2. They agreed that the statistical model detected a CLW signal but the underestimation was probably due to the inability of that model to completely separate the influence of water vapor from the effects of clouds.

Optically thick paths in the atmosphere (containing dense clouds or rain), i.e., the emission and scattering regimes, within the field of view (FOV) of the radiometer can significantly reduce the polarization difference. Additionally, the emission of microwaves from cloud droplets and rain will translate as an increase in brightness temperatures in both polarizations.

Passive microwave measurements reveal information about rain and precipitation-sized ice in the FOV of the SSM/I sensors. Prabhakara et al. (1992) used the 37-GHz channels to compute rain-rate statistics over the oceans. They found that at this frequency, where the FOV at the Earth's surface is approximately 30 km, rain is a

fairly strong emitter of microwave radiation while scattering by ice has a much smaller effect. At frequencies below 37 GHz, where the FOV is larger and the volume extinction coefficient is weaker, any additional information about rain appears somewhat redundant. However, at 85 GHz, where the FOV is approximately 15 km and the extinction is strong, direct information pertaining to rain is masked by the clouds. At this frequency, scattering by ice becomes very noticeable.

Nelkin (1992) examined the distribution of observed brightness temperatures as measured by the SSM/I at 85 GHz during August 1987. His study focused on several land and oceanic regions each encompassing an area of 5° latitude by 5° longitude. For each area for the entire month, he examined the pairs of brightness temperatures (vertical and horizontal), calculated each pair's average temperature, $(T_{BH} + T_{BV})/2$, along with their polarization difference ($T_{BV} - T_{BH}$ or ΔT_B) and plotted these temperatures on two-dimensional histograms or scatterplots. The observations were plotted on a Cartesian grid with the number of occurrences of each observation indicated by a shading scale. The plots were displayed with the average temperatures on the vertical axis and the polarization differences on the horizontal axis. Figure 1 is an example of the resulting plots which shows two 'branches'. The vertically oriented branch is indicative of the scattering regime while the negatively sloped branch is representative of the absorption regime.

Next, Nelkin defined a somewhat arbitrary point to delineate the scattering and absorption regimes. He identified a point at the top of the "notch" between the two branches where no observations were recorded. All observations to the right of this point fell into the absorption branch; all observations to the left and below this point were classified as the scattering branch. This still left quite a few observations unclassified due to the ambiguities associated with the source of the atmosphere's increased opacity (i.e. scattering from raindrops and ice particles or absorption from clouds and water vapor).

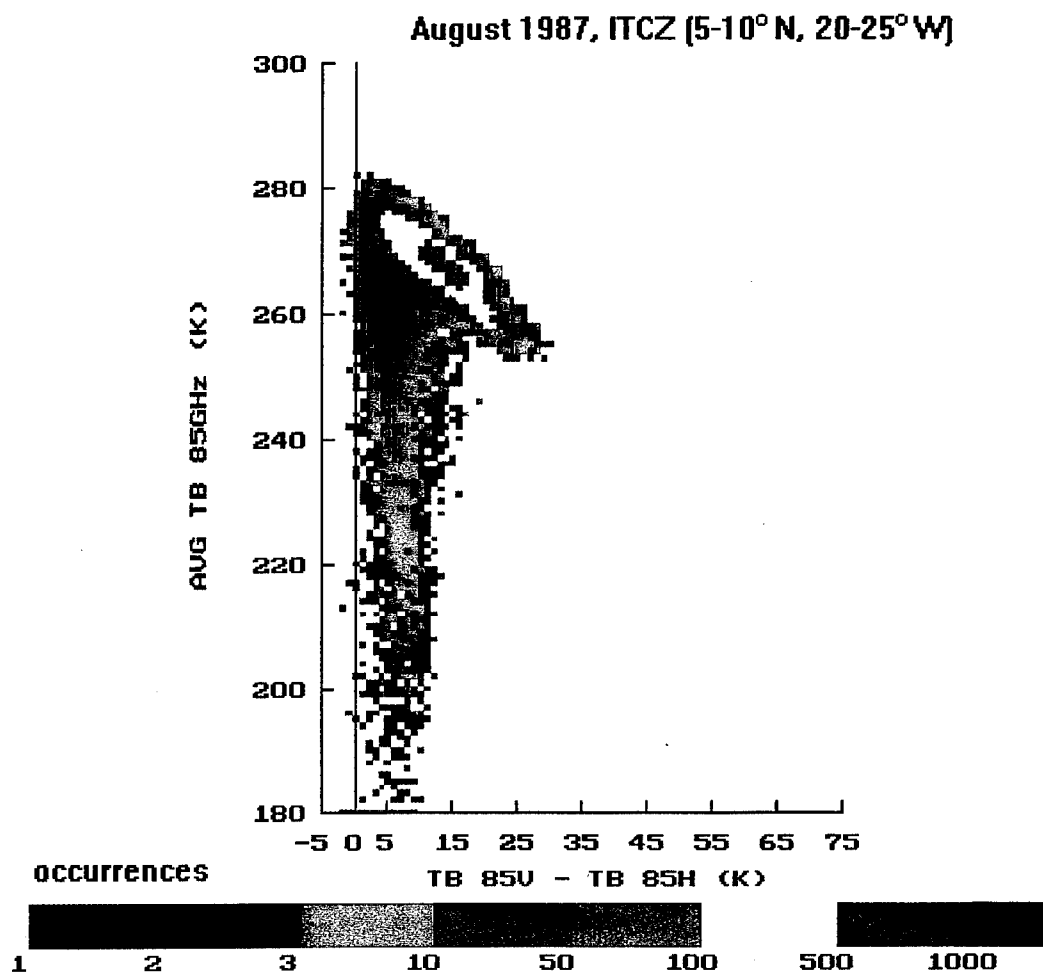


FIG. 1. SSM/I-observed average brightness temperature vs. polarization at 85 GHz for August 1987 - ITCZ box.

Nelkin used those pairs of brightness temperatures in the absorption branch to restrict retrievals of various geophysical parameters using the technique of Wilheit and Chang (1980). New "restrictive" algorithms resulted which improved the accuracy of the retrieved parameters. However, only those pairs of T_B 85 GHz observations and their associated lower channel observations which were clearly identified as belonging to the absorption branch could be input into these new algorithms. Due to the increased opacity (from rain and dense clouds) associated with many weather regimes, the applicability for using these new algorithms was severely limited (as little as 8% of the time for parts of the ITCZ).

4. Research objectives

The first objective of this investigation is to determine how often Nelkin's improved algorithms can be applied on a global scale after classifying all observations as belonging to either the absorption or scattering regime. These algorithms will constitute a simulation study for the performance of the MIMR which is tentatively scheduled for launch in the year 2000. The result of my first objective is a series of global maps depicting various sensitivity distributions relating the polarization differences between the 85 GHz channels ($T_{B85V} - T_{B85H}$) with the opacity of the atmosphere for a given region.

A second objective is to understand and explain the sensitivity distributions given the information contained in the CLW distributions over selected oceanic regions. Few studies have been conducted explaining the distribution of CLW in areas containing nonprecipitating clouds.

CHAPTER II

DATA

The data used in this study consist of earth located brightness temperatures as measured by the SSM/I and European Center for Medium-range Weather Forecasts (ECMWF) sea surface temperatures generated from the National Center for Atmospheric Research (NCAR) data.

The SSM/I data cover seven months (August - November 1987 and January - March 1993). The data sets are written in a binary format on CD-ROMs and are arranged in either hourly or daily files. The files contain brightness temperatures for all seven channels, time, and the associated location of an observation (latitude and longitude). In order to keep the amount of data to a manageable level, observation locations are reported only with those associated with the low frequency channels (i.e. A-scans only, 64 per scan). T_B 85 observations which are not collocated with low frequency channels are, for our purposes, assigned locations to an adjacent low frequency channel location (see Chapter V for further explanation and a schematic representation).

The geographic area, for this study, is restricted to brightness temperature measurements over the oceans between 60° N and S latitudes. A land mask, with a grid resolution of 0.5°, is applied to enforce this restriction.

Brightness temperatures are extracted off the CD-ROMs and placed into monthly files. These files are further subdivided into 5° x 5° latitude/longitude boxes. This process yields 1728 boxes of data for each month (land and ocean combined).

Boxes that contain all land are discarded while water boxes are kept for further analysis. Boxes that comprise a mixture of land and water (i.e. coastal and island areas) are classified *oceanic* if the water area is $\geq 10\%$ of the total area. Based on the above criteria, the resulting number of oceanic boxes is 1270.

Even though a box may contain as little as 10% water, only those observations that fall outside the land mask are used. This ensures land contamination is minimized. However, oceanic observations located within approximately 50 km of land are subject to land contamination since the criteria for determining water vs. land pixels used in constructing the land mask is imperfect.

The ECMWF data covers the time period from mid-January through March 1993. Similar to the SSM/I data sets, ECMWF surface temperatures are also written in a binary format and stored on CD-ROMs. Individual files contain one day of data. Observation points have a separation of 2.5° latitude and longitude and are reported twice daily (00Z and 12Z).

CHAPTER III

ABSORPTION VS. SCATTERING

OVER THE OCEANS

1. The absorption branch

Wilheit et al. (1994) stated that brightness temperatures that are low compared to the surface temperature and the associated layers of the atmosphere through which the radiation passes are produced in two ways. The first is scattering at short wavelengths (frequencies > 60 GHz) by ice particles with densities and sizes comparable to rain. This applies particularly well to the SSM/T's 85 GHz channels. The second is by reflection from a surface that has a high reflectivity. Such is the case with an ocean background as viewed by the SSM/I (Earth incidence angle of 53.1°). Since the view angle is far from nadir, the Fresnel relations from electromagnetic theory (Griffiths 1989) require that the reflectivity for horizontally polarized radiation always exceed the reflectivity for vertically polarized radiation (Fig. 2). Conversely, the emissivity for horizontally polarized radiation will always be less than the vertical. Therefore, the vertically polarized brightness temperature will always be greater than the horizontally polarized brightness temperature.

The atmosphere is fairly transparent to microwave radiation when no clouds and little or no water vapor is present (mild absorption case). In this instance, the brightness temperatures are low due to the highly reflective property of the ocean surface. Referring to the Fresnel relations, the polarization differences (ΔT_B) will be large.

As the opacity of the atmosphere increases, through the addition of water vapor and clouds, a comparative increase in the average brightness temperatures takes place. The absorption and concomitant emission of microwave radiation, from the now moderate to strongly absorbing layers of the atmosphere, result in increased brightness

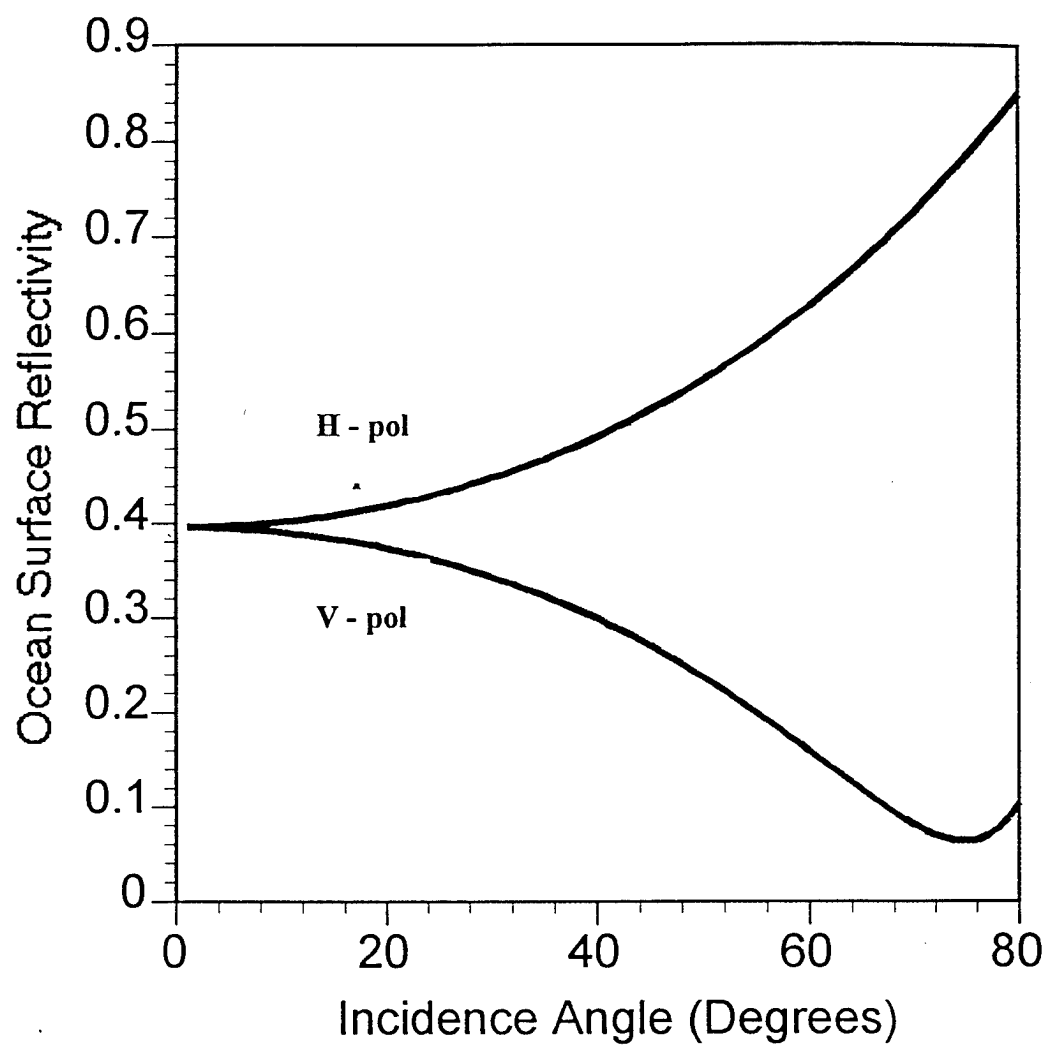


FIG. 2. Ocean surface reflectivity as a function of incidence angle and polarization for 85 GHz and surface temperature of 288 K. (Ocean surface computed for a complex index of refraction of $3.23 + 1.88i$).

temperatures. Also, the ΔT_B 's decrease as the polarization dependence decreases due to the increasing opacity of the intervening atmosphere.

Increasing atmospheric opacity moves the T_B 's along a nearly straight line in both polarizations (from lower to higher average T_B 's and concurrently, larger to smaller ΔT_B 's). The observations fall within a T_{BV} , T_{BH} space (or any linear transformation thereof) which can be depicted as the negatively-sloped absorption branch using the average-difference plots (Fig. 1). The characteristic slope of the absorption branch is always negative. A further physical argument is presented in section 4.

2. The scattering branch

The scattering regime can be characterized by small differences in the ΔT_B 's, and simultaneously, lower average brightness temperatures. The scattering regime appears as a nearly vertically sloped branch when displayed on the average-difference histograms (Fig. 1).

Low brightness temperatures which are generated by scattering will depend only slightly, if at all, on the polarization. This is the reason for very small ΔT_B 's in the scattering branch. It is the observations within this branch that must be eliminated in order to obtain reliable algorithm outputs. Any rain in the retrieval will invalidate the results.

Following the technique of Nelkin (1992), average-difference 2-D histograms are generated for each of the 1270 oceanic boxes for all seven months. The plots (Fig. 1 is an example) graphically depict the absorption and scattering branches. However, Nelkin's notch criterion for determining the borderline between both branches does not account for a large number of observations which can be classified as belonging to either regime. In order to maximize the percentage of time that 4-parameter (CLW, PW, SST, and WS) algorithms can be applied, it is necessary to statistically classify as many pair of 85 GHz (vertical and horizontal) observations as possible as belonging to either the absorption or scattering regime. This entails finding a method to separate the observations into their respective regimes.

The clue to solving this problem lies with the characteristic slopes associated with each branch. The slope of the absorption branch is always negative whereas the slope of the scattering branch is vertical.

The problem is where the two branches join. Here, the cloud drops, small raindrops, and water vapor are all contributing to the increasing brightness temperatures via their absorption and emission of the microwave radiation. The raindrops have yet to reach a size sufficient to produce noticeable scattering.

3. Separation of the branches

The following objective method is employed to delineate the observations within each branch. First, a linear regression is performed using the method of least squares to find the slope of the absorption branch for a given $5^\circ \times 5^\circ$ oceanic box. Specifically, only the observations which can be unambiguously identified as belonging to the absorption branch (i.e. as determined by Nelkin's notch criterion) are incorporated into the regression. The standard deviation (σ) of the average brightness temperatures is computed concurrently. Next, the resulting regression line (which runs through the center of the absorption branch) is extrapolated to cover the entire observed dynamic ΔT_B range (0-72K).

Before proceeding further, an assumption is made that the average brightness temperatures within the absorption branch are normally distributed. Boundary lines are then displaced $\pm 2\sigma$ from the regression line. Based on the above assumption, approximately 95% of all observations will lie between the boundary lines. All observations that fall between these lines are classified as belonging to the absorption regime. Observations outside the lines are classified as either belonging to the scattering regime or bad data. In either event, for the purposes of this study, only the observations within the absorption regime are relevant.

The histogram in Fig. 3 shows the result of applying the branch separation method to the data used in plotting Fig. 1. This box lies within the Intertropical Convergence Zone (ITCZ). Approximately 17% of the observations fall outside the

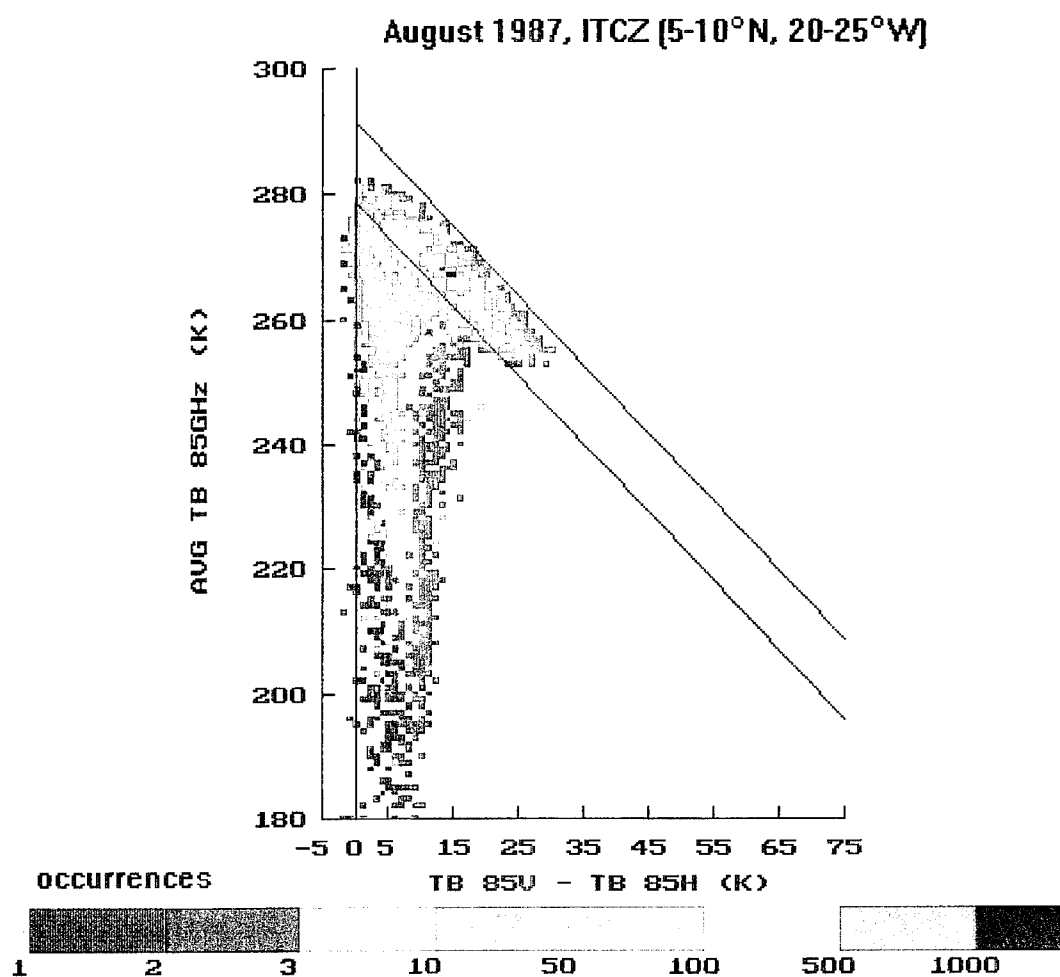


FIG. 3. Result of applying branch separation method to figure 1. (Data between diagonal lines constitute the absorption branch for this box).

absorption branch. Statistically, this is equivalent to stating that it rained approximately 17% of the time in this region during August 1987. Climatologically, this particular statistic appears to slightly overestimate (underestimate) the percentage of scattering (absorption) related brightness temperature observations. This discrepancy occurs in regions which commonly experience dense clouds and persistent light to heavy rainfall. The ITCZ, South Pacific Convergence Zone (SPCZ), and monsoon regions (i.e. Bay of Bengal) can be described in this manner.

However, it is preferable to underestimate (versus overestimate) the number of absorption related observations since the main drawback is a reduction in the percentage of time 4-parameter algorithms can be applied. An overestimation would allow scattering related observations into the algorithms. The errors associated with algorithm outputs would increase. However, a quantitative assessment of these errors has yet to be accomplished.

Further examples (Figs. 4 and 5) demonstrate that the separation method works well over most of the Earth's oceanic regions. Figures 4 and 5 are representative of the midlatitudes and subtropical high belt regions respectively. Two distinct differences between the midlatitudes and subtropics versus the tropics are worth noting. First, the plots associated with the midlatitudes and subtropics reveal a higher percentage of observations belonging to the absorption branch than do those associated with the tropics. The absorption branch in the midlatitude box (Fig. 4), accounts for 98.5% of the total observations, while the subtropical box (Fig. 5) can be described as a single branch plot (100% absorption).

Transient extratropical cyclones and their associated fronts create the vertical updrafts necessary to produce convective rain and ice particles which are associated with the small percentage of scattering observations in the midlatitudes. The single branch structure of the subtropical high region is indicative of a lack of vertical updrafts necessary to produce convective rain. Indeed, subtropical highs are often characterized as large areas of subsidence which inhibit cloud formation.

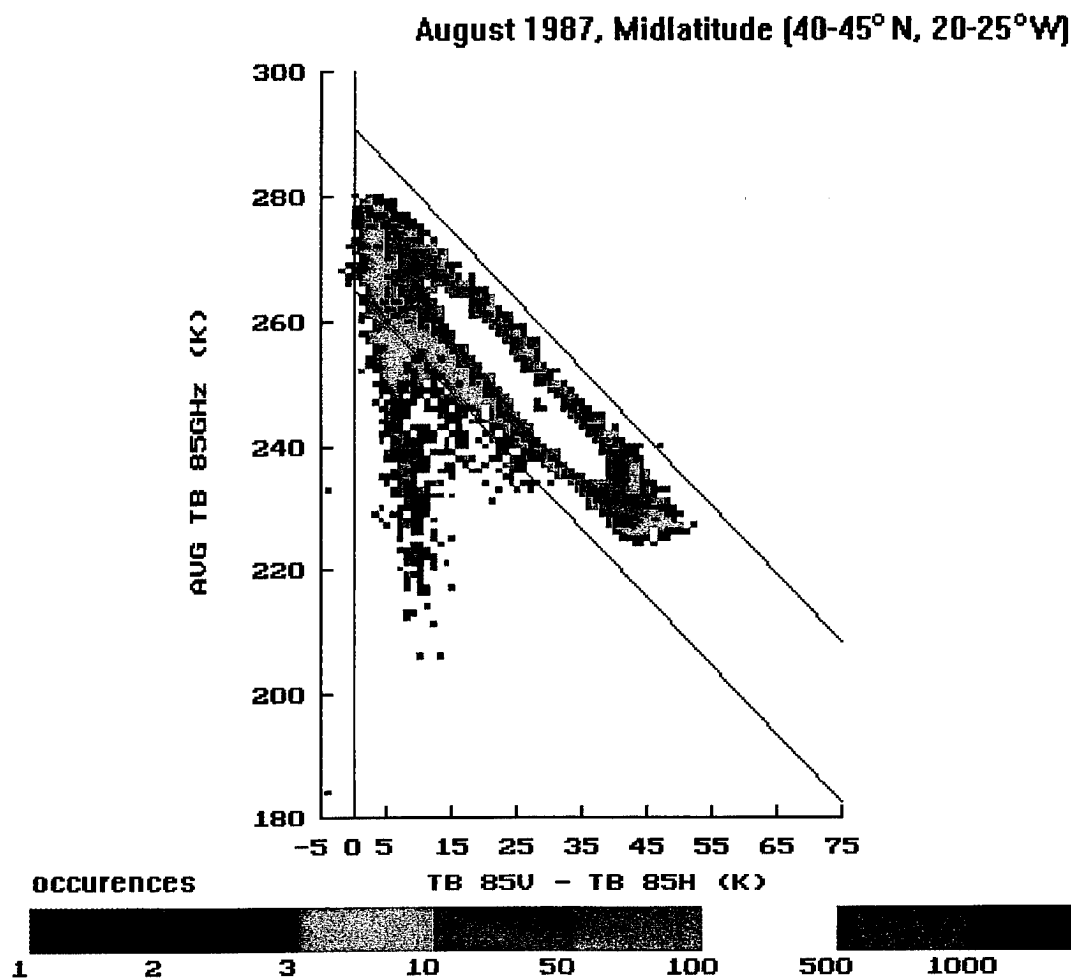


FIG. 4. SSM/I-observed average brightness temperature vs. polarization at 85 GHz for August 1987 - midlatitude box. (Data between diagonal lines constitutes the absorption branch for this box).

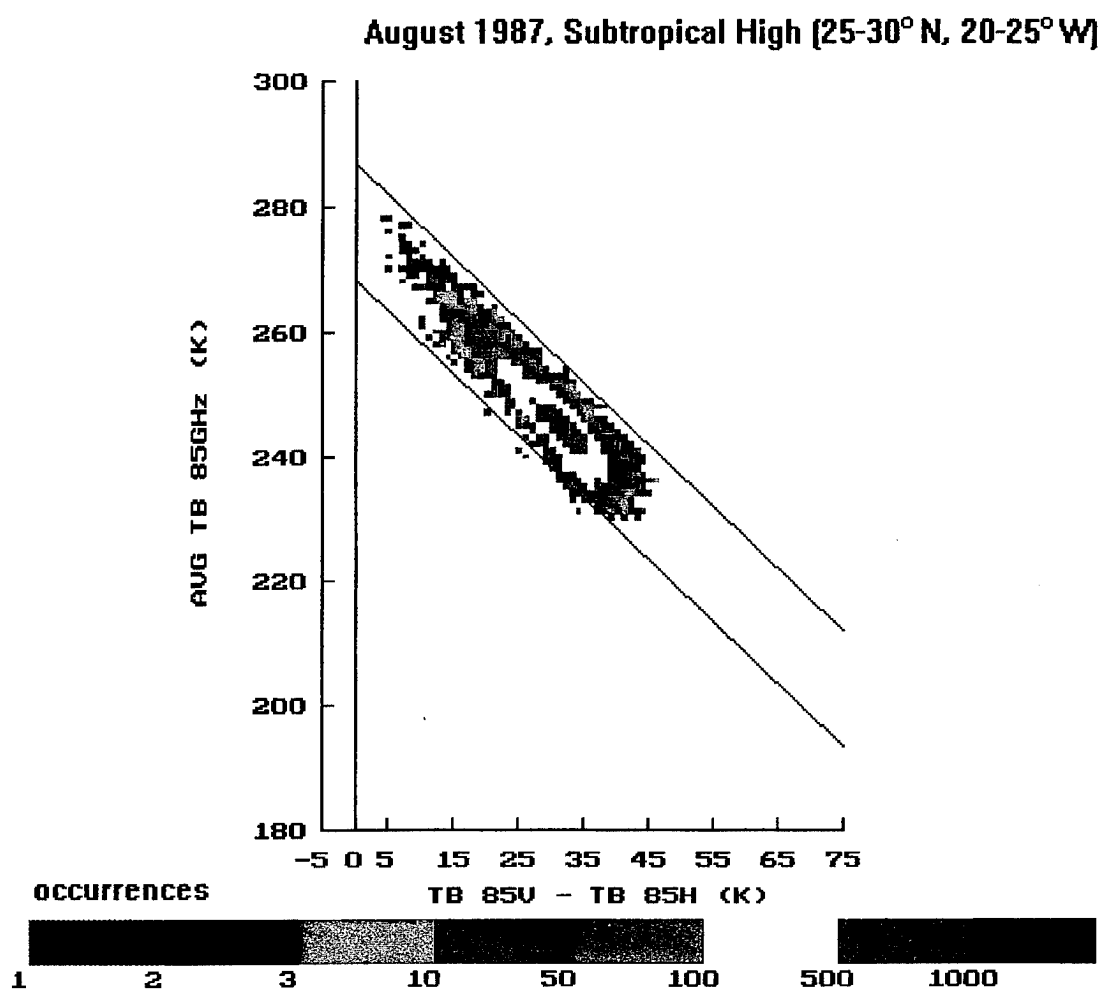


FIG. 5. SSM/I-observed average brightness temperature vs. polarization at 85 GHz for August 1987 - subtropical high box. (Data between diagonal lines constitutes the absorption branch for this box).

Second, CLW and PW vary greatly between regions. This can be illustrated by the various absorption branch lengths and widths. Following the physical description of the absorption branch in section 2, these large differences of CLW and PW can be explained by the differing climatic regimes associated with each region. The ITCZ shows the least variability (short and narrow branch), whereas the midlatitude box shows the greatest variability (long and wide branch). The atmosphere is very opaque along the ITCZ due to the extended coverage of deep convective clouds. The warming of the brightness temperatures are a function of the increasing opacity of the intervening atmospheric layers. Conversely, variable weather patterns associated with the midlatitude box (dynamic frontal boundaries to clear skies) produce a wide range of atmospheric opacities.

Even though the branch separation method works well over the majority of the Earth's oceans, it should be noted that sea ice (Fig. 6) in the SSM/T's FOV yields unusable results. It is apparent, from this plot, that the majority of observations form a vertical sloping branch. It should also be evident that it did not rain 99% of the time during February 1993 over Hudson Bay (as evidenced from the scattering branch).

Sea ice is electrically closer to land (small complex index of refraction) than water which gives the surface a low reflectivity. The lowering of brightness temperatures from apparent scattering results in little, if any, polarization dependence and thus small ΔT_B 's. Since the absorption branch cannot be detected, any areas containing sea ice must be avoided when invoking the 4-parameter algorithms.

This also suggests that small ΔT_B 's are a sensitive detector for the presence of sea ice and, therefore, can be used to filter out sea ice in addition to rain (reference Chapter I, section 1).

4. Physical justification for branch separation method

Up to this point, a statistical argument for separating the absorption and scattering regimes by employing T_B 85 observations was presented. The statistical method was

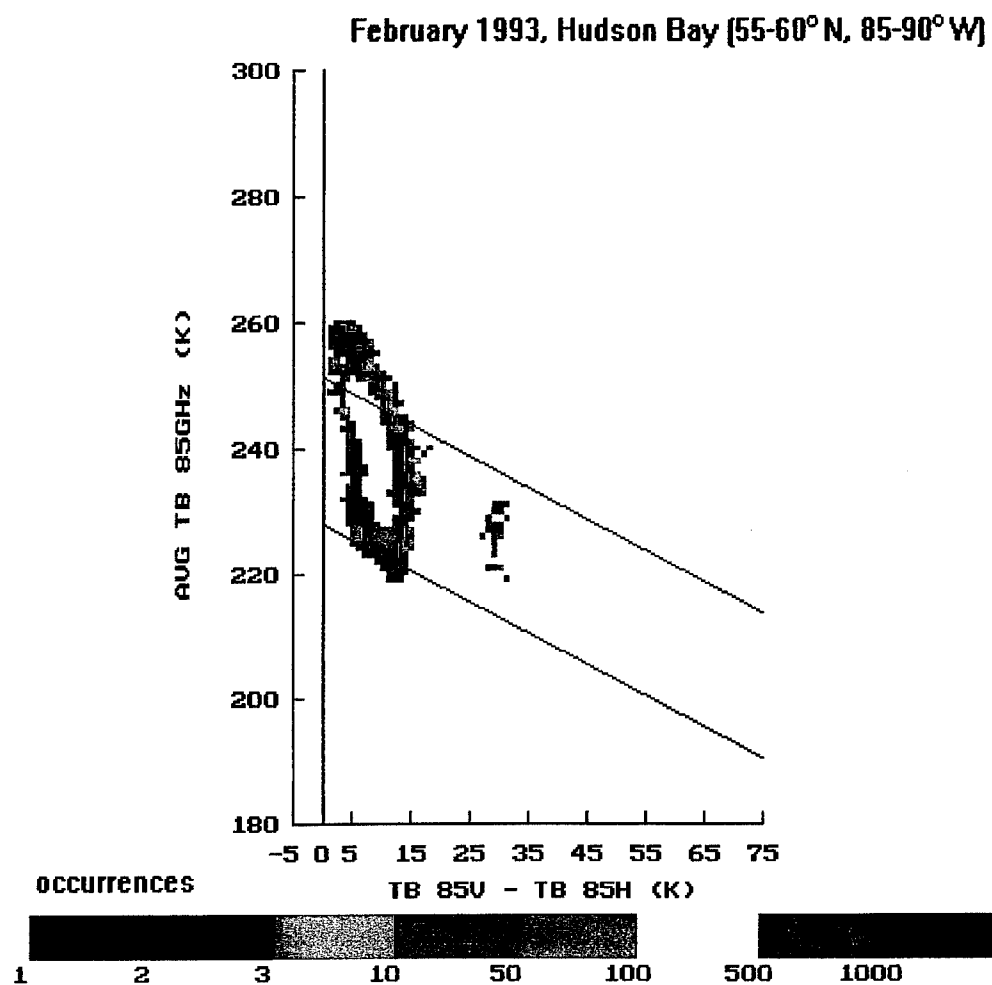


FIG. 6. SSM/I-observed average brightness temperature vs. polarization at 85 GHz for February 1993 - Hudson Bay region. (Branch separation method not effective due to presence of sea ice).

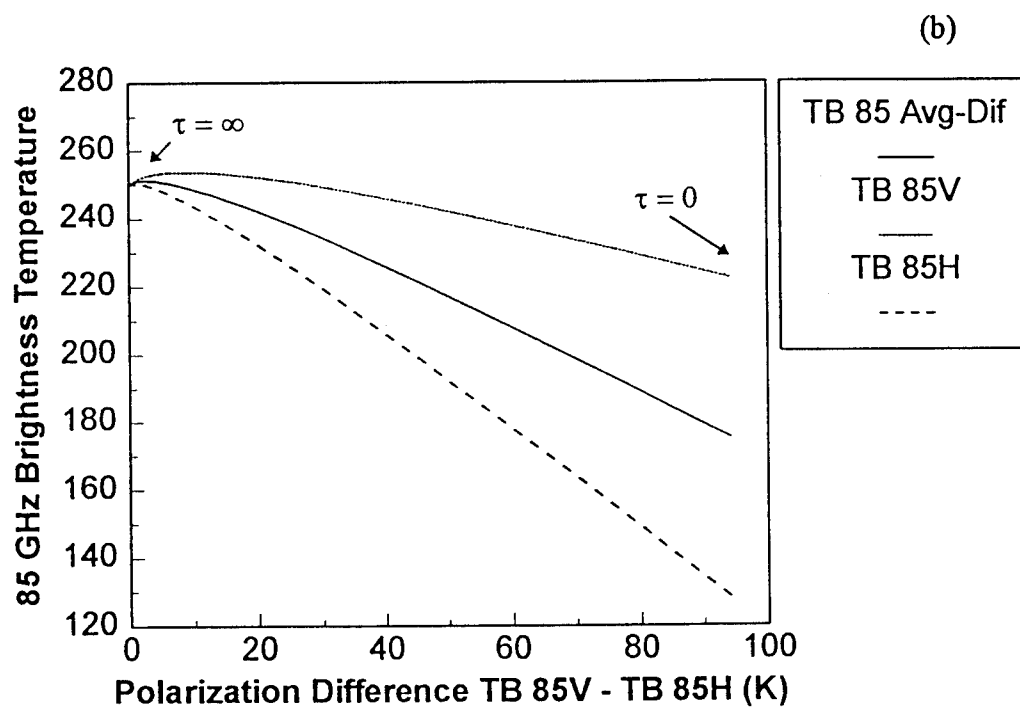
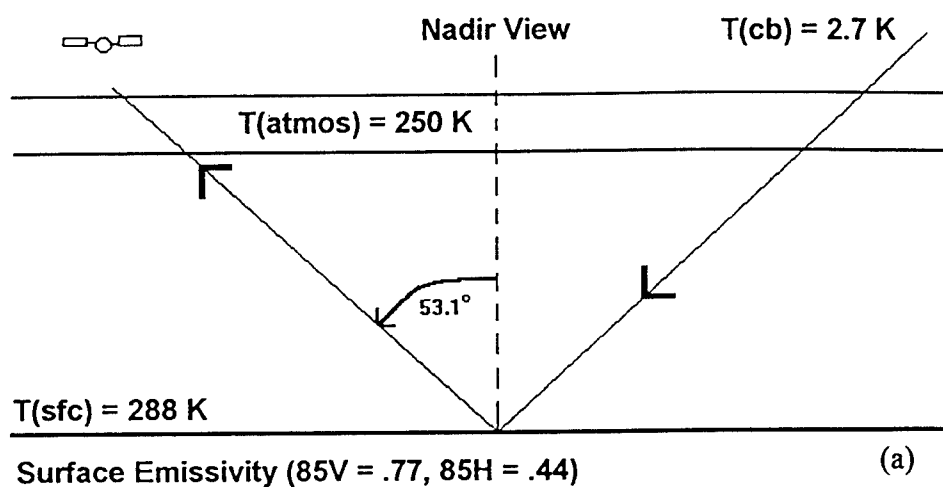


FIG. 7. Two-component (single layer atmosphere and surface) radiative transfer model (a) and effects on brightness temperatures as a result of varying optical depth (τ) (b). Surface emissivity values taken from figure 2. Optical depth varied from totally opaque ($\tau=\infty$) to clear sky ($\tau=0$).

used because of its relative simplicity and expeditious processing of vast quantities of data required to obtain global statistics. However, this method lacks physical meaning. Therefore, a simple radiative transfer model (RTM) based on the ERT is used to show that the statistical method is physically reasonable.

A simple two-component (single layer atmosphere and surface) RTM (Fig. 7a) can be constructed to illustrate radiative transfer. This model does not account for scattering and assumes atmospheric homogeneity. For a given surface temperature (T_s), view angle (θ), and wavelength (λ), by varying the optical depth (τ) from zero (no atmosphere) to infinity (completely opaque), brightness temperatures will vary nearly linearly (in both polarizations) from some computed value (no atmosphere case) to the cloud thermometric temperature (totally opaque case) (Fig. 7b).

For the ITCZ case, this temperature range is indicated by the lower dotted line in Fig. 8 which assumes that the coldest nonprecipitating (non scattering) cloud layer to be 272 K. If the cloud temperature is assumed to be close to the surface temperature, then the warmest expected temperature (in the opaque case) would be equivalent to that of the surface. This temperature range is indicated by the upper dotted line in Fig. 8.

The dotted lines in Fig. 8 trace out a triangle with the zero ΔT_B line its base. The area inside this triangle represents the range of possible values which could occur by allowing attenuation to vary from zero (no atmosphere) to infinity (totally opaque) at any temperature. The underlying physics can be applied globally, however, the expected range of temperatures (assuming absorption is taking place) between the surface temperature and cloud temperature varies latitudinally.

The temperature range is dynamic due to differing cloud types, heights, and thickness which are functions of the cloud's microphysics. Cloud microphysics is associated with various weather regimes which in turn can be categorized by latitude.

For example, in the tropics, clouds are generally convective (large vertical extent) and are situated globally in the warmest atmosphere. This condition persists to the point where there exists relatively little variability of cloud types and amounts.

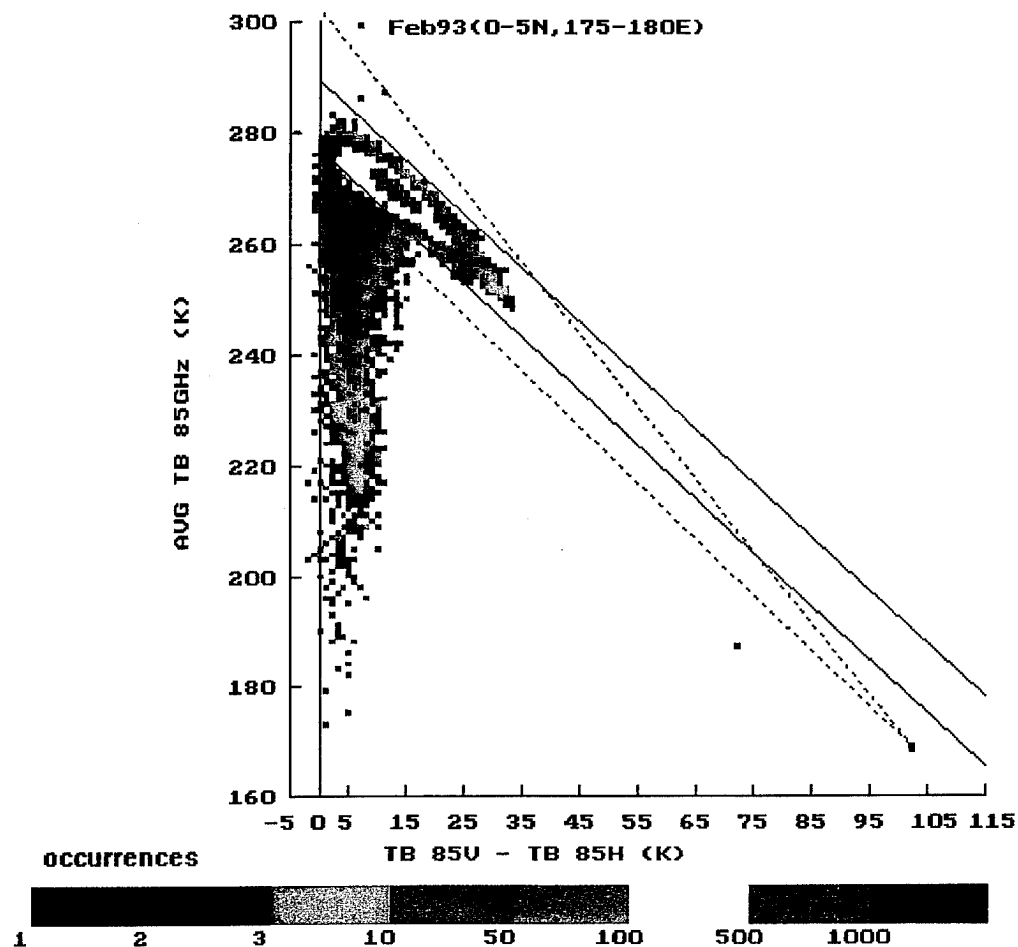


FIG. 8. Intercomparison of the physical model and the statistical method to identify the absorption branch of a February 1993, ITCZ box. (Data within dotted lines associated with physical model, data within solid diagonal line associated with statistical method).

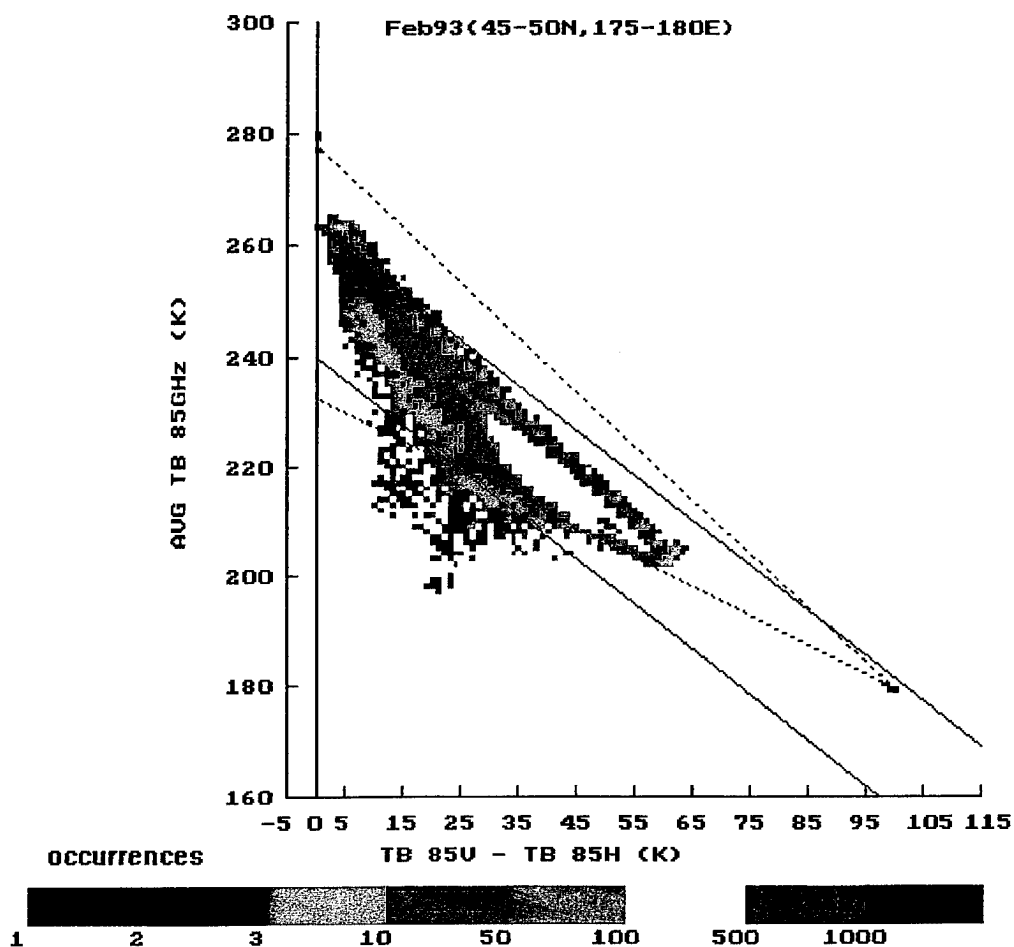


FIG. 9. Intercomparison of the physical model and the statistical method to identify the absorption branch of a February 1993, midlatitude box. (Data within dotted lines associated with physical model, data within solid diagonal line associated with statistical method).

Therefore a dynamic range of 30 K is sufficient to account for this variability and serve as the boundary for the absorption regime. The observations lying within the model's triangular boundaries are nearly identical to those which are defined by the statistical method (between the solid, parallel lines). Since the areas traced out by both methods are similar, this serves as an argument that the statistical method is physically reasonable.

Another example which illustrates how the temperature range is a function of cloud physics and variability is the midlatitudes. The midlatitudes experience the largest variabilities of CLW and PW due to transient extratropical cyclones. Large daily swings in atmospheric opacity (from clear skies through dense overcasts) are not uncommon. This necessitates a larger dynamic temperature range of 45 K to account for the majority of possible weather regimes (Fig. 9). As with the tropical region, the RTM output (area within the dotted triangular region) is in close agreement with the statistical method's output (area between solid, parallel lines).

As long as a sufficient dynamic temperature range is specified, the RTM output closely mirrors the statistical output. A reasonable representation for comparing the physical and statistical methods can be obtained by applying the dynamic temperature range criteria found in Table 2. This table differentiates the variability of atmospheric opacity by latitude.

TABLE 2. Dynamic temperature range necessary for application of physical model to statistics. Climate zones based on analysis of February 1993 SSM/I T_B 85 GHz observations over the North Pacific.

Climate Zones	Latitude Range (Degrees)	Dynamic Temperature Range (K)
High Latitudes	50-60	40
Midlatitudes	30-50	45
Subtropics	20-30	40
Tropics	0-20	30

CHAPTER IV

GLOBAL SENSITIVITY STUDY

1. Sensitivity percentile thresholds

Atmospheric opacity, in this study, is described in terms of 85 GHz ΔT_B 's. As previously mentioned, increasing atmospheric opacity yields decreasing ΔT_B 's. This allows algorithm sensitivities to be described in terms of the ΔT_B range.

Regions within the radiometer's FOV where the atmosphere is relatively transparent (i.e., $\Delta T_B > 25$ K) can be identified so that an algorithm can be made which is very sensitive to a specific parameter (CLW, PW, SST, or WS), thereby eliminating much of the retrieval's uncertainty. As opacity increases, the algorithm must be less sensitive to the desired parameter. This results in a larger retrieval uncertainty.

Four percentile thresholds (10, 50, 75, and 90) have been chosen to represent how often algorithms can be used based on their sensitivity. The method to determine the distribution of ΔT_B sensitivities involves the following procedure which is applied to each $5^\circ \times 5^\circ$ box separately.

First, the total number of T_B 85 observations are tabulated. Next, only the observations within the absorption branch are counted, in descending order of ΔT_B 's (from right to left along the horizontal axis in Figs. 1 and 3-6). When the number of observations within the absorption branch reaches a percentile threshold (percent of the total observations), the corresponding ΔT_B is noted and assigned as the 'sensitivity value' for that box at that percentile threshold.

For example, referring to the plot in Fig. 3, the total number of observations sums to 40,000. Counting observations within the absorption branch (from right to left), 4,000 observations (10 % of the total) have ΔT_B 's greater than or equal to 19 K. Continuing the process, 20,000 observations (50 % of the total) have ΔT_B 's greater than or equal to 14 K. This process continues until all four percentile thresholds are calculated. If the number of observations within the absorption branch is less than

what is required for a particular threshold (i.e. there is fewer than 36,000 observations to attain 90 % in Fig. 3), then a default ΔT_B value of -1 K is assigned.

2. Global sensitivity distributions

After sensitivity values are assigned to all 1270 oceanic boxes, global sensitivity maps for each of the four percentile thresholds are constructed (Figs. 10-13). Each figure shows a monthly (August 1987) composite, for a given percentile threshold, of the 1270 regions and their assigned sensitivity values.

Based on the assigned shading scale, sensitivity values (or equivalently, 85 GHz polarization differences) indicate relatively optically transparent (blue, >25 K) to relatively opaque (red, 0-5 K) regions. The percentiles indicate how often algorithms can be invoked. This depends on their individual sensitivity for retrieving a specific geophysical parameter. For example, in Fig. 10, a relatively sensitive algorithm (sensitivity value >20 K) can be employed at least 10% of the time over the majority of the Earth's oceans. The only exceptions appear to be along portions of the ITCZ and monsoon regions (Bay of Bengal and Arabian Sea) where dense clouds, water vapor, ice particles, and persistent rain render the atmosphere sufficiently opaque to lower sensitivity values of 15-20 K. The same logic applies for the remaining three percentile thresholds.

A by-product of the global maps is a strong correlation between the ΔT_B 's and large scale weather features. This is a good cross check for verifying the reliability of the entire global sensitivity mapping process since clouds, ice particles, water vapor, and rain are the main ingredients for triggering a change in atmospheric opacity at 85 GHz. At the 50th percentile (Fig. 11), moderately opaque (sensitivity values 15-25 K) regions appear in the extreme South Atlantic Ocean, while the majority of all southern hemispheric oceans remain relatively transparent (> 25 K).

At first glance, this might suggest that the increased opacity is a result of increased cloudiness, but inspection of the individual plots, of these relatively

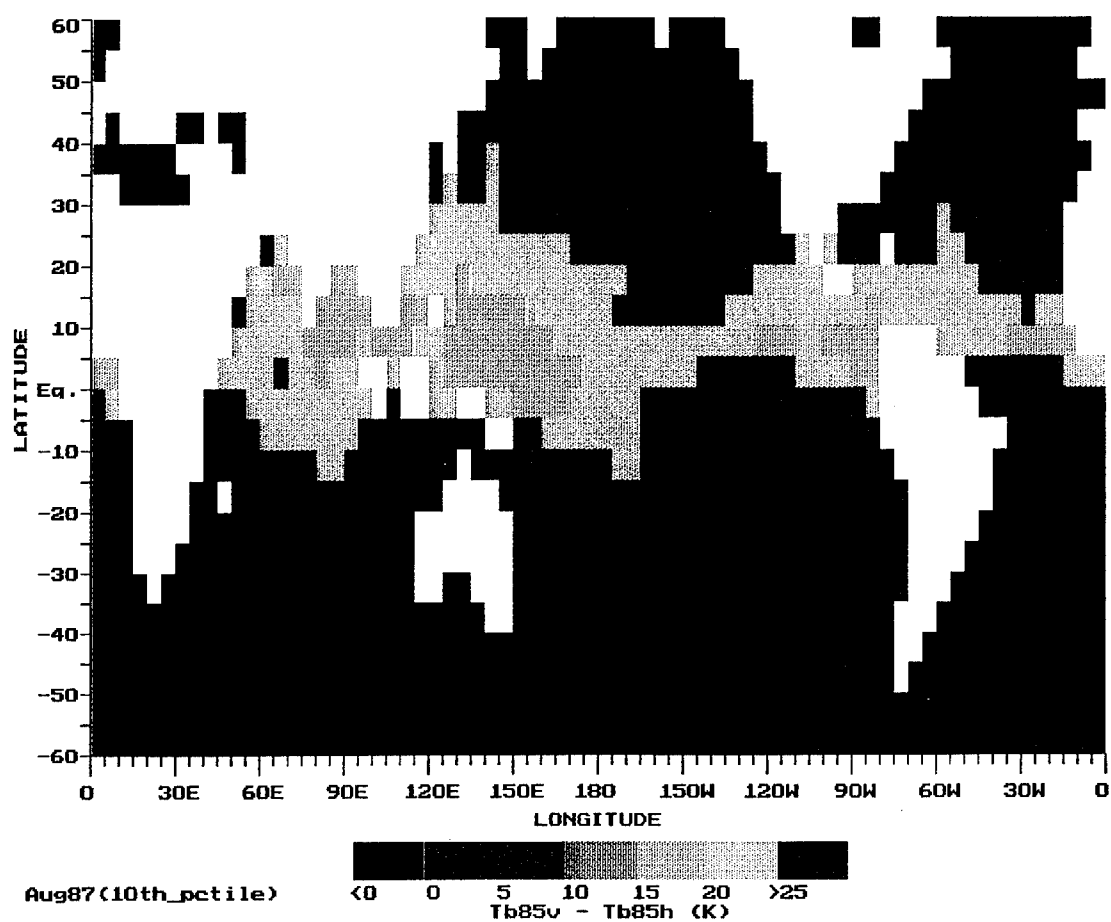


FIG. 10. Global sensitivity map depicting 85 GHz polarization difference values for August 1987 at the 10th percentile threshold. (Shading scale applies only to the 1270 oceanic regions; land regions default to white).

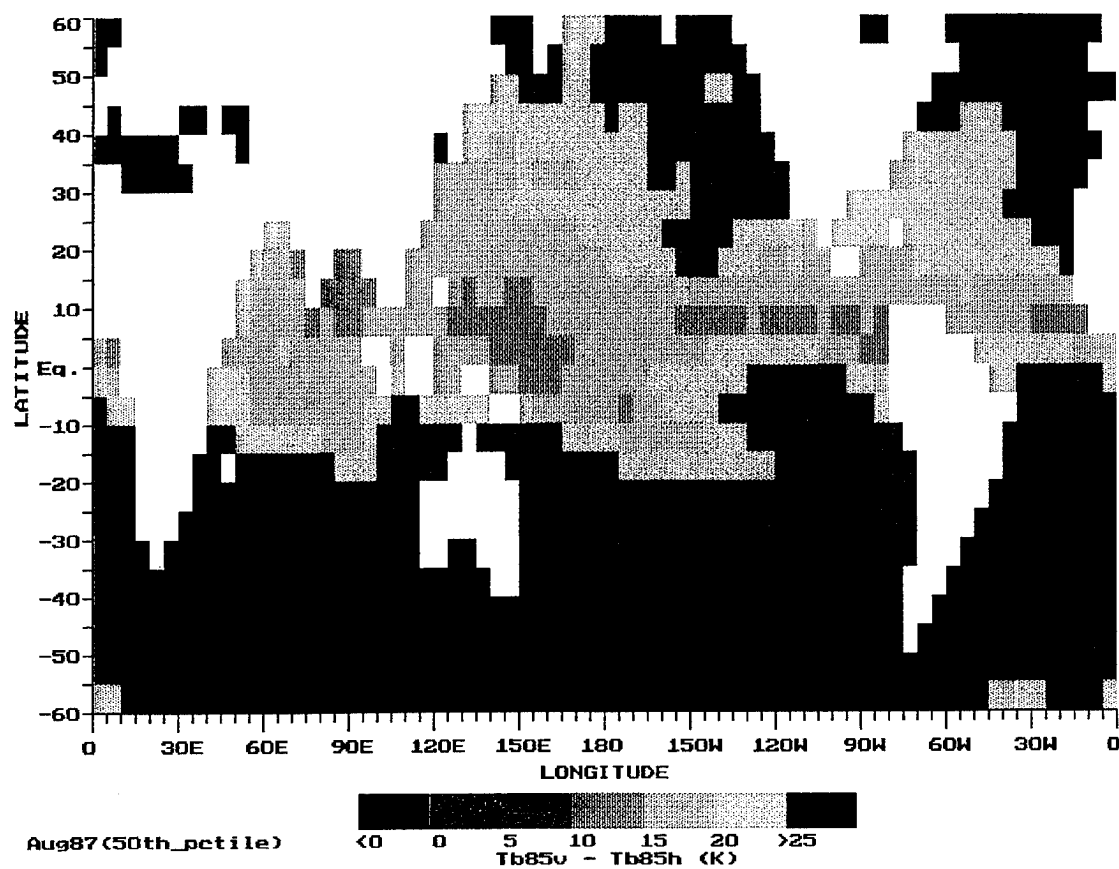


FIG. 11. Global sensitivity map depicting 85 GHz polarization difference values for August 1987 at the 50th percentile threshold. (Shading scale applies only to the 1270 oceanic regions; land regions default to white).

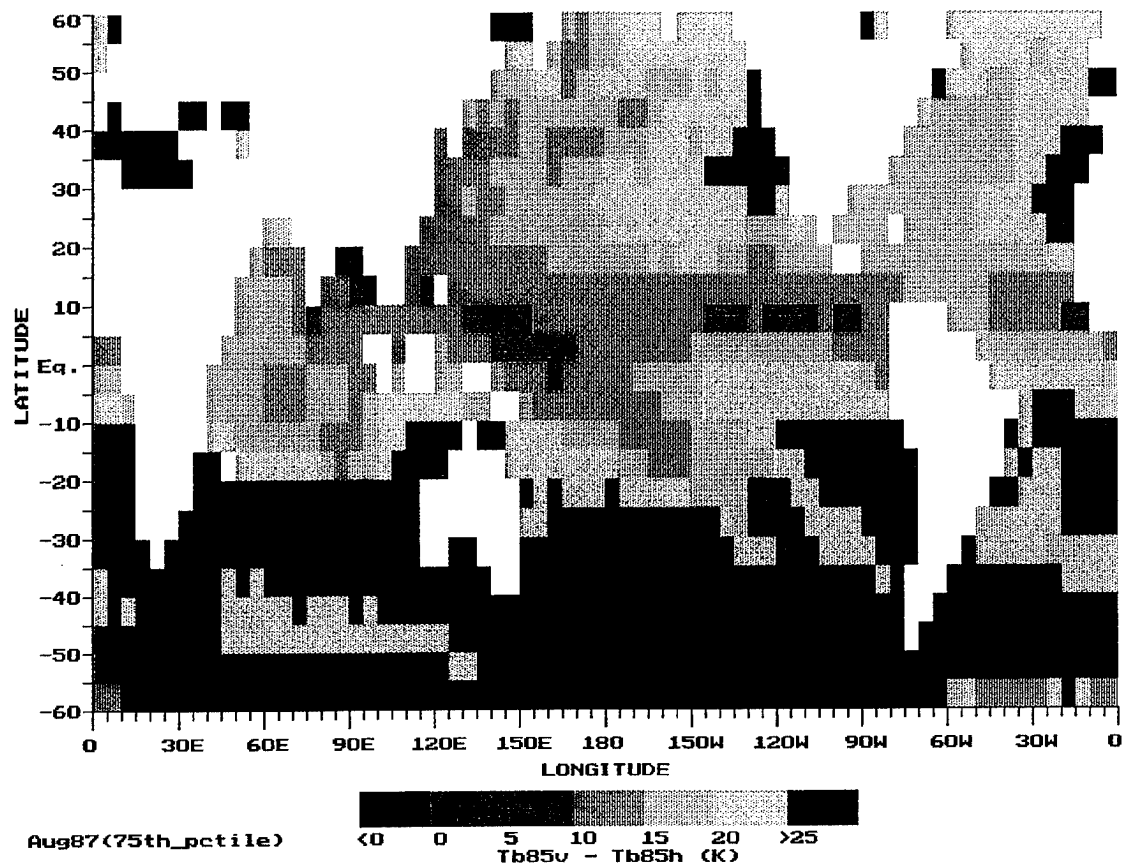


FIG. 12. Global sensitivity map depicting 85 GHz polarization difference values for August 1987 at the 75th percentile threshold. (Shading scale applies only to the 1270 oceanic regions; land regions default to white).

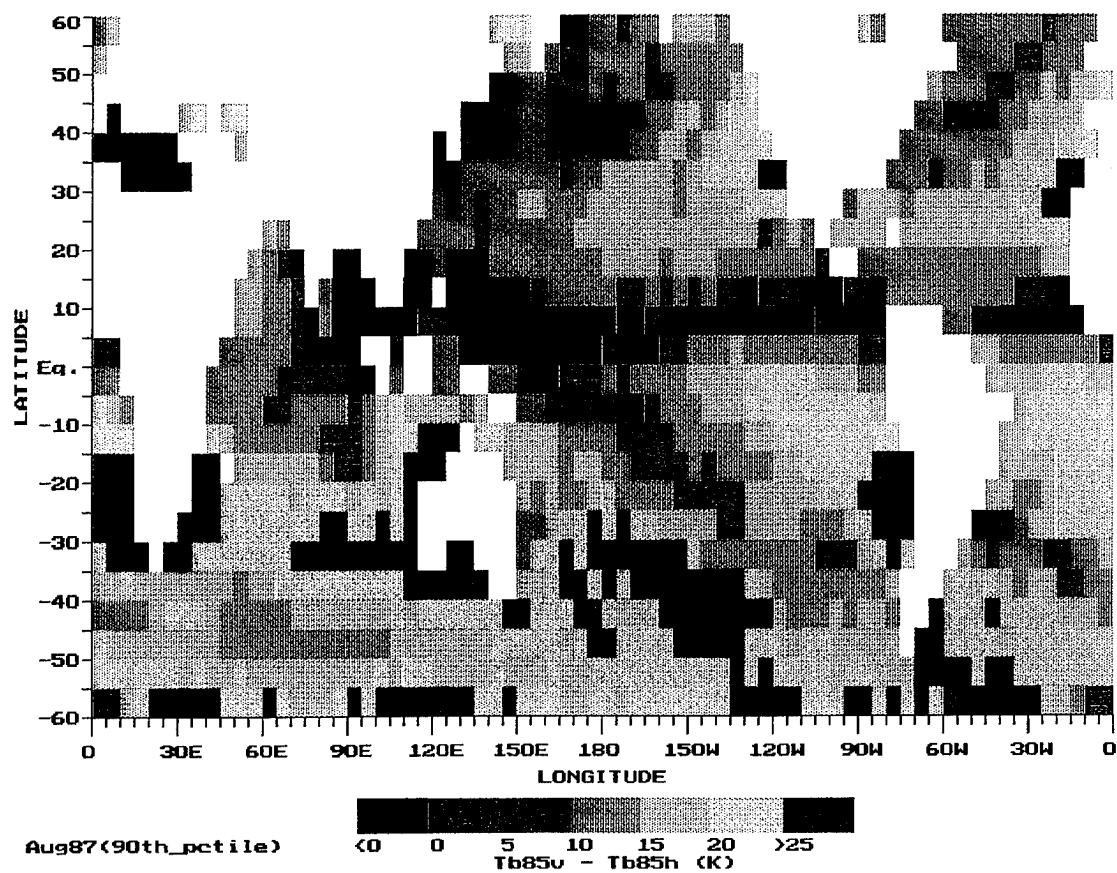


FIG. 13. Global sensitivity map depicting 85 GHz polarization difference values for August 1987 at the 90th percentile threshold. (Shading scale applies only to the 1270 oceanic regions; land regions default to white).

opaque regions, reveal similar profiles to those seen in Fig. 6. Therefore, based on the 85-90 GHz polarization differences, these regions are further examples of SSM/I observations contaminated by sea ice, and as such, cannot be incorporated into the global sensitivity distributions.

At the 75th percentile (Fig. 12), portions of the Bay of Bengal are extremely opaque (sensitivity values < 0.5 K). Specifically, a numerical analysis of the box which indicates a value of -1 K ($10 - 15^{\circ}\text{N}$, $95-100^{\circ}\text{E}$) reveals 73.8% absorption based observations. This statistic is equivalent to stating that it rained 26.2% of the time in that region during August 1987. To keep this in perspective, it would have to rain an average of six hours per day to achieve this absorption/scattering ratio. Since it is during the monsoon, this statistic seems plausible if not completely accurate.

Several additional meteorological features appear in fig. 12. First, the SPCZ is visible, via small polarization differences, from the eastern equatorial Pacific through the South Central Pacific. Next, the majority of the eastern North Pacific and Atlantic Oceans also reveal rapidly decreasing ΔT_B 's. In these regions, the increasing atmospheric opacity is most likely associated with transient midlatitude cyclones which feed off the warm waters carried by the Kuroshio and Gulf Stream currents.

Finally, there are many boxes which remain relatively transparent (>20 K) at the 75th percentile threshold to include the southern hemispheric oceans between 20 and 60° S. Transparent areas exist along the western coasts of North America and Africa (minus the ITCZ). It is in these areas where subsidence, associated with subtropical highs, is a major determining factor for the scarcity of clouds and precipitation.

The global sensitivity map of the 90th percentile (Fig. 13) continues, as expected, to show a decrease of polarization differences through all boxes. It is only in the most opaque regions (black (-1 K) and red ($0-5$ K)) where no algorithms can be expected to produce reliable results a majority of the time. Specifically, the areas of concern include the ITCZ, monsoon regions, portions of the SPCZ, and extreme South Atlantic Ocean (due to sea ice formation). However, this map shows that the least

sensitive algorithms (those which function down to a ΔT_B of 5 K) can be utilized up to 90% of the time over the majority of the oceans.

An alternative method for displaying the global sensitivity distributions involves focusing on the latitudinal variability of polarization differences. The graphs in Figs. 14 and 15 contain a plethora of information relating to both inter and intralatitude variability. Each graph displays statistics (maximum and minimum ΔT_B 's, mean ΔT_B , and \pm one standard deviation) for 24 separate sets of data.

Each data set contains *oceanic* boxes grouped along latitudinal bands in increments of 5° from 60° N to S. Since boxes have a width of 5° longitude, a maximum of 72 boxes is possible within a 5° latitudinal band around the Earth. The actual number of boxes used in computing the statistics for a given latitudinal band varies and can be considerably less especially in the Northern Hemisphere where the majority of Earth's land masses reside.

At the 10th and 50th percentile thresholds, there exist a symmetric pattern to the data between hemispheres. This pattern implies an increase in atmospheric opacity with decreasing latitude, as evidenced from the mean values. The summer (Northern) Hemisphere atmosphere is more opaque as seen from its lower mean ΔT_B values. The intralatitude variability ($\pm \sigma$) is similar for both hemispheres with one notable exception: larger variability between 30 and 40° N as compared to other latitudes. This increased variability could be partially due to the extreme differences in weather regimes associated with the subtropical highs (eastern portion of ocean basins) and warm ocean currents (western portion of ocean basins).

At the 75th percentile (Fig. 15), the symmetry begins to break down. A more complex pattern emerges which adds information to the rather simple hemispheric pattern suggested in the above paragraph. The summer hemisphere continues to show a higher atmospheric opacity; however, with the exception of the tropics, opacity no longer increases as latitude decreases. The presence of the subtropical high belt can again be seen by its large ΔT_B variability. The global ΔT_B variability increases for all latitudes from the 75th to 90th percentiles while a peak mean value between 30 and

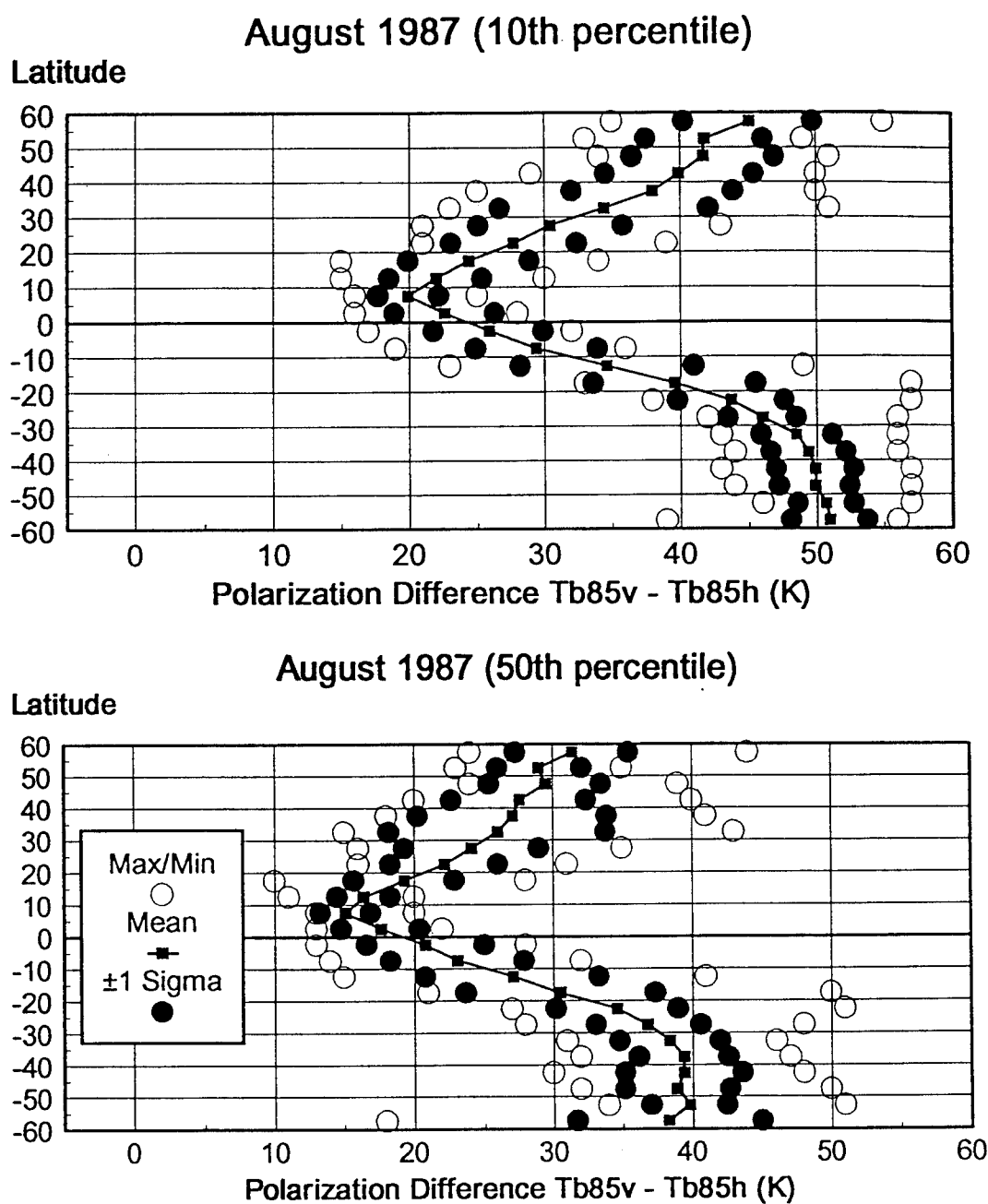


FIG. 14. Statistics displaying the latitudinal variability of the sensitivity distributions for August 1987 at the 10th (top) and 50th (bottom) percentile thresholds.

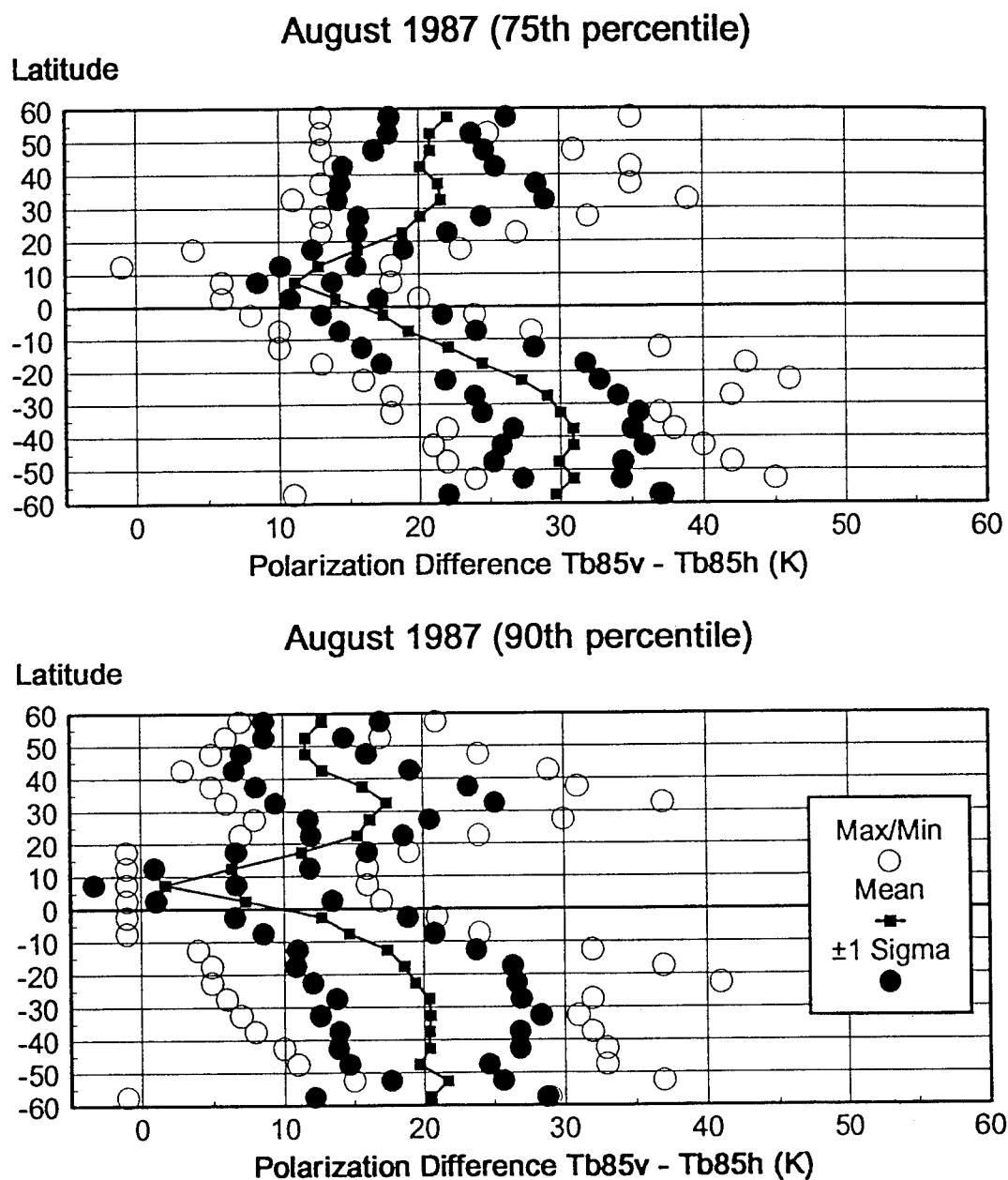


FIG. 15. Statistics displaying the latitudinal variability of the sensitivity distributions for August 1987 at the 75th (top) and 90th (bottom) percentile thresholds.

35° N (Fig. 15) indicates the most transparent atmospheric region in the Northern Hemisphere.

The graph displaying the 90th percentile statistics can be described as having a skewed distribution (the $-\sigma$ exceeds the minimum ΔT_B value) for the boxes in the data set ranging from 5 - 10° N. It is no coincidence that this happens to be the heart of the ITCZ.

Two factors contributing to the skewness can be explained. First, the minimum ΔT_B value (-1 K) is an artificial lower boundary (refer to section 1, this chapter). The majority of the observations within the ITCZ are extremely opaque and warrant the -1 K value. This leads to an extremely small mean ΔT_B (1.7 K). Second, a few boxes are associated with ΔT_B 's as large as 16 K. This computes to a fairly large variability and a standard deviation of ± 5 . Hence, the $-\sigma$ value (-3.3 K) exceeds the artificial minimum ΔT_B value (-1 K).

As previously mentioned, a good cross check for the global sensitivity maps are large scale weather features. In addition to finding latitudinal variations within the sensitivity distributions, comparing summer and winter scenarios yields further information regarding seasonal migration of large scale weather patterns (Figs 16-23). These graphs answer the questions: "Do seasonal variations in weather patterns alter the sensitivity distributions?" and if so, "How does this affect the applicability of our algorithms for retrieving various geophysical parameters" ?

For the seasonal comparison, data from August 1987 and February 1993 are analyzed to investigate changes that occur in the sensitivity distributions. At the 10th percentile (Fig. 16), several major differences are evident. First, the southward shift of the ITCZ (page 23, Crowley and North 1991) during northern winter (January - March) is readily apparent. Associated with the ITCZ shift, the monsoon region is experiencing its dry season (page 35, Wallace and Hobbs 1977). In sharp contrast to the summer scenario, the skies over the Arabian Sea and Bay of Bengal are mostly cloud free. This equates to large polarization differences for those regions which allows the use of algorithms that are sensitive to CLW, PW, SST, and WS. Also,

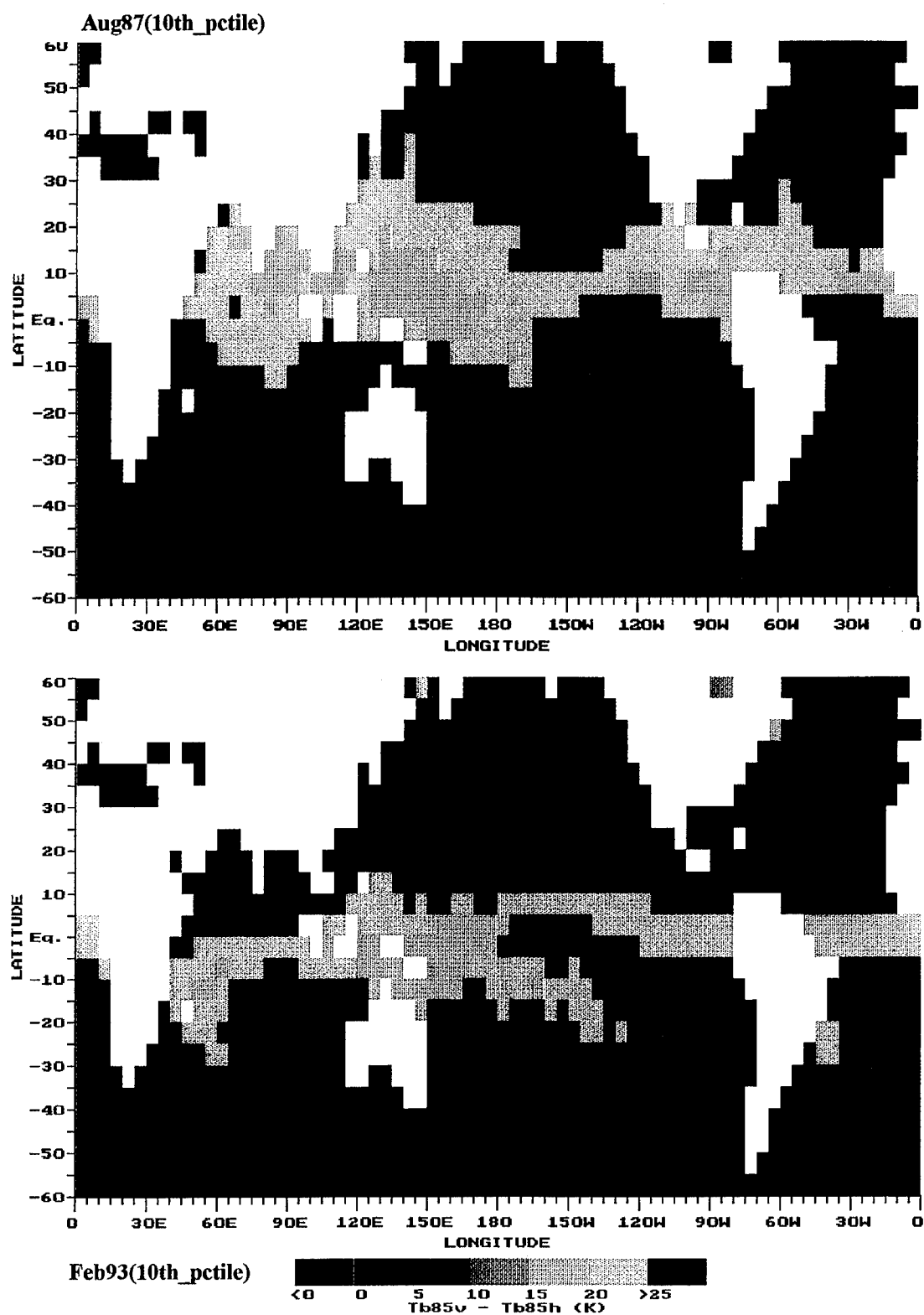


FIG. 16. Intercomparison of the global sensitivity distributions at the 10th percentile threshold for August 1987 (top) and February 1993 (bottom).

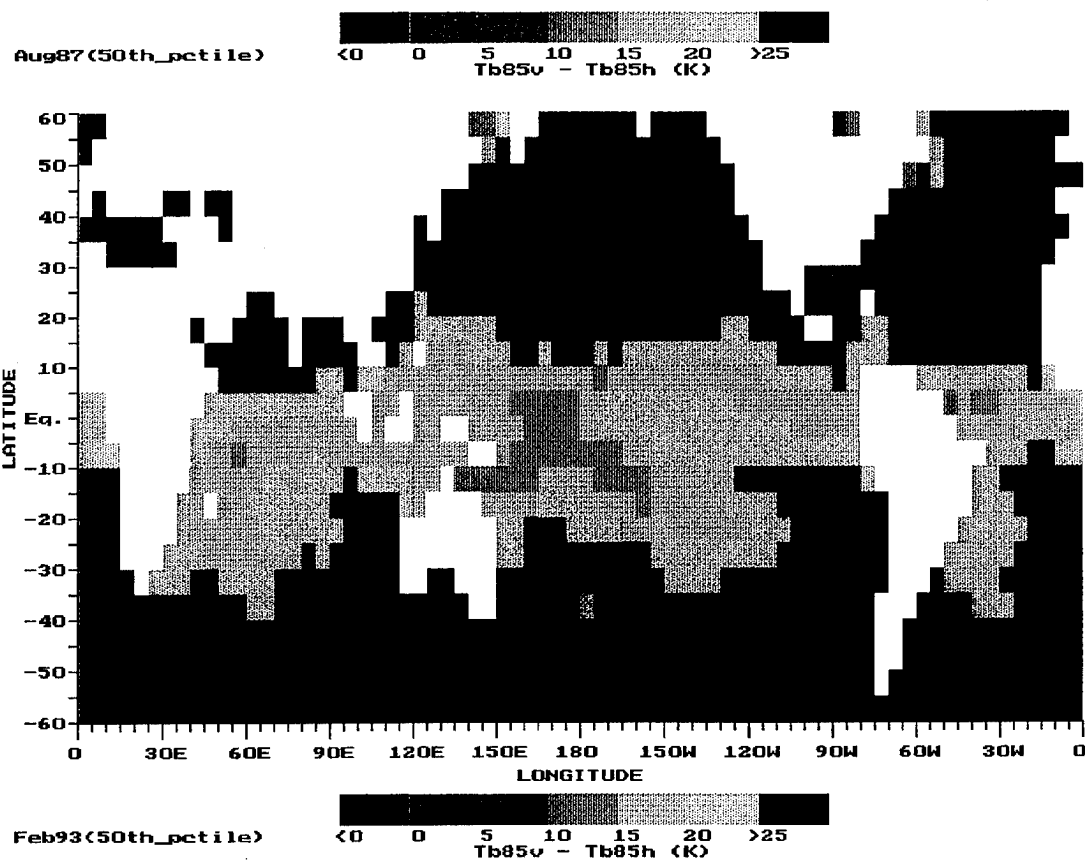


FIG. 17. Intercomparison of the global sensitivity distributions at the 50th percentile threshold for August 1987 (top) and February 1993 (bottom).

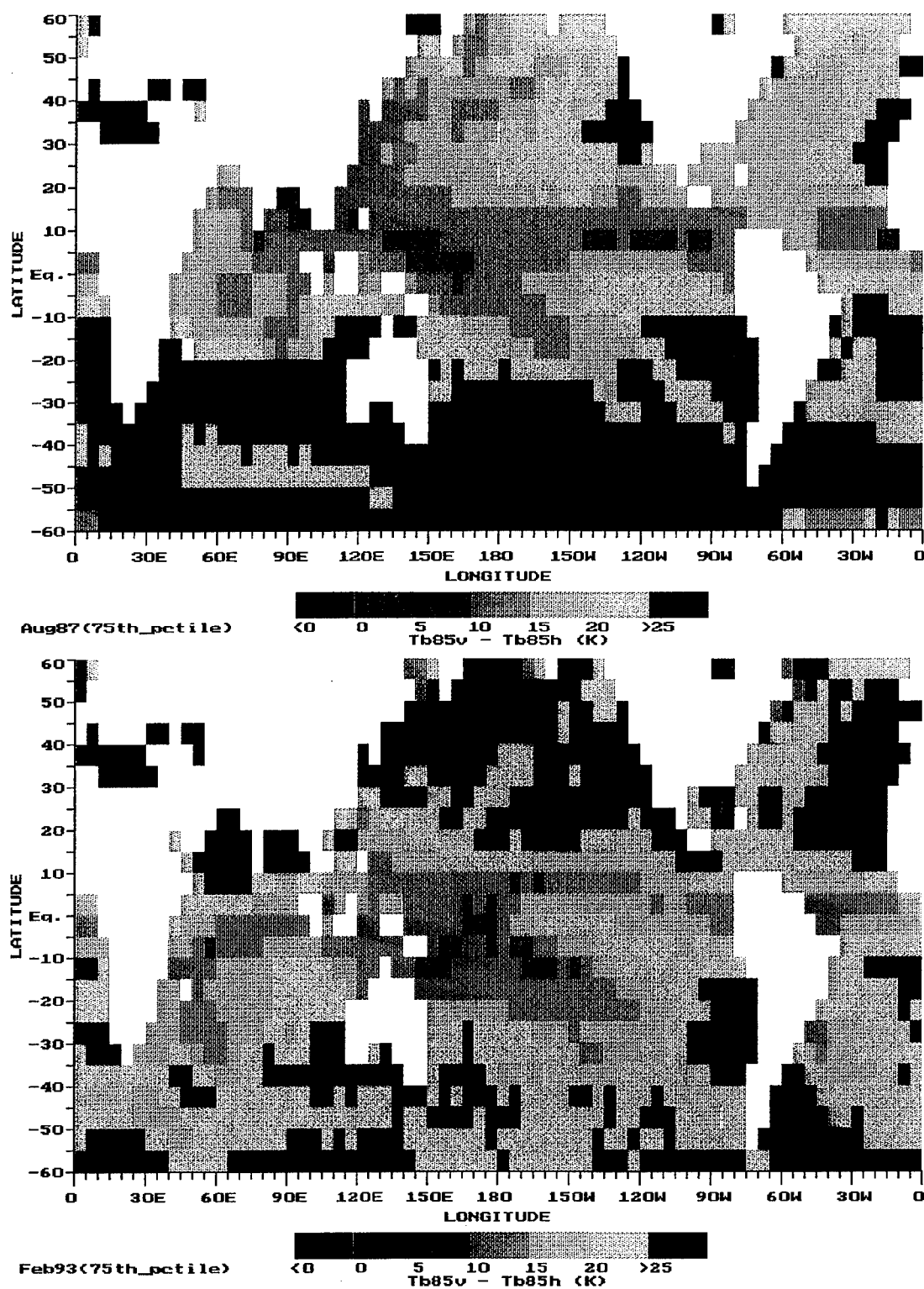


FIG. 18. Intercomparison of the global sensitivity distributions at the 75th percentile threshold for August 1987 (top) and February 1993 (bottom).

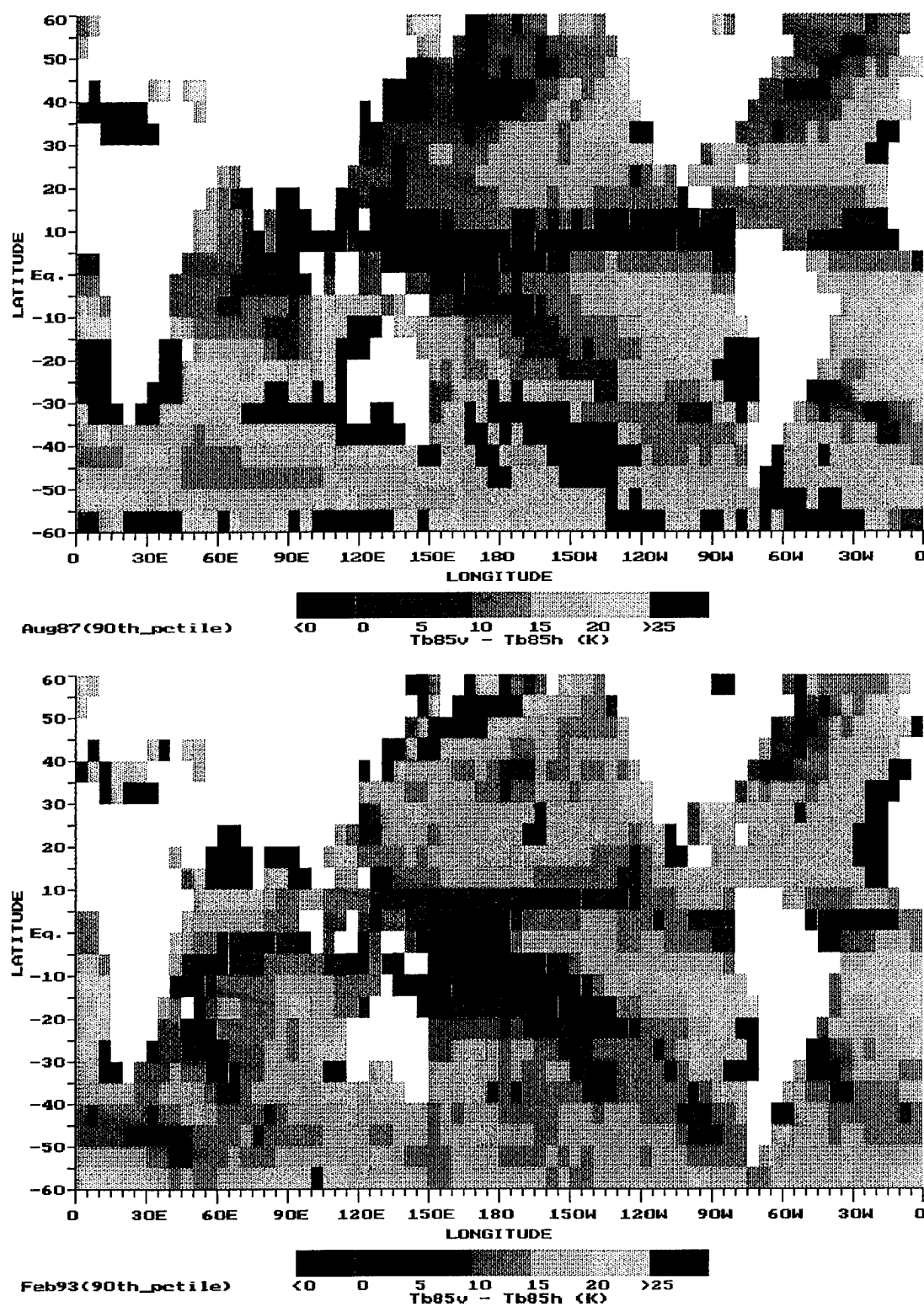


FIG. 19. Intercomparison of the global sensitivity distributions at the 90th percentile threshold for August 1987 (top) and February 1993 (bottom).

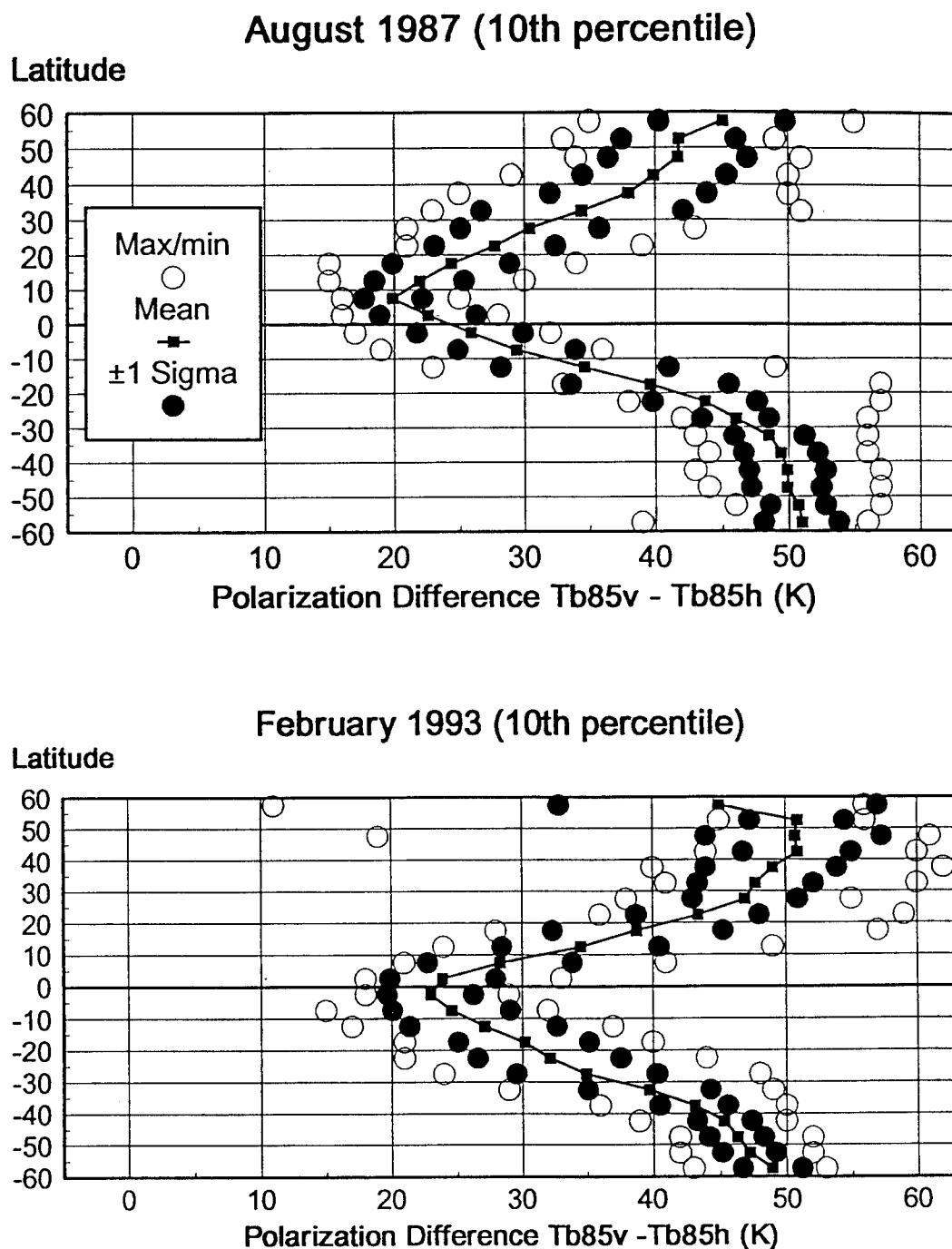


FIG. 20. Statistics comparing the latitudinal variability of the sensitivity distributions for August 1987 (top) and February 1993 (bottom) at the 10th percentile threshold.

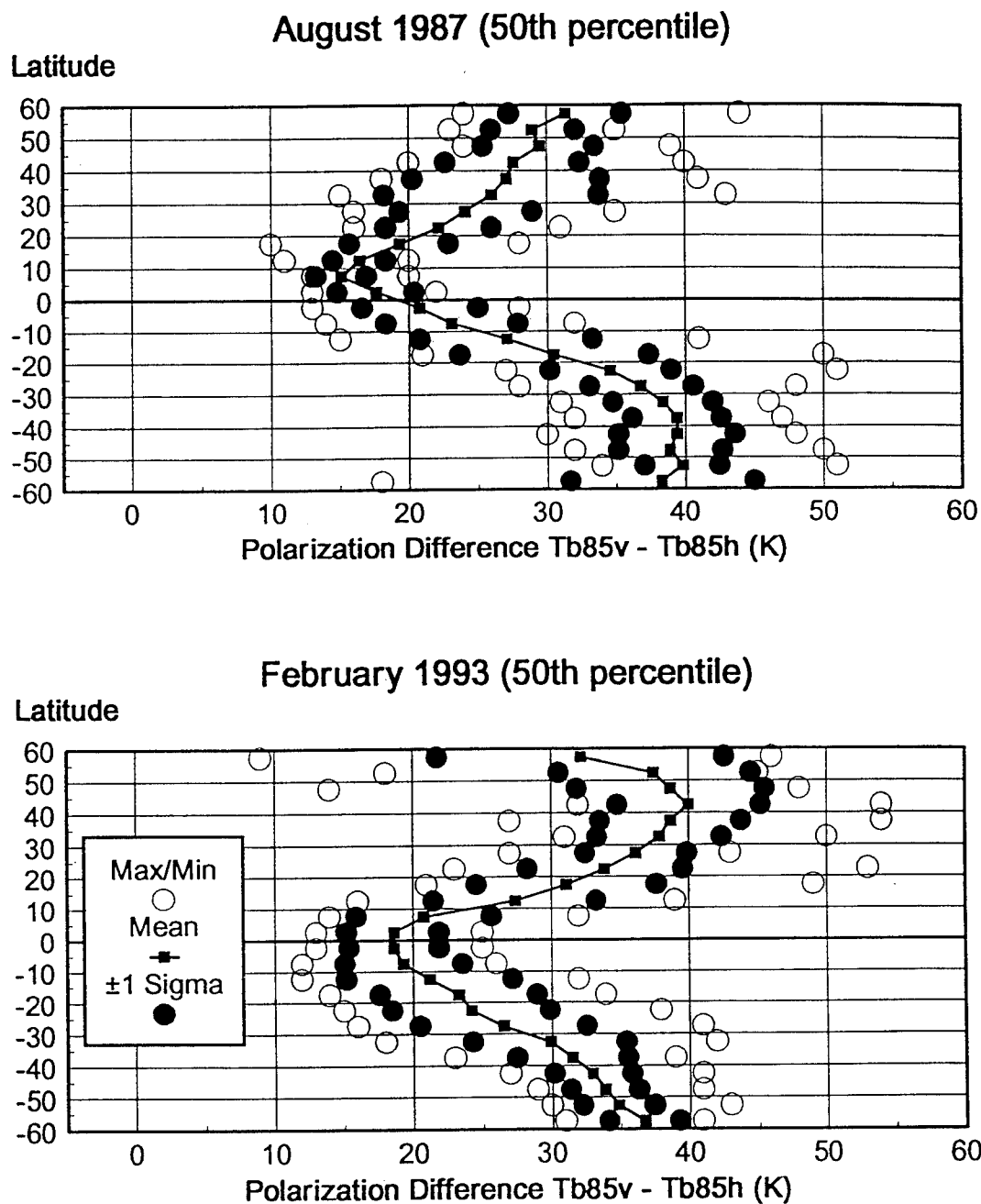


FIG. 21. Statistics comparing the latitudinal variability of the sensitivity distributions for August 1987 (top) and February 1993 (bottom) at the 50th percentile threshold.

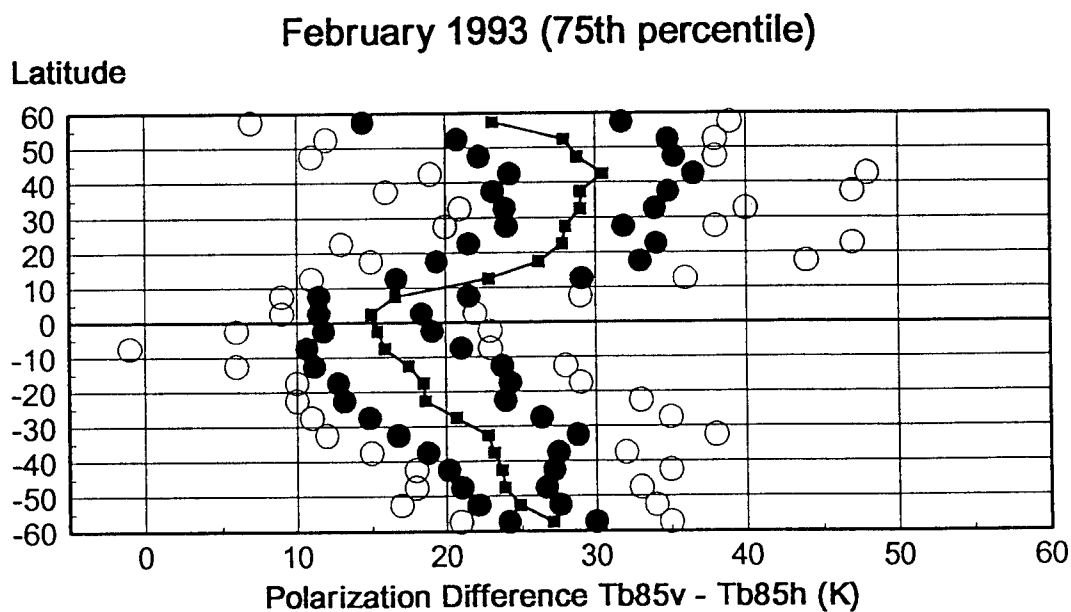
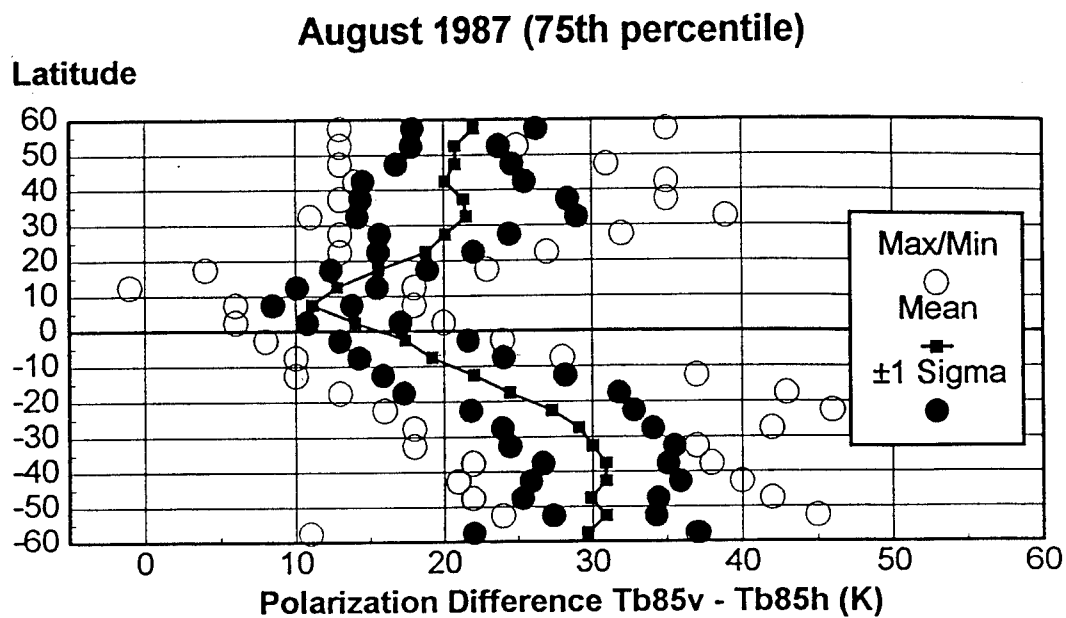


FIG. 22. Statistics comparing the latitudinal variability of the sensitivity distributions for August 1987 (top) and February 1993 (bottom) at the 75th percentile threshold.

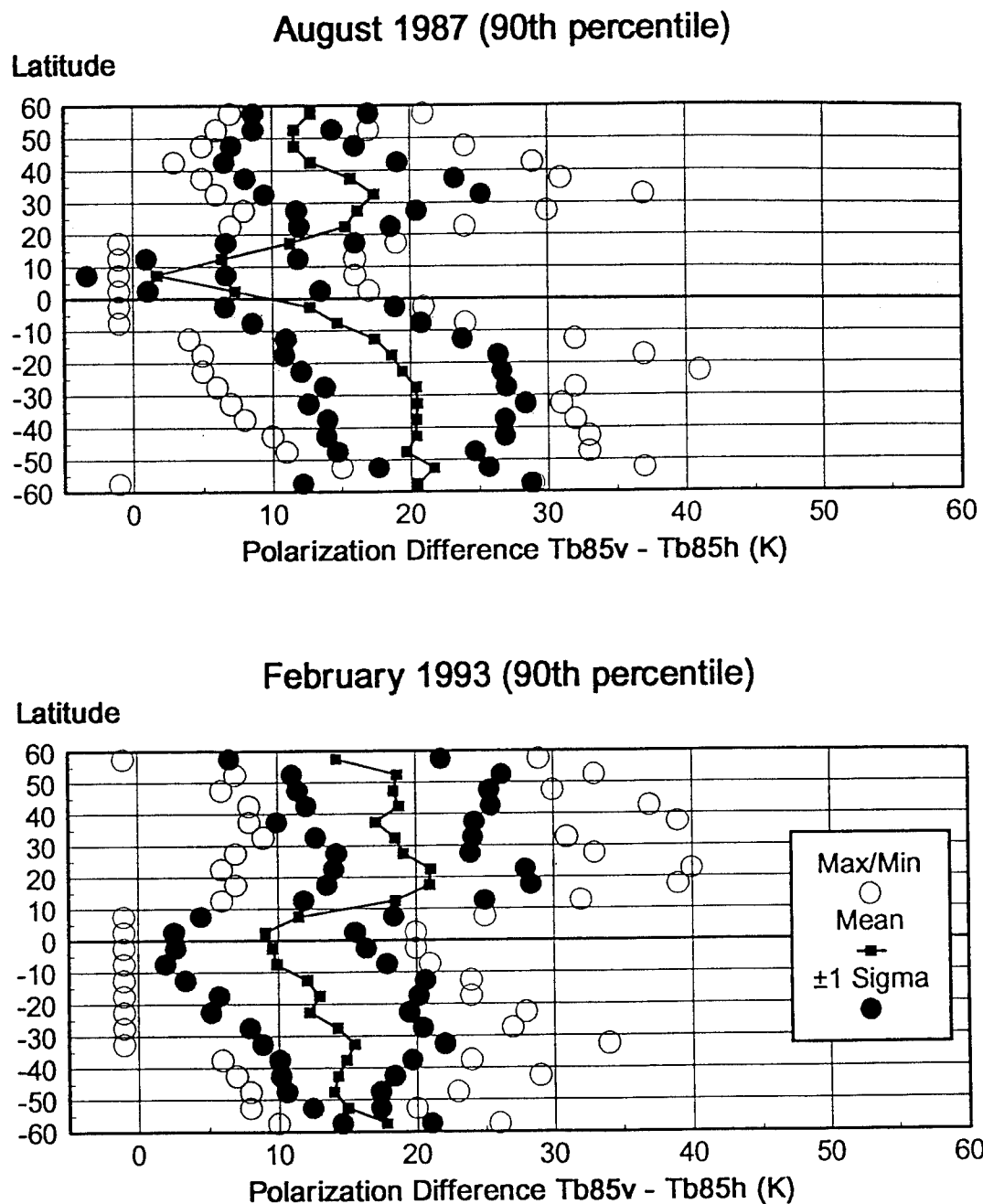


FIG. 23. Statistics comparing the latitudinal variability of the sensitivity distributions for August 1987 (top) and February 1993 (bottom) at the 90th percentile threshold.

several regions in the Northern Hemisphere are potential regions of sea ice formation: the Sea of Okhotsk (55 - 60° N, 150 - 155° E), Hudson Bay (55 - 60° N, 80 - 90° W), and the Gulf of St. Lawrence (45 - 50° N, 55 - 60° W). Examination of the individual scatterplots, such as Hudson Bay's (Fig. 6), reveal the characteristic scattering branch with little or no absorption based observations. As a result, none of the 4-parameter algorithms are expected to give reliable results for these regions.

At the 50th percentile (Fig. 17), the polarization differences for the extreme South Pacific Ocean in February exceed 25 K. This is in direct contrast to the August plot which depicts regions of decreasing ΔT_B 's in the South Pacific Ocean between 55 and 60° S. Sea ice does not extend that far north during southern summer (January-March). As a result, the more sensitive algorithms can be used in these regions at least 50% of the time.

At the 75th percentile (Fig. 18), two distinct differences emerge between the summer and winter plots. First, the polarization differences along the SPCZ have decreased significantly in February. Interestingly, this decrease exceeds the one shown for August. The rapidly decreasing ΔT_B 's are associated with the rapidly intensifying SPCZ during southern summer (Vincent 1994). Increased convergence producing denser (convective) clouds, rain, and ice particles adds to the atmospheric opacity so that only the least sensitive algorithms can be invoked.

The second difference involves the sharp contrast between the Northern and Southern Hemispheres. The regions with the largest polarization differences are associated with their respective winter hemisphere. Subsidence, fewer clouds, and decreased rainfall are associated with large areas of high pressure. This leads to relatively optically transparent atmospheric conditions. As a result, the more sensitive algorithms (>25 K) are usable at least 75% of the time over the winter hemisphere oceans.

As with all the global maps, the trend of decreasing ΔT_B 's continues through the 90th percentile (Fig. 19). The most striking feature for comparison involves the SPCZ. During February, the convective intensity throughout the SPCZ is much

greater than August. As a result, even the least sensitive algorithms (0-5 K) are not usable in the SPCZ during southern summer. However, at least 90% of the time, the majority of the remaining global oceanic regions are usable for algorithms with sensitivity thresholds above 5 K.

Comparing latitudinal variability between seasons (Figs. 20-23) yields some distinct similarities and differences. At the 10th percentile (Fig. 20), both graphs show strong symmetry between hemispheres. In both cases, the winter hemisphere is associated with larger mean ΔT_B 's. Additionally, both seasons show a rapid decrease of polarization differences with decreasing latitude. The graphs depicting the seasonal variability at the 50th percentile (Fig. 21) continue to show strong hemispheric symmetry with the exception of the region north of 40°N during February. Here, a reverse of the decreasing ΔT_B 's with decreasing latitude is noted.

There are two possible explanations for this discrepancy. First, several regions of sea ice are present (as observed by the presence of several regions of extremely low minimum ΔT_B values). The arithmetic mean values are lower than expected since the mean is strongly influence by these outliers. Another potential contributor to the reverse ΔT_B trend is associated with the weather regime. Sufficient numbers of transient extratropical cyclones traversing these northern latitudes could effectively lower the ΔT_B 's due to their extensive cloud shields and associated precipitation.

The overall decrease in ΔT_B 's continues throughout the 75th and 90th percentile thresholds (Figs. 20 and 21).

CHAPTER V

REGIONAL SENSITIVITY STUDY

1. Enlarging the T_B 85 GHz FOV

As mentioned in Chapter I, the SSM/I's and MIMR's measurement geometries are such that there are many high resolution T_B 85-90 observations distributed around the low resolution channels. Selecting the appropriate algorithm for a particular parameter will be driven by the *lowest* value ΔT_B observed at high resolution within the low channel's FOV.

In general, the smaller the ΔT_B value the more robust the algorithm needs to be. Unfortunately, a robust algorithm implies a relatively large uncertainty in the retrievals compared to those found in more sensitive algorithms. Nelkin (1992) determined the uncertainties associated with the 4 - parameter algorithms as a function of the minimum 85-90 GHz ΔT_B (Table 3). As a result of a subsequent error found with his random number generator, the uncertainty values have been increased by a factor of 1.5 to compensate for the discrepancy.

Since we are taking the minimum ΔT_B , if there is any variability in the observations, the sensitivity distributions will shift downward. Also, because the extent of this degradation is not known, a procedure to simulate decreasing 85 GHz channel resolution is presented.

This procedure involves analyzing progressively larger groups of collocated T_B 85 observations. Groups of 4 (2 along-scan x 2 cross-scan), 16 (4 x 4), and 64 (8 x 8) are chosen since these figures are multiples of the number of total observations (128) sampled along a scan line. Thus, data manipulations and calculations are performed without the need to incorporate any type of weighting or averaging scheme to account for any 'left over' observations. It is of interest to note that groups of 4 and 16 have comparable resolutions with the 37 and 22 GHz channels respectively. The group of 64 compares favorably to the resolution that a 10.65 GHz channel would have.

TABLE 3. 4 - parameter algorithm sensitivities as a function of polarization difference. Sensitivity values taken from Nelkin (1992) and adjusted to compensate for errors in his random number generator.

Min. 85-90 GHz ΔT_B (K)	PW (kg/m ²)	CLW (kg/m ²)	SST (K)	WS (m/s)
0	1.740	.069	1.357	2.51
18	1.035	.041	1.152	1.90
20	1.005	.039	1.153	1.85
22	0.975	.038	1.122	1.76

Once observations are grouped, the pair with the smallest ΔT_B (from a group of 4, 16, or 64) is identified. This pair indicates the area (85 GHz FOV) containing the most opaque atmosphere within that group. The remaining pairs in the group are dropped from further analysis, while the smallest ΔT_B value is retained to represent the total area (FOV) covered by the group. The latitude and longitude of the low channel (A-scan) observation point corresponding most closely to the group's geographic center is then assigned this ΔT_B value. Based on the assigned latitude and longitude, the ΔT_B value is then placed into the appropriate 5 x 5 degree box. From this point on, the data are processed in the manner described in Chapter III.

Figures 24, 25, and 26 illustrate the scan geometry of the SSM/I. However, it should be noted that they are not drawn precisely to scale and that the actual scans are conical, not linear. Large X's denote locations where the radiometer records observations for all seven channels. Small X's indicate locations where only the 85 GHz channels are sampled. Small ovals, encircling individual observation points, depict the approximate spatial resolution of the 85 GHz channels (15 km). Large ovals illustrate the approximate 37 and 22 GHz FOV's (37 x 38 km and 60 x 47 km, Figs. 24 and 25, respectively). Shaded ovals (dark and light) designate observation locations representing specific groups (4, 16, or 64). The dark shaded ovals indicate the low channel observation point selected to represent the geographic center of the group. The relative horizontal resolutions of the 19, 10, and 6 GHz channels (69 x 50 km, 120 x 85 km, and 190 x 120 km, respectively) are compared to each other and overlaid onto a group of 64 (Fig. 26).

The precise center of a group does not directly correspond to an observation point since the groups are composed of an even number of 'rows' and 'columns' (cross-scan and along-scan). However, aggregate FOV's composed of various 85 GHz groups compare favorably with low channel FOV's. Figure 24b shows the approximate 37 GHz FOV and its adjoining 85 GHz observations. It appears that as many as nine 85 GHz FOV's (totally or partially) are incorporated within the 37's FOV. However, by

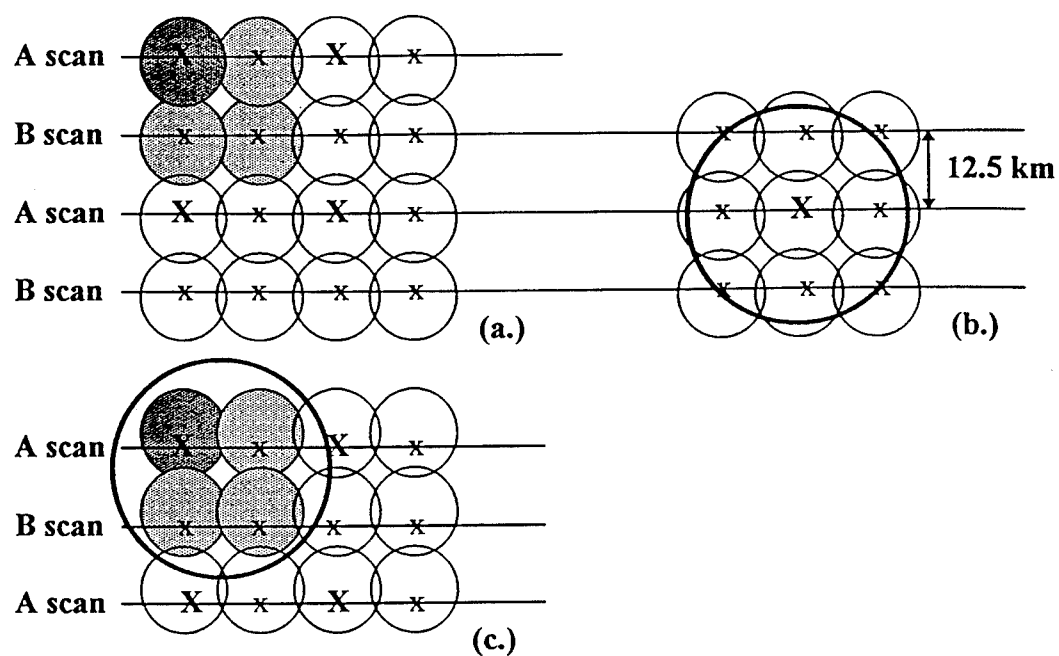


FIG. 24. Simplified scan geometry of the SSM/I with relative FOV's for 37 and 85 GHz. Group of 4 T_B 85 FOV's highlighted in (a). T_B 37 FOV overlaid onto several T_B 85 FOV's to show relative area coverage (b). T_B 37 FOV compared to a group of 4 T_B 85 FOV's (c).

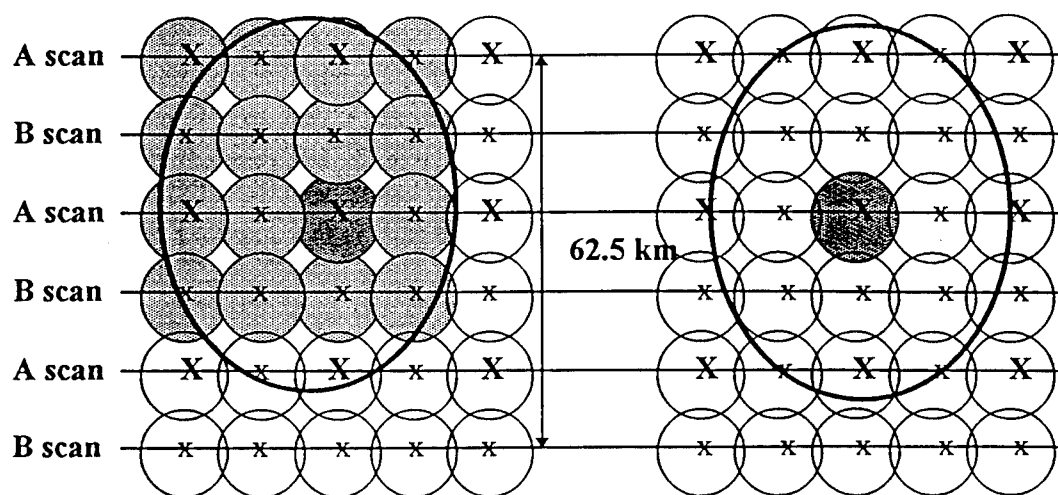


FIG. 25. Simplified scan geometry of the SSM/I with relative FOV's for 22 and 85 GHz. Group of 16 T_B 85 FOV's compared to a T_B 22 FOV (left panel). T_B 22 FOV overlaid onto several T_B 85 FOV's showing relative area coverage (right panel).

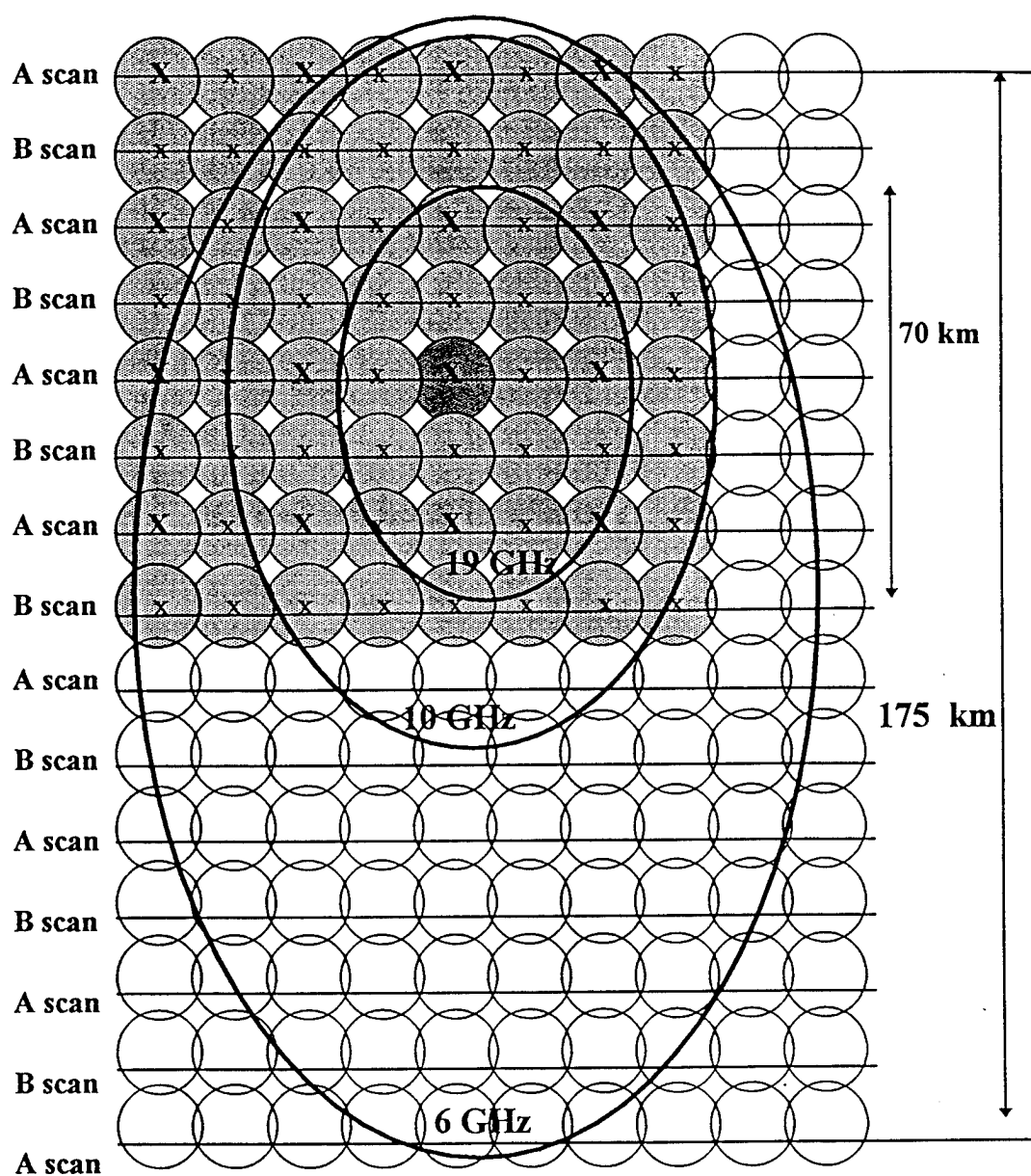


FIG. 26. Simplified scan geometry of the SSM/I with relative FOV's for 6, 10, 19, and 85 GHz. Group of 64 T_B 85 FOV's compared to T_B 19, 10, and 6 FOV's.

centering the 37 GHz FOV on a group of four (Fig. 24c), it is apparent that the total 85 GHz coverage is comparable to the 37's FOV. Similarly, as many as twenty-one 85 GHz FOV's are completely or partially enclosed within the 22 GHz FOV (Fig. 25b). Once again, by centering the 22 GHz FOV on a group of 16 (Fig. 25a), it can be seen that a group of 16 has an equivalent resolution to the 22 GHz channel.

Finally, the 19, 10, and 6 GHz FOV's are overlaid onto a group of 64 (Fig. 26). The area covered by this group compares most closely with that of the 10 GHz FOV, while the majority of the 6 GHz channel FOV is represented.

Since the 10 and 6 GHz channels are not supported by the SSM/I, their respective resolutions are determined from the existing SSM/I channels and then scaled based on their wavelengths. Holding all other factors constant, such as slant range (distance from the radiometer to the ground observation point) and antenna aperture diameter, there exists a nearly linear relationship between wavelength and resolution. Specifically, resolution increases (smaller FOV) as wavelength decreases. Although resolutions will increase (by a factor of 2 - 3 times) aboard the MIMR, the channels relative resolutions will remain nearly constant. Therefore, the conclusions resulting from this experiment can be used in a simulation study for the performance of the MIMR.

2. Effects of enlarging the FOV

Since the 37 GHz resolution (group of 4) is coarser than the 85 GHz, we see a degradation of sensitivities (progressively lower ΔT_B 's) throughout the entire globe (Figs. 27 and 28). Similarly, groups of 16 yield further declines in the global sensitivity distributions (Figs. 29 and 30), while groups of 64 have the least sensitive (most opaque) distributions (Figs. 31 and 32).

These global portrayals of the 85 GHz sensitivity distributions are primarily qualitative in the sense that they show large-scale atmospheric weather features (in terms of atmospheric opacity or optical depth) associated with both cloud mass and

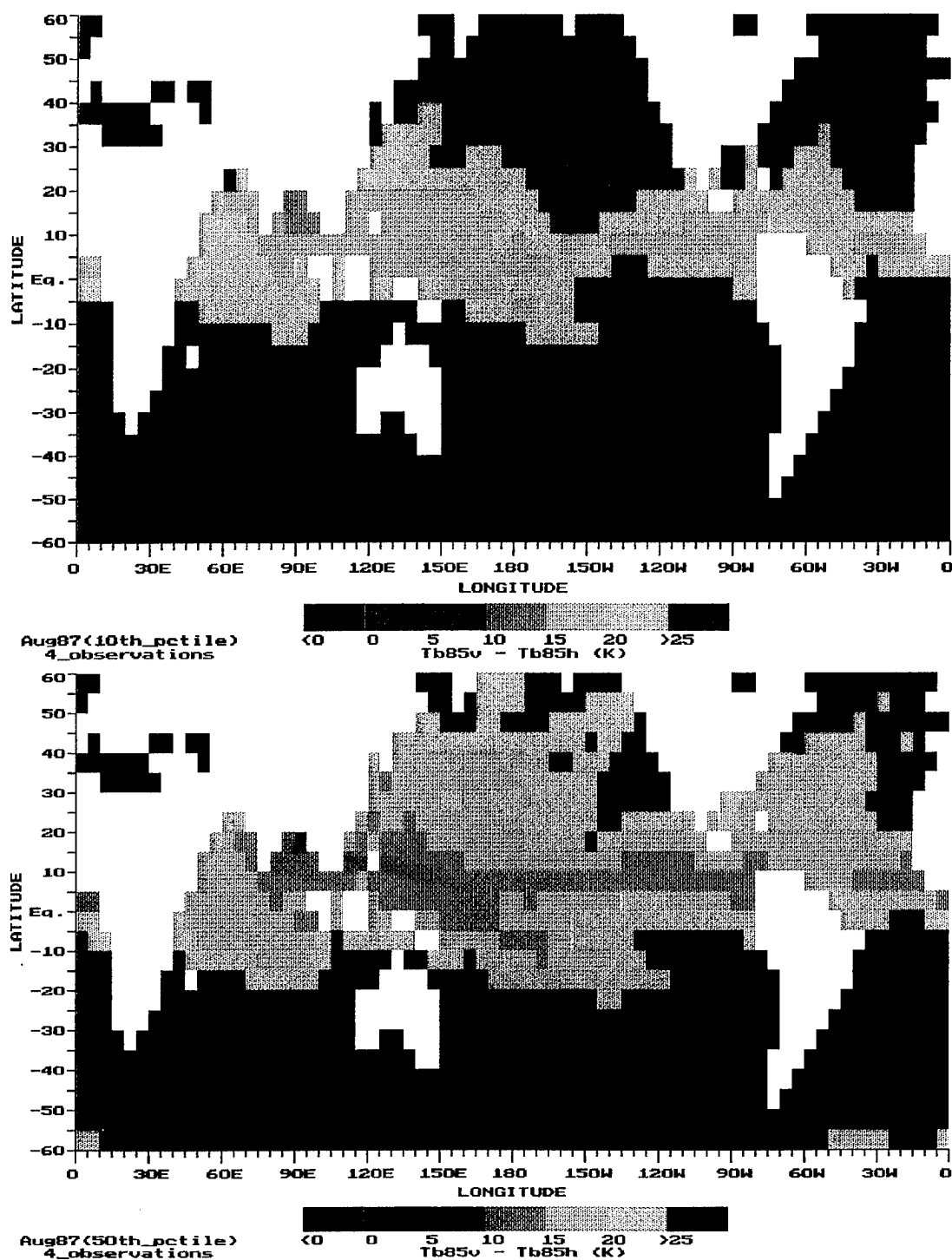


FIG. 27. Global sensitivity maps depicting groups of 4, T_B 85 GHz observations and their resulting polarization difference values at the 10th (top) and 50th (bottom) percentile thresholds for August 1987.

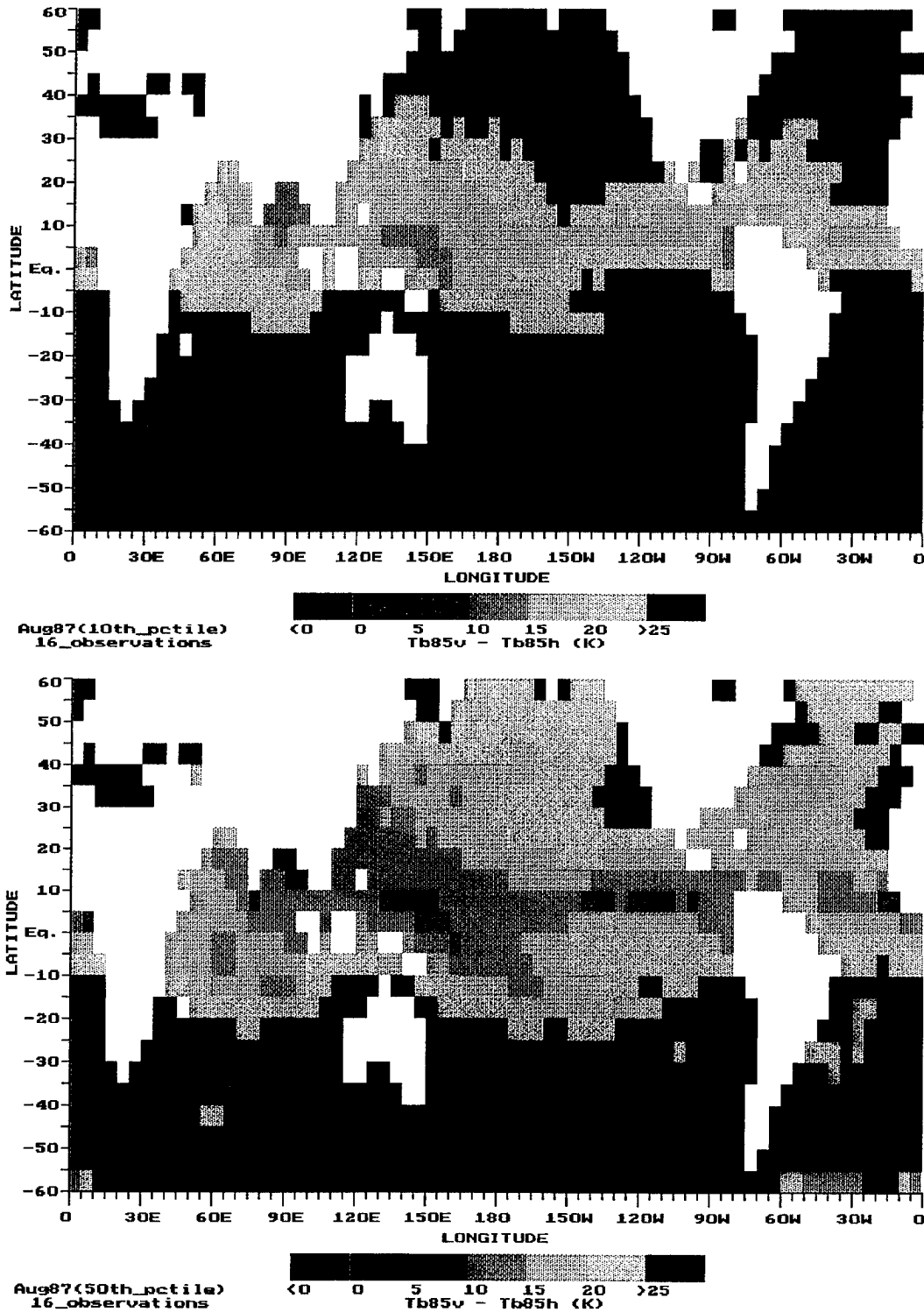


FIG. 29. Global sensitivity maps depicting groups of 16, T_B 85 GHz observations and their resulting polarization difference values at the 10th (top) and 50th (bottom) percentile thresholds for August 1987.

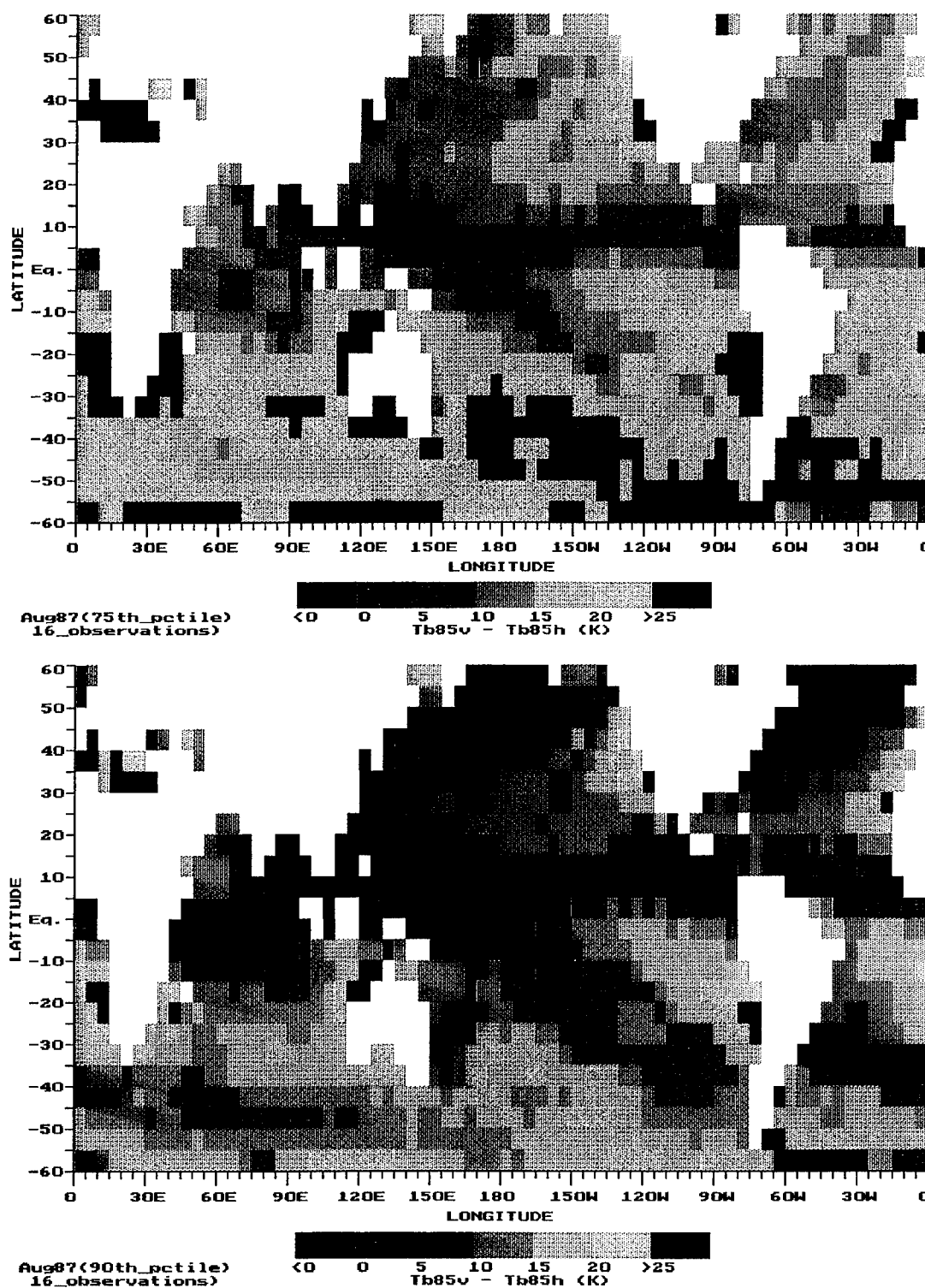


FIG. 30. Global sensitivity maps depicting groups of 16, T_B 85 GHz observations and their resulting polarization difference values at the 75th (top) and 90th (bottom) percentile thresholds for August 1987.

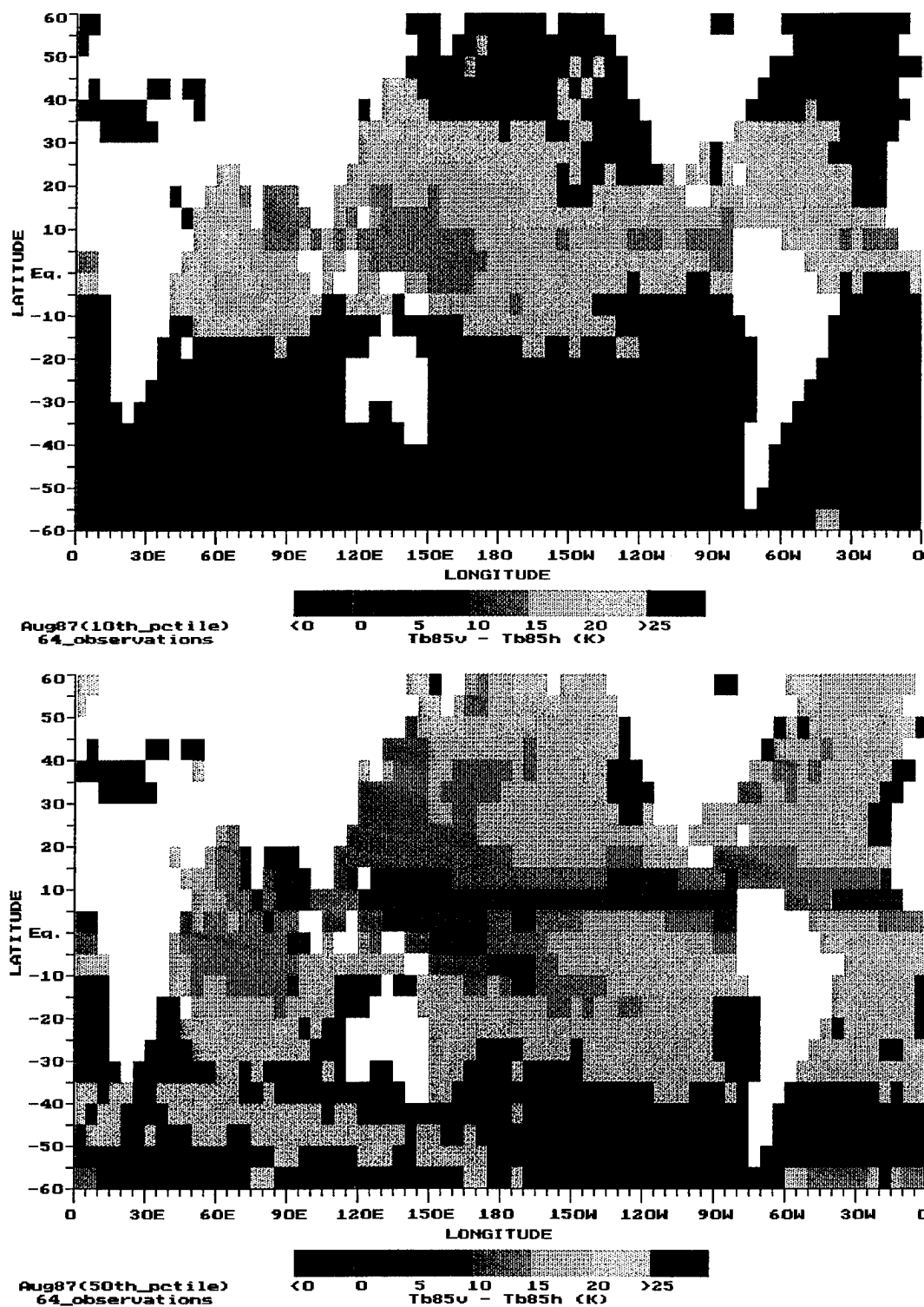


FIG. 31. Global sensitivity maps depicting groups of 64, T_B 85 GHz observations and their resulting polarization difference values at the 10th (top) and 50th (bottom) percentile thresholds for August 1987.

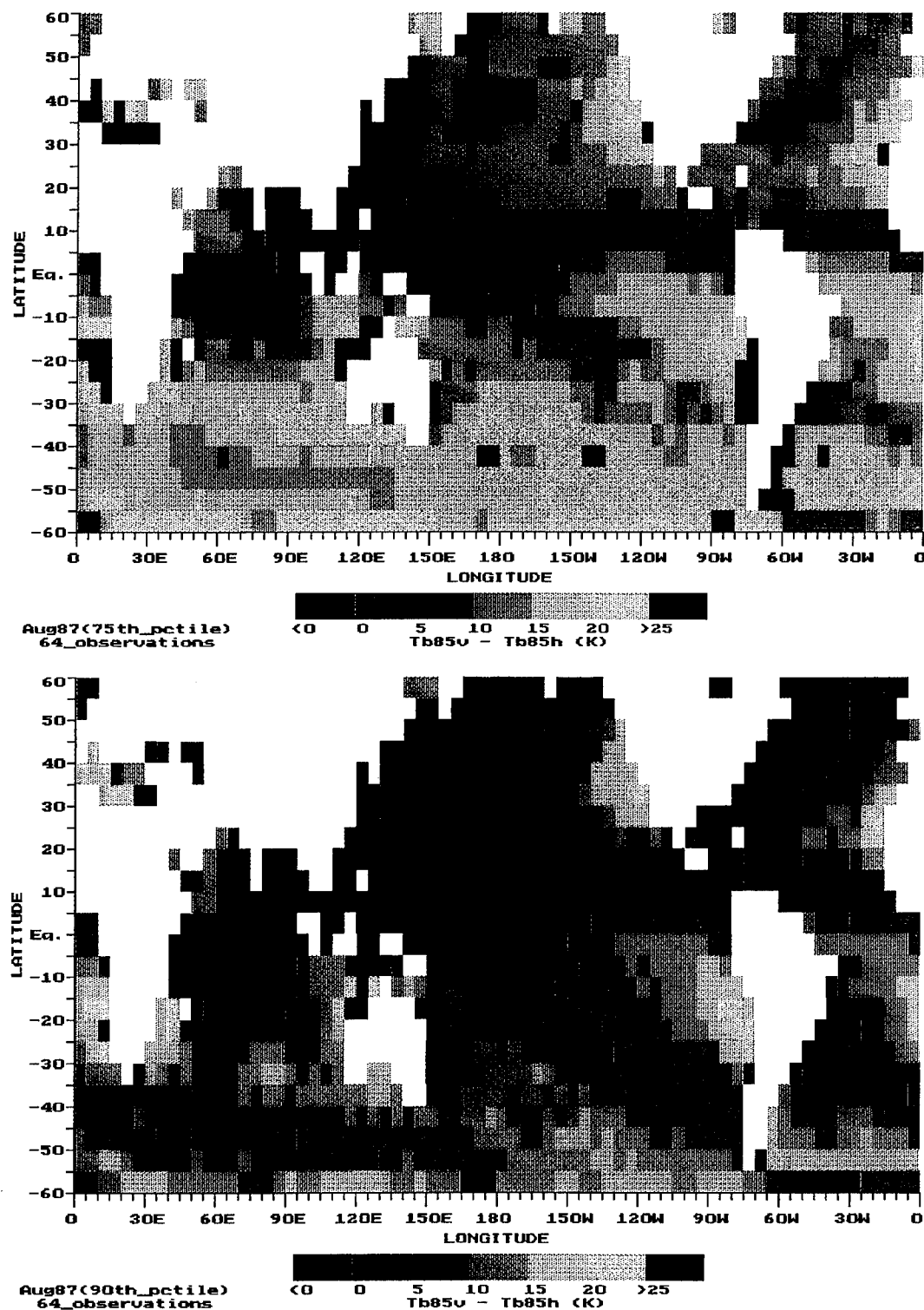


FIG. 32. Global sensitivity maps depicting groups of 64, T_B 85 GHz observations and their resulting polarization difference values at the 75th (top) and 90th (bottom) percentile thresholds for August 1987.

water vapor. The progressive degradation of the sensitivity distributions is a direct result of selecting the smallest ΔT_B value to represent increasingly larger groups of T_B 85 observations and their correspondingly larger FOV's.

Similar to the cases where every available T_B 85 observation is utilized to create global sensitivity maps (Figs. 16-19), the trend of decreasing ΔT_B 's (from the 10th through 90th percentile thresholds) is evident no matter what group size is chosen.

This is due to the manner in which ΔT_B 's are computed and has no other significant meaning, physical or otherwise. However, the trend of decreasing ΔT_B 's, between the various group sizes as evidenced from the global profiles in figures 27-32, has physical meaning. To some extent, these figures show how changing wavelengths affects resolution which, in turn, affects the sensitivity distributions. The exact quantitative measure of this wavelength/resolution effect cannot be determined from these global maps.

Once again, an alternative method for displaying the results can be shown in terms of the latitudinal variability of the polarization differences (Figs. 33-40). This time, the attention is focused on comparing the intralatitude variability ($\pm \sigma$ from the mean) between the various T_B 85 group sizes at specific percentile thresholds. For example, Figs. 33 and 34 depict the latitudinal variability of the polarization difference at the 10th percentile. Figure 33 contains the graphs of all T_B 85 observations and groups of four during August 1987. Figure 34 contains the graphs for groups of 16 and 64 during the same period. Assuming a normal or near normal distribution of ΔT_B 's along a given latitude belt, an interval of $\pm \sigma$ accounts for approximately 68% of the total observations (Ott 1993) along that latitude. This allows for a more quantitative assessment of the impact that resolution plays on the sensitivity distributions.

Small differences exist between the graphs in Fig. 33 that represents a decrease in resolution by approximately a factor of 2 (when considering the 4-observation graph).

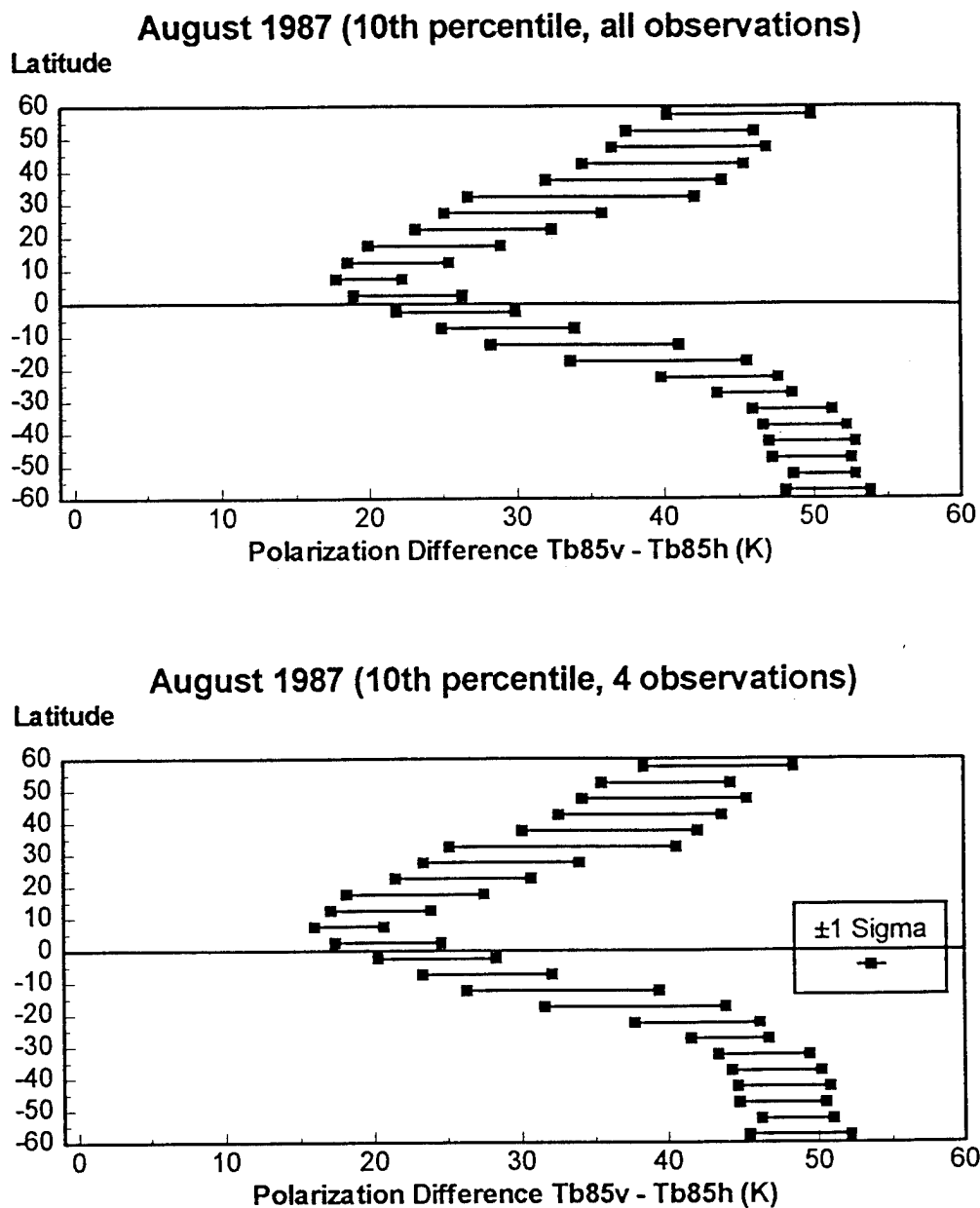


FIG. 33. Latitudinal variability of the T_B 85 GHz polarization differences at the 10th percentile threshold for August 1987 (all T_B 85 observations (top) and groups of 4 (bottom)). Variability is ± 1 standard deviation from the mean.

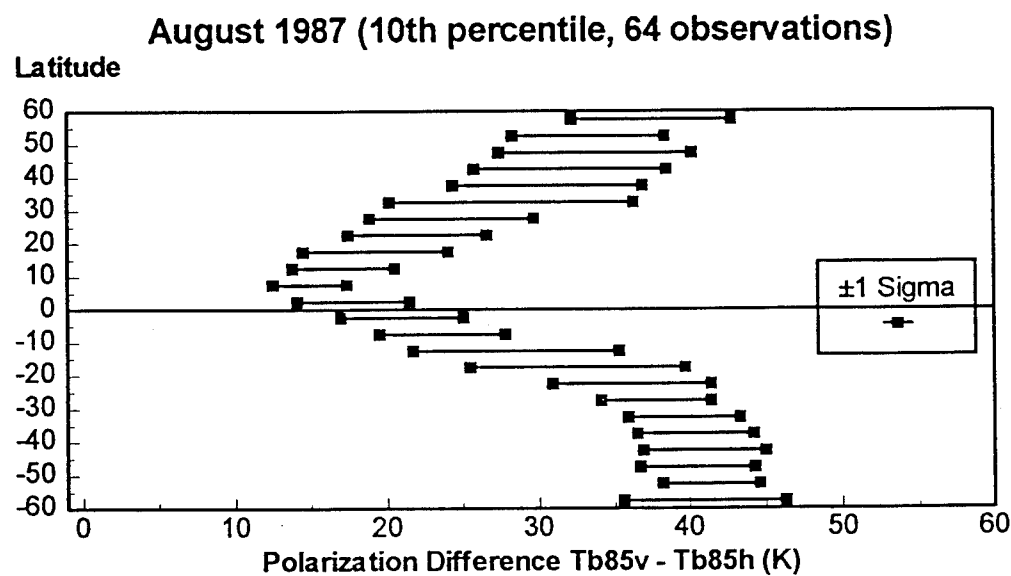
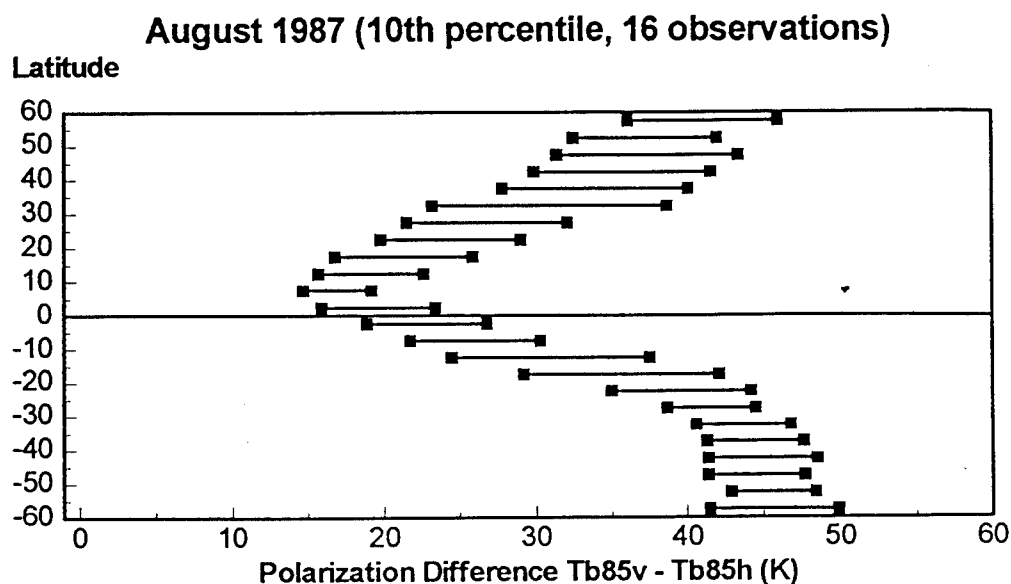


FIG. 34. Latitudinal variability of the T_B 85 GHz polarization differences at the 10th percentile threshold for August 1987 (groups of 16 (top) and 64 observations (bottom)). Variability is ± 1 standard deviation from the mean.

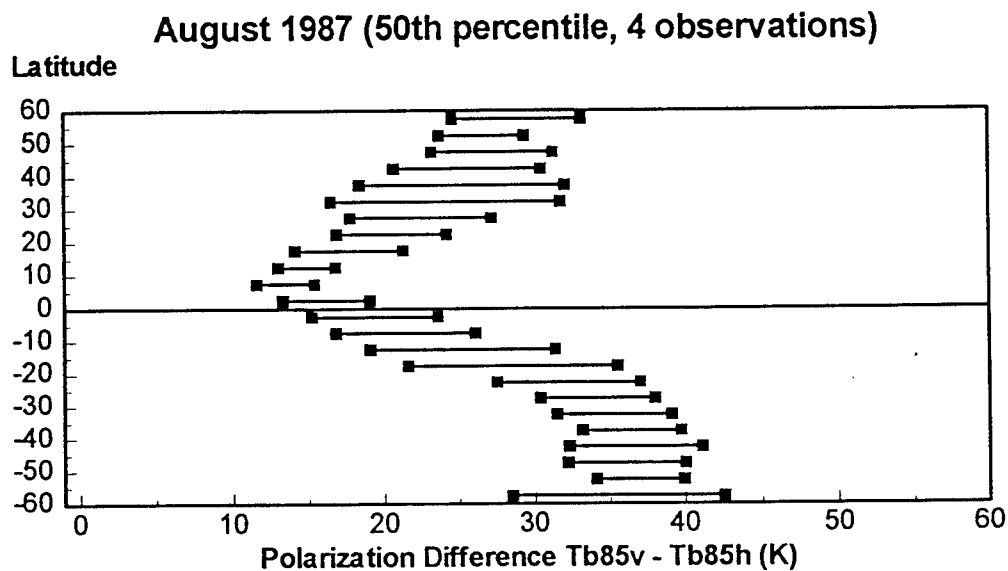
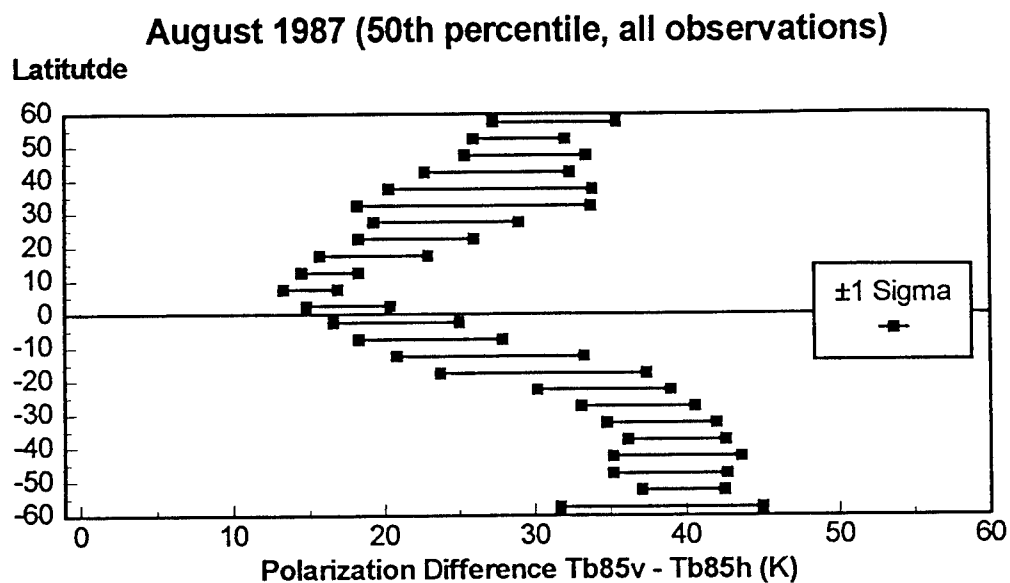


FIG. 35. Latitudinal variability of the T_B 85 GHz polarization differences at the 50th percentile threshold for August 1987 (all T_B 85 observations (top) and groups of 4 (bottom)). Variability is ± 1 standard deviation from the mean.

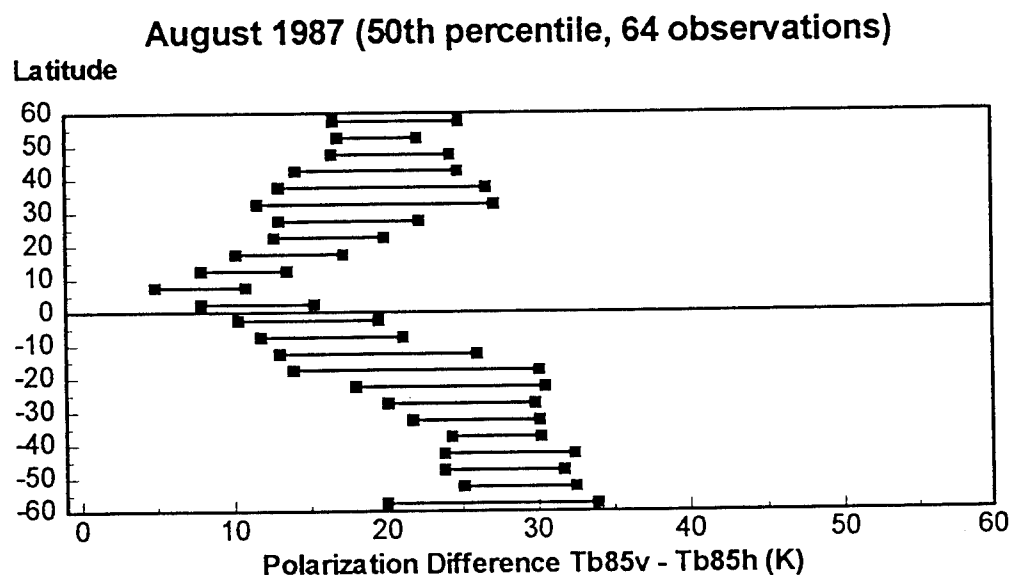
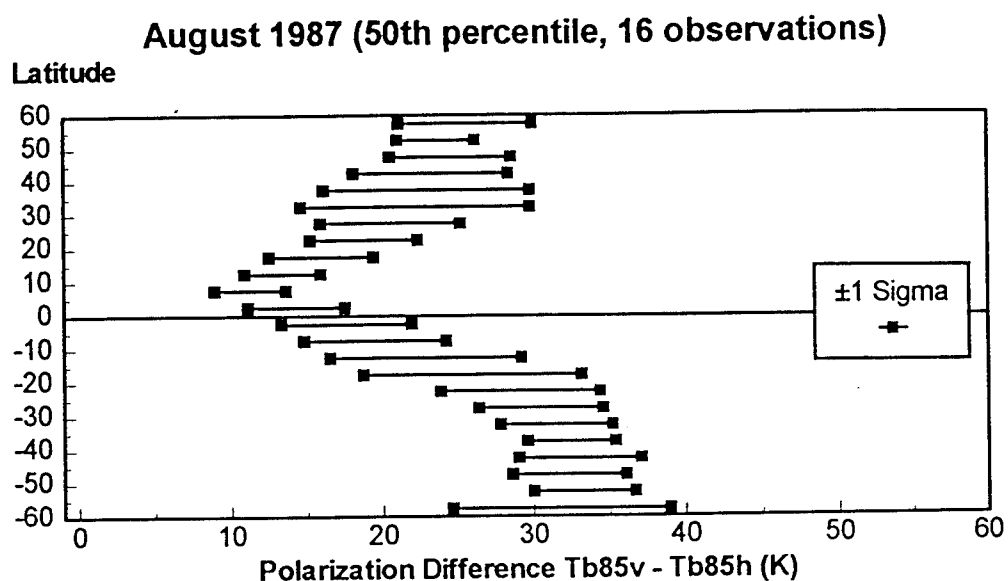


FIG. 36. Latitudinal variability of the T_B 85 GHz polarization differences at the 50th percentile threshold for August 1987 (groups of 16 (top) and 64 observations (bottom)). Variability is ± 1 standard deviation from the mean.

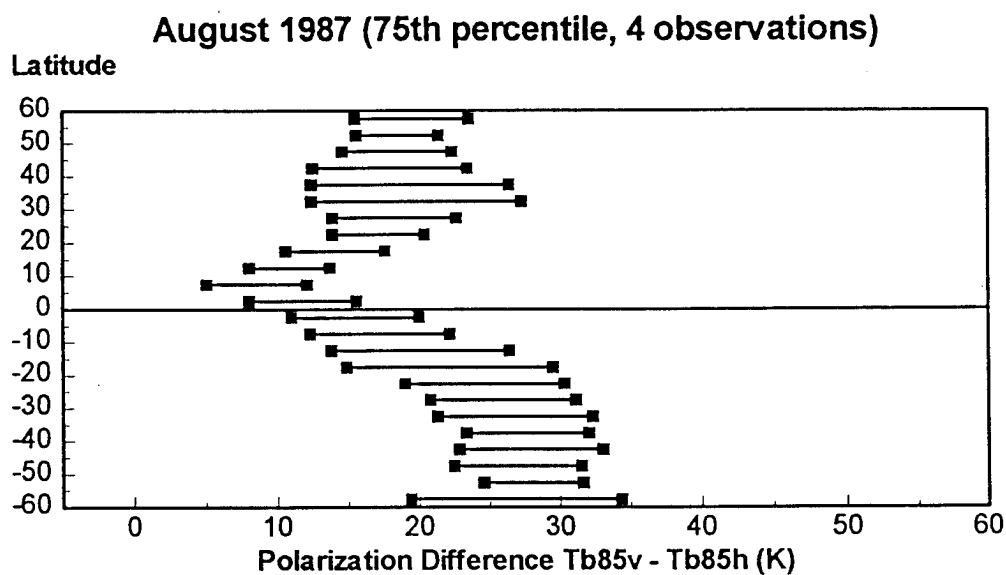
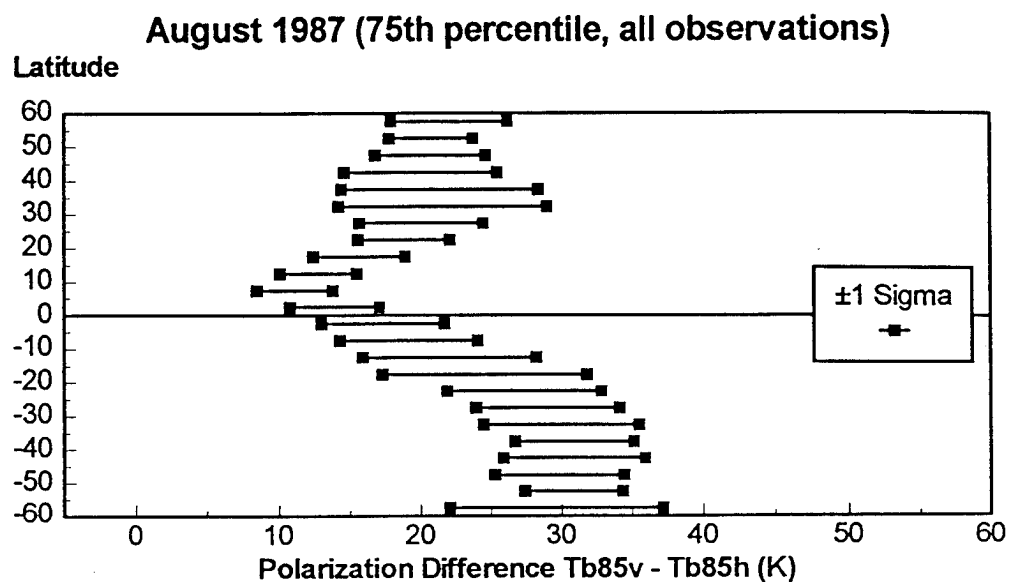


FIG. 37. Latitudinal variability of the T_B 85 GHz polarization differences at the 75th percentile threshold for August 1987 (all T_B 85 observations (top) and groups of 4 (bottom)). Variability is ± 1 standard deviation from the mean.

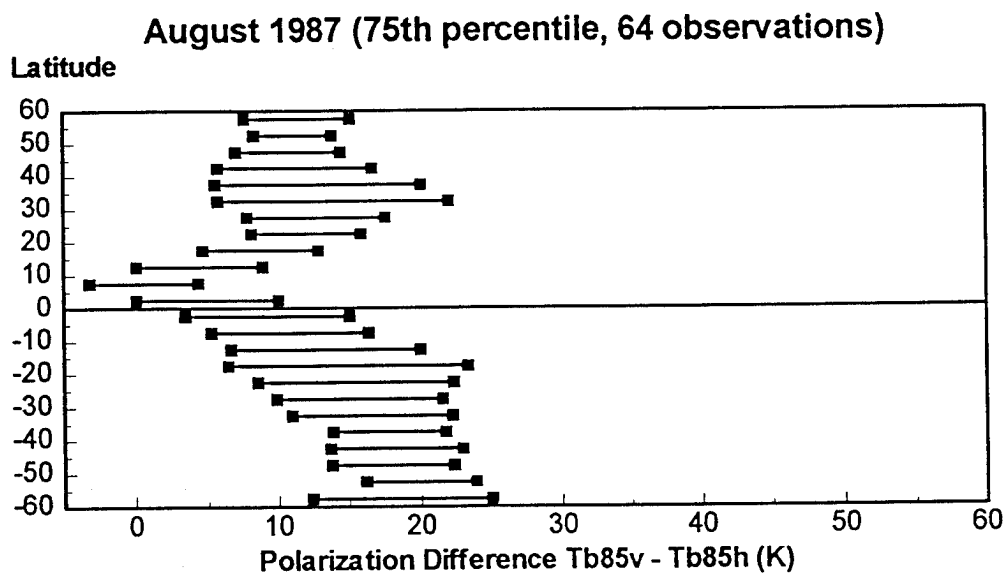
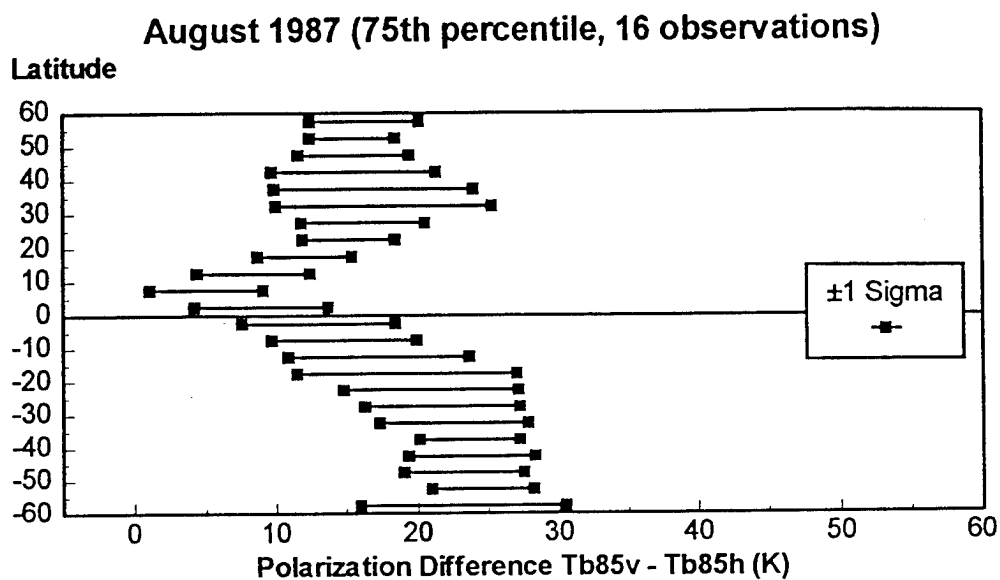


FIG. 38. Latitudinal variability of the T_B 85 GHz polarization differences at the 75th percentile threshold for August 1987 (groups of 16 (top) and 64 observations (bottom)). Variability is ± 1 standard deviation from the mean.

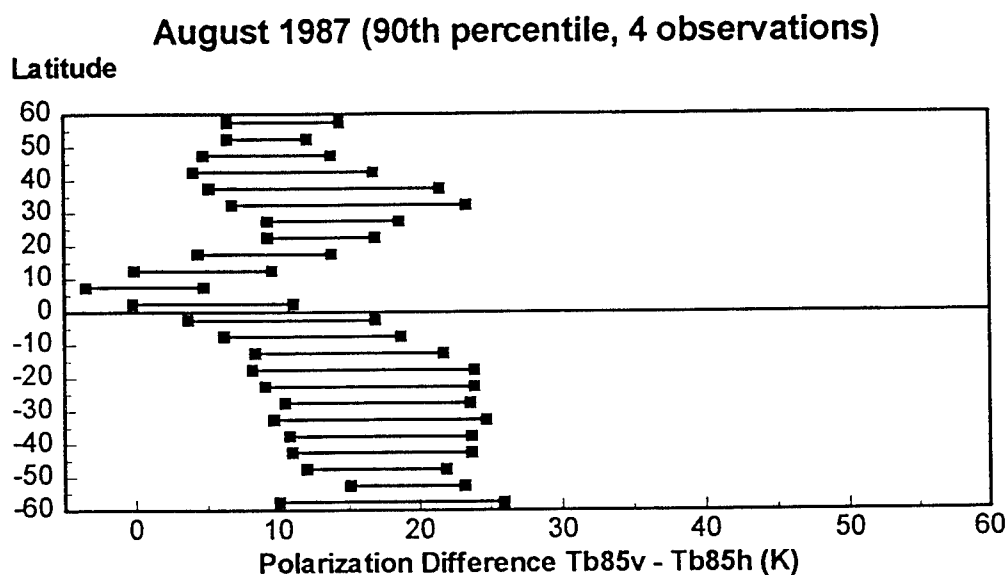
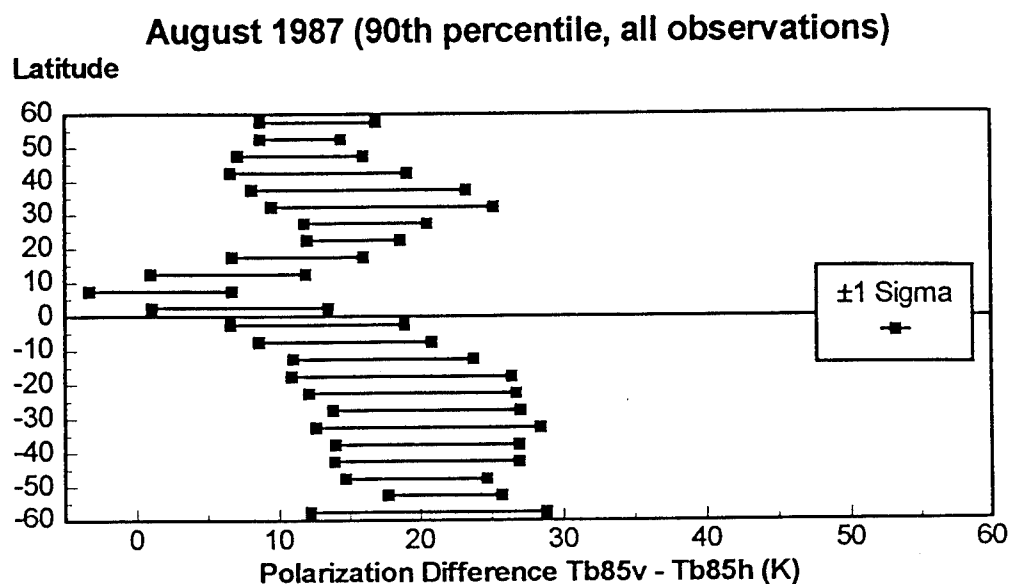


FIG. 39. Latitudinal variability of the T_B 85 GHz polarization differences at the 90th percentile threshold for August 1987 (all T_B 85 observations (top) and groups of 4 (bottom)). Variability is ± 1 standard deviation from the mean.

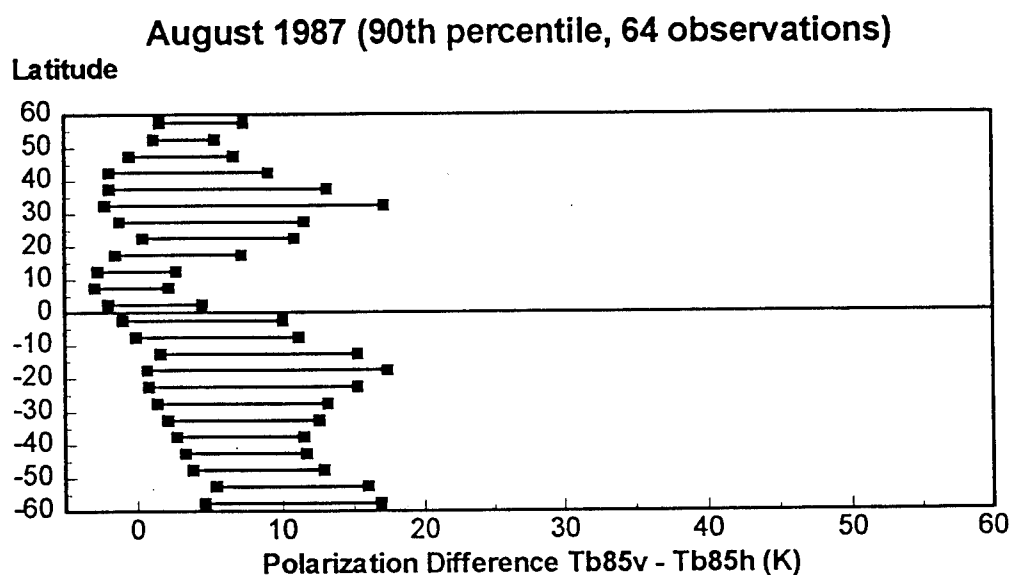
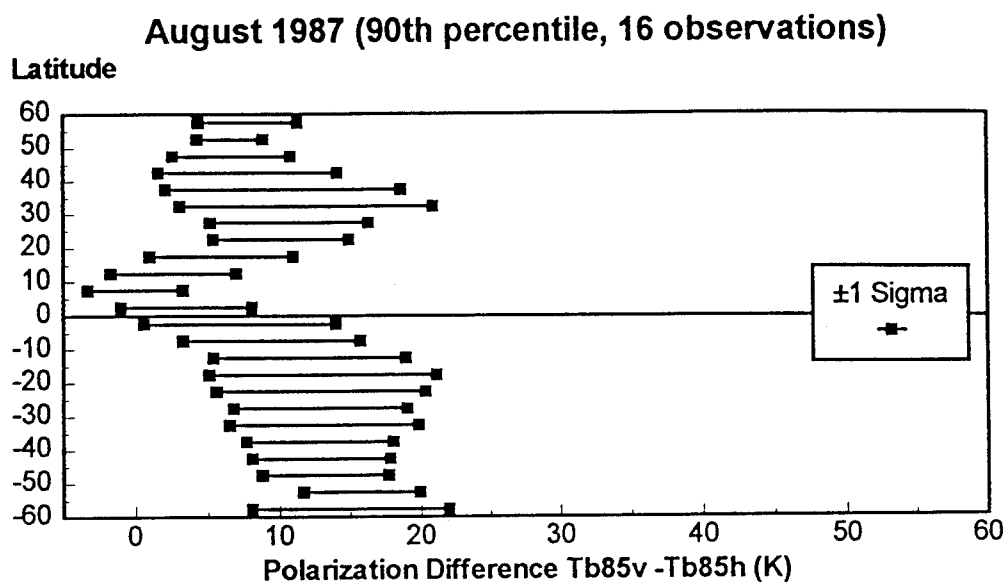


FIG. 40. Latitudinal variability of the T_B 85 GHz polarization differences at the 90th percentile threshold for August 1987 (groups of 16 (top) and 64 observations (bottom)). Variability is ± 1 standard deviation from the mean.

The main difference involves a shift towards lower ΔT_B values. On average, the shift is less than 5 K. This implies that resolution does not severely impact the overall characteristics of the sensitivity distributions. Further decreases of resolution (Fig. 34) yield similar results because the sensitivity distributions are not significantly altered even by resolutions only 1/8 the original. The hemispheric symmetry remains intact while the intralatitude variability remains fairly constant. The ITCZ regions display the smallest intralatitude variability regardless of the resolution while the subtropical regions show the largest.

The trend of decreasing ΔT_B 's with decreasing resolution continues for all remaining percentile thresholds. This is not a new discovery; however, the graphs show that, on average, the polarization difference decreases no more than 10 K between the all-observation cases and the 64-observation cases irrespective of the percentile threshold.

Finally, three regions that were selected for their differing and diverse atmospheric regimes, were analyzed to determine the exact extent resolution influences sensitivity distributions. For each region, polarization difference vs. percentile threshold was plotted for all four T_B 85 group sizes (total, 4, 16, and 64 observations)(Fig. 41) during August 1987.

All three regions are located in the North Atlantic. The first region is between 40 and 45°N and 30-35°W. It is representative of the midlatitude regions where large differences in cloud coverage and water vapor can be found daily due to transient extratropical cyclones migrating with the polar jet stream. This weather regime implies a large variability in the polarization differences. The four midlatitude group plots have the least steepest slopes of the three selected regions which is indicative of a large polarization difference variability. The degradation of the polarization differences across the range of resolutions is minimal; it is less than 10 K at the 10th percentile to approximately 12 K at the 90th percentile. Considering the lowest resolution profile, moderately sensitive algorithms ($\Delta T_B > 10K$) can be used 80% of the time in this region.

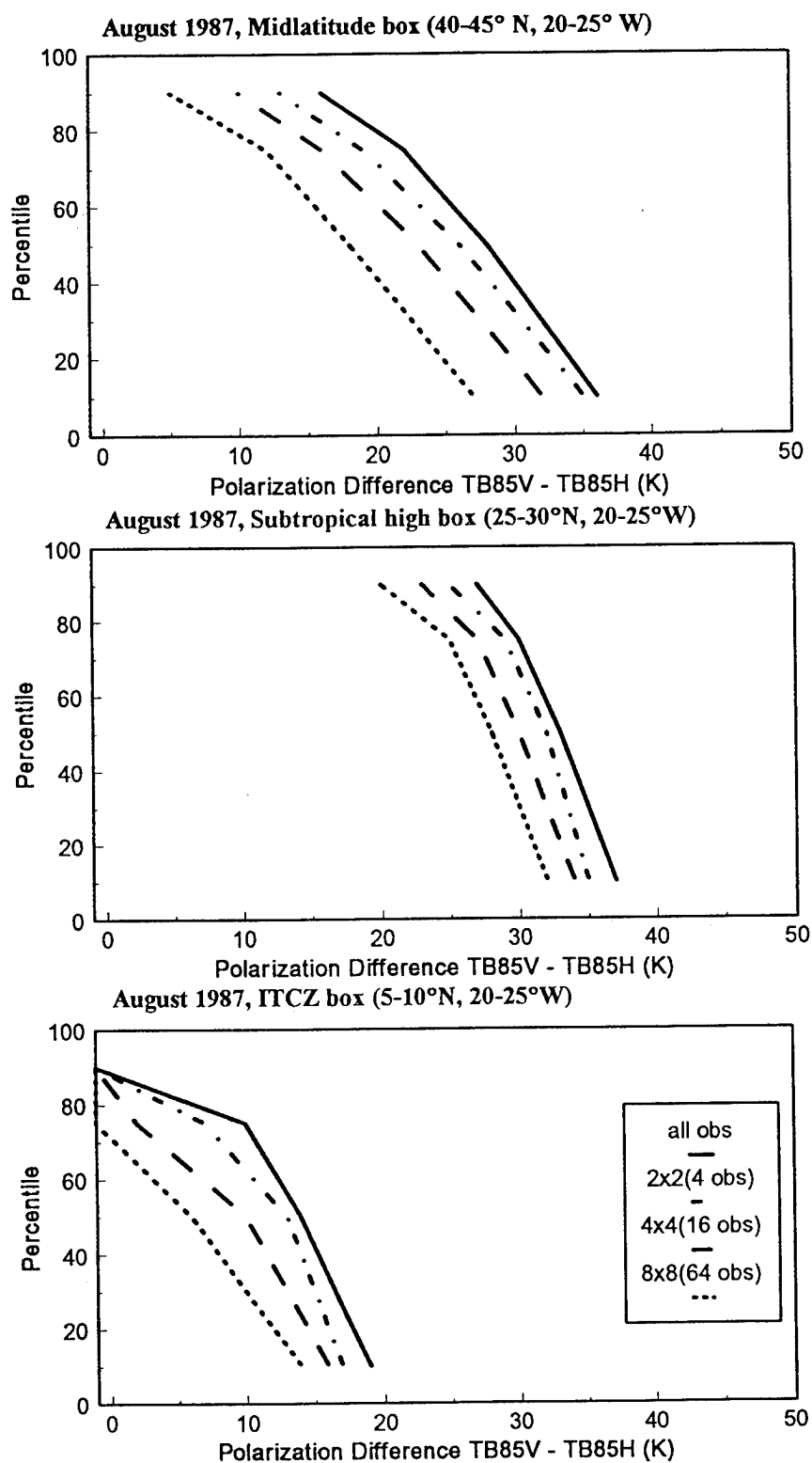


FIG. 41. Regional analysis comparing resolution effects on sensitivity distributions as a function of climate regime.

The second region is located between 25 and 30°N and 20-25°W. This region is representative of the subtropical high belt where rain and dense clouds are minimal due to large areas of subsidence. As a result of the semi-permanent high pressure systems there exists less atmospheric variability in these regions. The second graph, in Fig. 41, shows relatively small ΔT_B variabilities compared to the midlatitude plots, indicated by the larger slopes of all four group plots. Also, the plots are significantly less opaque evidenced by their larger ΔT_B values.

Finally, the degradation of the polarization differences across the range of resolutions is extremely small; it is less than 10 K at every percentile. Because of the relatively small atmospheric opacity in Subtropical Highs, the most sensitive algorithms can be used nearly all of the time.

The third region is located between 5-10°N and 20-25°W). This region is representative of the tropics, specifically, the ITCZ, which is characterized by strong upward motion associated with low level convergence of the northeast and southeast trade winds. The existence of ample water vapor, dense convective clouds, and heavy rainfall, creates a relatively opaque atmosphere throughout the ITCZ. This large opacity is manifested by relatively small ΔT_B values in all four plots of the third graph (Fig. 41). CLW and PW variability is the smallest of the three regions even though their absolute quantities are the greatest. The relatively small variability of CLW and PW is characterized by extremely steep slopes (as seen in the third graph).

Finally, the degradation of polarization differences is problematic since it appears that none of the plots are valid at the 90th percentile. Since atmospheric opacity is relatively large, robust algorithms must be used the majority of the time. The increased resolution capabilities of the MIMR should alleviate this situation somewhat.

It is reasonable to conclude from this exercise that the degradation of the ΔT_B values resulting from decreased resolutions is not significant between frequencies (on the order of 10 K). Incorporating the 6 and 10 GHz channels should not adversely affect the quality of the retrievals for SST and WS.

CHAPTER VI

DISTRIBUTION OF CLOUD LIQUID WATER

1. Multi-frequency retrieval algorithm

The second objective of this study was to understand and explain the sensitivity distributions in terms of the CLW distributions over selected oceanic areas containing nonprecipitating clouds. To accomplish this, an operational CLW algorithm from the Calibration/Validation studies (Alishouse et al. 1990) was selected.

Their algorithm is of the D-matrix type; however, they used surface-based measurements to derive new matrix coefficients. The retrieval algorithm (1) is linear in brightness temperature and is configured for 4 channels. It is in the form $CLW = a_0 + \sum a_i * T_{Bi}$ ($i = 1, 2, \dots, 7$), where the a_i 's are the matrix coefficients and the T_{Bi} 's are the brightness temperatures associated with a specific channel. The final algorithm is:

$$CLW (kg/m^2) = -3.14559 + 6.0257E - 3 * 19H - (4.8803E - 3 * 22V) + (1.9595E - 2 * 37V) - (3.0107E - 3 * 85H) \quad (1)$$

2. Regional cloud liquid water distributions

Four regions (corresponding to the climate zones in Table 2) were selected to serve as test cases for the algorithm's output: a high latitude box extending from 55-60°N and 20-25°W, a midlatitude box extending from 40-45°N and 20-25°W, a subtropical high box extending from 25-30°N and 20-25°W, and a tropical box extending from 10-15°N and 20-25°W. These regions were identified because they represented a wide range of weather regimes.

The pairs of T_B 85 observations and their corresponding lower channel observations that were previously categorized as belonging to the absorption branch were injected into the algorithm. This was done to assure that retrieved values of

CLW were associated with nonprecipitating clouds or, at worst, clouds with very little precipitation.

The algorithm output, for a given region during August 1987, was plotted on a Cartesian grid with cumulative percent on the vertical axis and CLW amount (kg/m^2) on the horizontal axis (Figs. 42 and 43). Together, the four graphs give some insight into the distribution and variability of CLW on a global scale.

The high latitude box (Fig. 42) indicates that approximately 30 % of the retrieved CLW values are negative. Negative CLW values are not possible. By definition, in clear skies, CLW equals zero. Colton and Poe (1994) identified the problem of retrieving negative CLW values in clear or nearly clear skies (clear meaning cloud free) as inherent in this algorithm.

Two possible reasons for this discrepancy exist. First, the algorithm is overestimating the contribution of water vapor to the retrieval. Second, there is noise in the observations on the order of $.05 \text{ kg/m}^2$ (Table 3) which is within the range of the resulting negative values. In either case, it is reasonable to assign a value of zero to all negative retrievals and simply state that this region experienced clear skies approximately 30 % of the time during August 1987.

This graph also displays a median CLW value of $.05 \text{ kg/m}^2$. Since this median value is within the noise of the retrievals, the observations are consistent with the skies being clear more than 50 % of the time.

Finally, the variability of CLW is a function of the plotted slopes. The steeper the slope, the less the variability. The slopes of the high latitude, midlatitude, and tropical boxes are similar; they all show relatively high CLW variability compared to the subtropical box (Fig. 43). As mentioned in previous chapters, the high CLW variability of the midlatitudes is directly attributable to transient extratropical cyclones.

The midlatitude box (Fig. 42) shows a slightly higher median CLW value of $.07 \text{ kg/m}^2$. The variation in the zero crossings suggest that there is approximately a $\pm .03 \text{ kg/m}^2$ latitudinal shift in the calibration. However, with the exception of the ITCZ

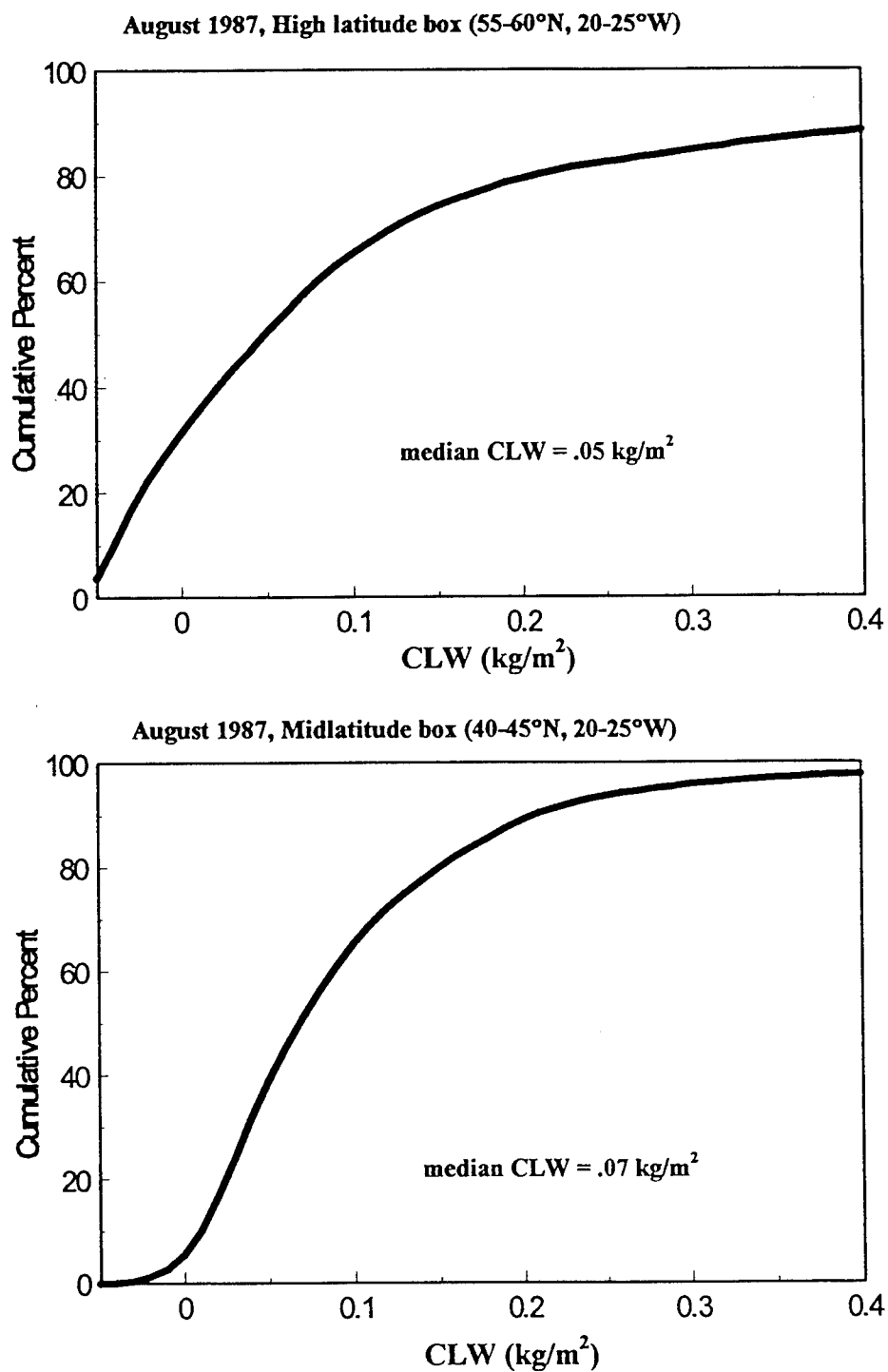


FIG. 42. Regional cloud liquid water distributions (amount of CLW vs. percent of time found) in a high latitude box (top) and midlatitude box (bottom) in August 1987.

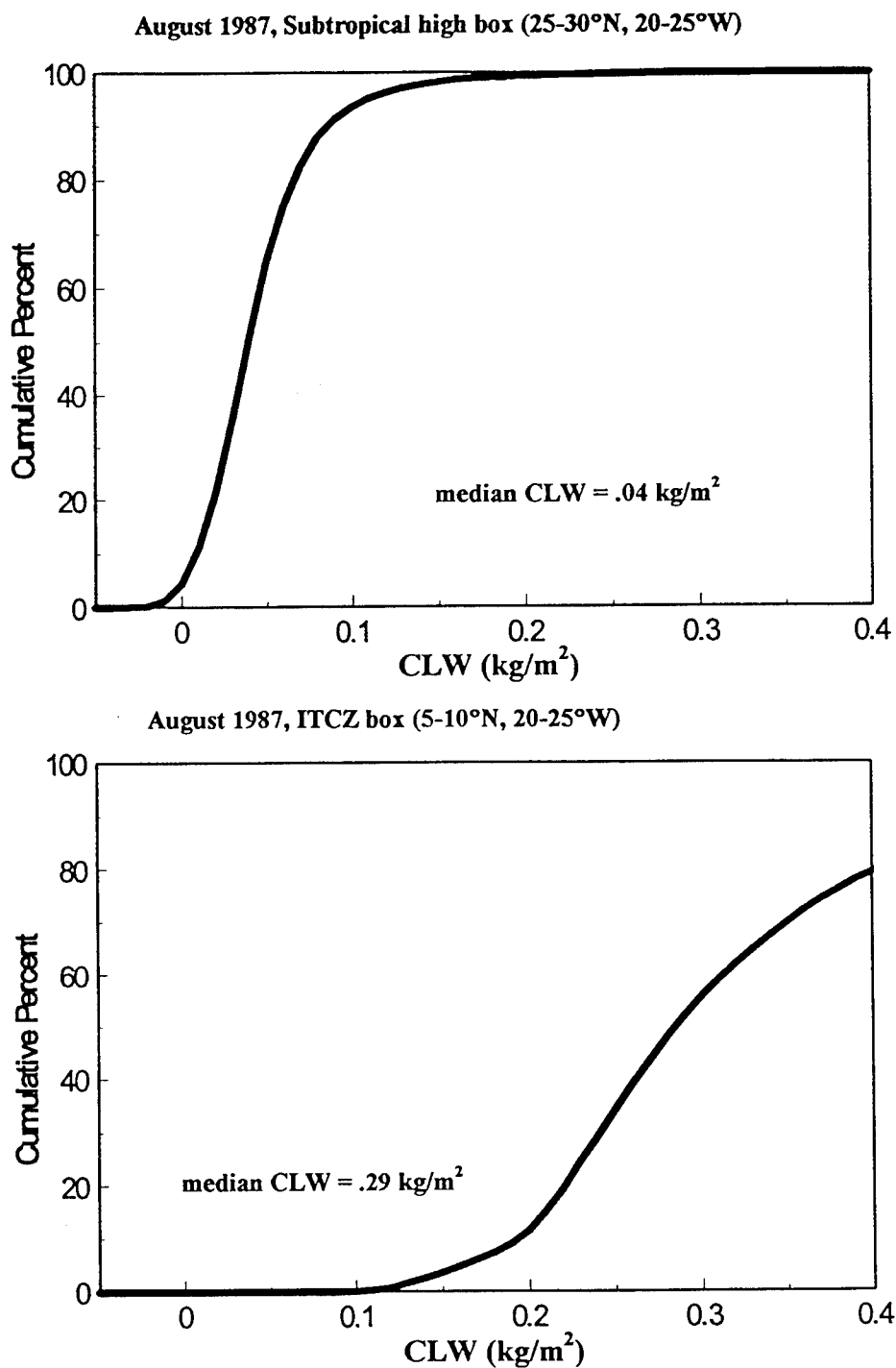


FIG. 43. Regional cloud liquid water distributions (amount of CLW vs. percent of time found) in a subtropical high box (top) and a tropical box (bottom) in August 1987.

box, all remaining regions are consistent with a relatively high percentage (up to 50% in some cases) of clear sky. Regions with extremely thin clouds or CLW values $< .03 \text{ kg/m}^2$ can be considered clear sky for practical purposes.

The subtropical high box (Fig. 43) has a mean CLW value similar to the high latitude box but possesses less variability . Applying the $.03 \text{ kg/m}^2$ criterion, over 30% of this box's retrieval profile can be associated with clear skies. This statistic is reasonable since this region is dominated by strong subsidence which inhibits cloud development.

The ITCZ box (Fig. 43) contains the highest amounts of CLW with a median value of $.29 \text{ kg/m}^2$. This box's relatively high median value is a result of the persistent and extensive deep convective clouds associated with the tropics. However, the median value should probably be closer to $.17 \text{ kg/m}^2$ owing to the apparent positive bias seen in the CLW distribution. This bias is another example of the algorithm's inability to properly account for the effect of water vapor on atmospheric opacity.

The branch separation method is not completely effective in the tropics. Taking into account the $.12 \text{ kg/m}^2$ positive bias, nearly 40 % of the retrieved CLW values exceed $.25 \text{ kg/m}^2$ which is normally associated with the cutoff between precipitating and nonprecipitating clouds (Wilheit, personal communication). This CLW value corresponds to an atmospheric opacity produced by approximately a 0.5 mm/hr rain rate.

This highlights a shortcoming with the branch separation method: even though observations reside in the absorption branch, small, precipitation-sized hydrometeors contribute to the brightness temperature through absorption and emission. The T_B 85 observations which are suspect are those with ΔT_B 's $< 10 \text{ K}$ where atmospheric opacity is greatest.

Finally, it is of interest to quantify (at least approximately) the magnitude of the CLW effect on the ΔT_B 85 sensitivity distributions. For example, given a typical

midlatitude CLW value of 0.07 kg/m^2 (reference Fig. 42), we can quantify the reduction in the ΔT_B value as compared to a perfectly clear (no CLW or PW) sky.

The two-component RTM (Fig. 7) is used as the basis for the calculations (i.e., cloud temperature = 250 K, $\theta = 53.1^\circ$, etc.). For a perfectly clear sky ($\tau = 0$), the ΔT_B value is 94.15 K. After introducing the 0.07 kg/m^2 of CLW, and remembering to compute for a two-way pass through the atmosphere, the optical depth is .230 which equates to a transmissivity of 0.7942 (ΔT_B value of 74.77 K). Therefore, CLW reduces the ΔT_B by a factor of approximately 1.26.

Next, the all-observation curve for the midlatitude box in figure 41 (which corresponds to the midlatitude box in fig. 42) is extrapolated to find the ΔT_B value at the zeroth percentile (38 K). This allows us to compare the mean value (28 K) of this curve against its clear sky value (38 K). Multiplying the transmissivity with the extrapolated value (i.e., $0.7942 * 38$), yields a ΔT_B of 30.18 K which allows us to quantify the CLW's contribution to the overall reduction in polarization difference.

This implies that the reduction in the polarization difference due to the contribution of CLW is approximately 93% ($28/30.18$) of the total. Therefore, in the midlatitudes, on average, it is reasonable to infer that clouds account for over 90% of the variability of atmospheric opacity (at least during periods of relatively transparent atmospheric conditions).

The above procedure was repeated for the subtropical high box using 0.04 kg/m^2 CLW. The results indicate that the CLW contribution to the reduction in the polarization difference is approximately 99% of the total. Therefore, in the subtropics, on average, it is reasonable to infer that the clouds account for nearly all the atmospheric opacity.

Three of the four boxes displaying CLW distributions (Figs. 42 and 43) indicate a slight bias towards negative CLW values on the order of .005 to .05 kg/m^2 . This implies that the Alshouse et al. algorithm is undercorrecting for the water vapor contribution. However, the fourth box (ITCZ), displays a fairly large positive bias (approximately .12 kg/m^2) which implies the algorithm is overcorrecting for the water

vapor in the tropical regions. Therefore, if the bias ($.12 \text{ kg/m}^2$) is subtracted from the median value ($.29 \text{ kg/m}^2$), and the new median CLW value of $.17 \text{ kg/m}^2$ is used, the results are then in close agreement with the first two boxes. Specifically, clouds account for nearly all the atmospheric opacity in the tropics as well as the other regions.

CHAPTER VII

CONCLUSIONS AND RECOMMENDATIONS

1. Sensitivity distribution results

The global sensitivity distributions reveal that Nelkin's algorithms can be used 75-90 % of the time over the majority of the Earth's oceans. This result varies depending on the particular algorithm in question.

The winter hemisphere, when compared to the summer hemisphere, provides better results. This is due to generally dryer and clearer atmospheric conditions associated with large scale subsidence. In this case, the algorithms applicability reaches 90 %.

The sensitivity distributions are affected slightly (approximately 10 K) when the FOV is increased (resolution decreased) by a factor of 8. The results of the FOV experiment suggest that the applicability of the algorithms which retrieve the ocean surface parameters SST and WS, is not altered significantly. Employing a ΔT_B lower threshold of 10 K on these algorithms results in a decrease in applicability to a maximum of 75 % over approximately half the Earth's oceans.

Conclusions derived from the algorithms can be deemed unreliable under various atmospheric or ocean surface conditions. Certain weather regimes render the atmosphere sufficiently opaque to derive unreliable results. These weather regimes are characteristically associated with deep convective clouds with heavy and persistent rain. Their locations are seasonally and latitudinally dependent.

A prime example of the importance the time of year plays on the applicability of the new algorithms is the monsoon region. During the Summer, algorithms cannot be expected to perform reliably more than 50 % of the time whereas during the Winter, applicability reaches 90 %.

The ITCZ and SPCZ are good examples of regions where seasonal and latitudinal factors significantly affect the global sensitivity distributions. It is in these regions

where robust algorithms will have to be selected at the price of increased uncertainty in the retrievals. As with the monsoon region, depending on the location and intensity of the ITCZ and SPCZ, which are seasonal considerations, the algorithms cannot be expected to give highly reliable results more than 50 % of the time.

Finally, any region containing sea ice (i.e. Hudson Bay or the Sea of Okhotsk) cannot be used by any of the 4-parameter algorithms. Fortunately, the formation of sea ice is seasonally dependent and is limited to relatively small areas.

2. Cloud liquid water distribution results

CLW distributions vary with latitude. The statistics shown in Table 4 are a compilation of the regional outputs derived from the Alishouse et al. (1990) algorithm for the North Atlantic during August 1987. Interestingly, the data are divided into similar climate zones as found in Table 2.

The median CLW values are either close to or buried within the noise of the observations ($.05 \text{ kg/m}^2$). Even with this limitation, some knowledge as to the relative magnitude of the amount of CLW can be gained.

3. Recommendations for future work

CLW retrievals within the tropics, especially the ITCZ and SPCZ, contain raining events. This is true even after the application of the branch separation method. One possible way to make the algorithms more robust would be to eliminate T_B 85 observations (and their associated low channel observations) when the ΔT_B value is less than 10 K. Although this might lower the applicability of the algorithms this would probably be offset by an increased accuracy in the retrieval amounts. A more detailed climatology of the tropics would need to be accomplished prior to obtaining meaningful results.

Additional future work should concentrate on the results obtained from the global sensitivity distributions. The idea would be to create a decision tree approach for

TABLE 4. Typical global cloud liquid water values. Climate zones based on analysis of August 1987 regional CLW distributions over the North Atlantic.

Climate Zones	Latitude Range (Degrees)	Median Cloud Liquid Water (kg/m ²)
High Latitudes	50-60	.04 - .05
Midlatitudes	30-50	.07 - .10
Subtropics	20-30	.04 - .05
Tropics (excluding ITCZ)	0-20	.12 - .22

when to select a specific algorithm depending on its sensitivity to atmospheric opacity. Data could then be input into these algorithms, which are designed to compute PW and other geophysical parameters, and their output compared against ground truth (i.e. radiosonde water vapor profiles) to determine their validity.

REFERENCES

- Alishouse, J. C., J. B. Snider, E. R. Westwater, C. T. Swift, C. S. Ruf, S. A. Snyder, J. Vongsathorn, and R. R. Ferraro, 1990: Determination of cloud liquid water content using the SSM/I. *IEEE Transactions on Geoscience and Remote Sensing*, **28**, 817-821.
- Colton, M. C., and G. A. Poe, 1994: Shared processing program, defense meteorological satellite program, Special Sensor Microwave/Imager Algorithm Symposium, 8-10 June 1993. *Bull. Amer. Meteor. Soc.*, **75**, 1663-1669.
- Crowley, T. J., and G. R. North, 1991: *Paleoclimatology*. Oxford University Press, 339 pp.
- Filiberti, M. A., L. Eymard, and B. Urban, 1994: Assimilation of satellite precipitable water in a meteorological forecast model. *Mon. Weather Rev.*, **122**, 486-506.
- Goodberlet, M. A., C. T. Swift, and J. C. Wilkerson, 1989: Remote sensing of ocean surface winds with the Special Sensor Microwave/Imager. *J. Geophys. Res.*, **94**, 14547-14555.
- Greenwald, T. J., G. L. Stephens, T. H. Vonder Haar, and D. L. Jackson, 1993: A physical retrieval of cloud liquid water over the global oceans using Special Sensor Microwave/Imager (SSM/I) observations. *J. Geophys. Res.*, **98**, 18471-18488.
- Griffiths, D. J., 1989: *Introduction to Electromagnetics (2nd Ed.)*. Prentice Hall, 532 pp.
- Gunn, K. L. S., and T. W. R. East, 1954: The microwave properties of precipitation particles. *Quart. J. Roy. Meteor.*, **80**, 522-545.
- Hollinger, J., R. Lo, G. Poe, R. Savage, and J. Peirce, 1987: *Special Sensor Microwave/Imager User's Guide*, Naval Res. Lab., Washington, D.C., 120 pp.
- Nelkin, E. J., 1992: Implications of SSM/I observations for retrievals of ocean surface and marine atmospheric parameters. M.S. thesis, Univ. of Texas A&M, 95 pp.
- Prabhakara, C., G. Dalu, G. L. Liberti, J. J. Nucciarone, and R. Suhasini, 1992: Rainfall estimation over oceans from SMMR and SSM/I microwave data. *J. Appl. Meteor.*, **31**, 532-552.

Vincent, D. G., 1994: The South Pacific Convergence Zone (SPCZ): A review. *J. Appl. Meteor.*, **31**, 1949-1970.

Wallace, J. M., and P. V. Hobbs, 1977: *Atmospheric Science an Introductory Survey*. Academic Press, Inc., 467 pp.

Wentz, F. J., 1988: *User's Manual - SSM/I Antenna Temperature Tapes*. RSS Technical Report 032588, 23 pp. (Personal Collection, J.F. Polander).

_____, 1992: Measurement of oceanic wind vector using satellite microwave radiometers. *IEEE Transactions on Geoscience and Remote Sensing*, **30**, 960-971.

Wilheit, T. T., 1979: A model for the microwave emissivity of the ocean's surface as a function of wind speed. *IEEE Transactions on Geoscience Electronics*, **17**, 244-249.

_____, and A. T. C. Chang, 1980: An algorithm for retrieval of ocean surface and atmospheric parameters from the observations of the scanning multichannel microwave radiometer. *Radio Sci.*, **15**, 525-544.

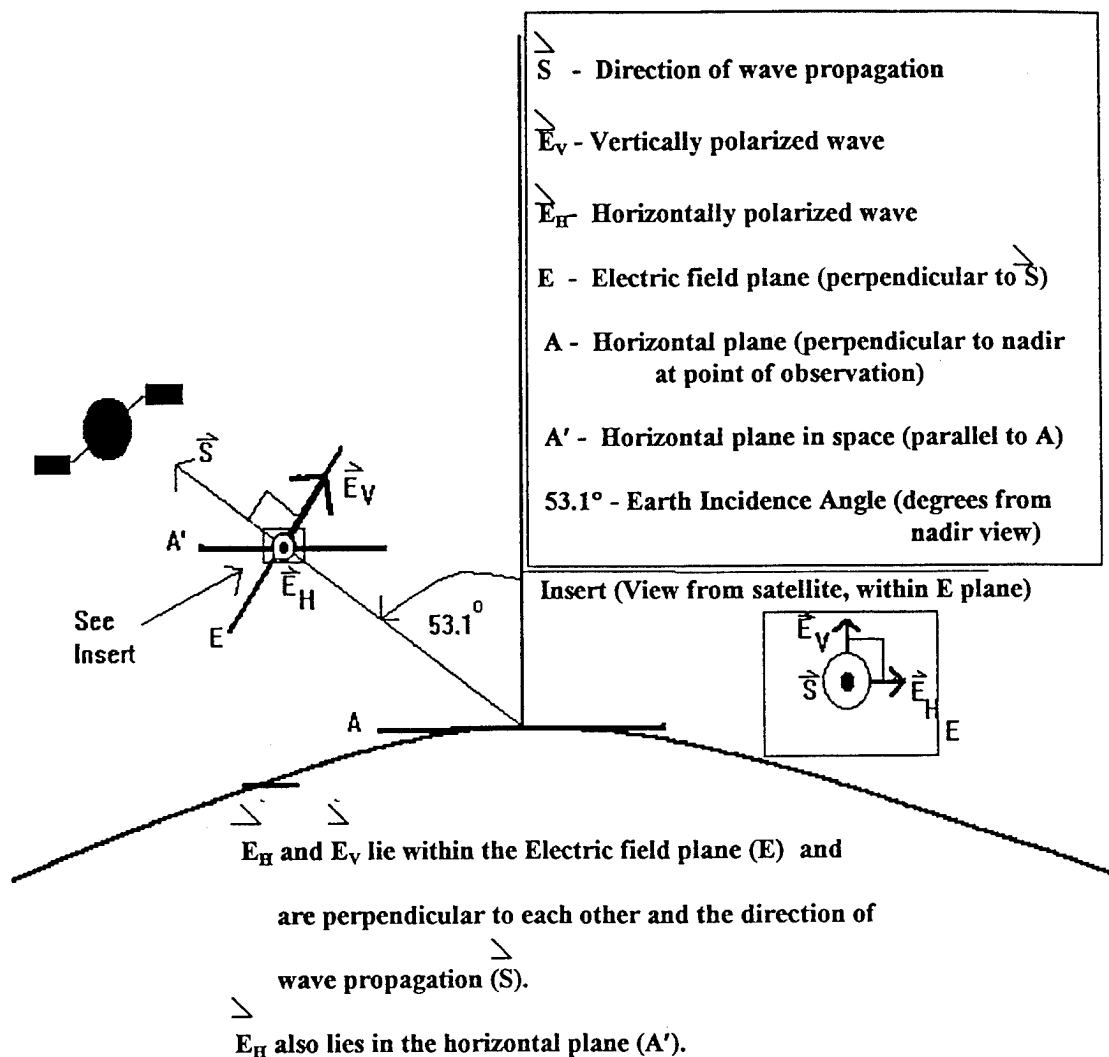
_____, A. T. C. Chang, and L. S. Chiu, 1991: Retrieval of monthly rainfall indices from microwave radiometric measurements using probability distribution functions. *J. Atmos. Oceanic Technol.*, **8**, 118-136.

_____, R. Adler, S. Avery, E. Barrett, P. Bauer, W. Berg, A. Chang, J. Ferriday, N. Grody, S. Goodman, C. Kidd, D. Kniveton, C. Kummerow, A. Mugnai, W. Olson, G. Petty, A. Shibata, and E. Smith, 1994: Algorithms for the retrieval of rainfall from passive microwave measurements. *Remote Sensing Reviews*, **11**, 163-194.

APPENDIX A

SCHEMATIC OF THE SSM/T'S

CHANNEL/FREQUENCY POLARIZATIONS



APPENDIX B

LIST OF ACRONYMS

CLW	- Cloud Liquid Water
ECMWF	- European Center for Medium-range Weather Forecasts
EOS	- Earth Observing System
ERT	- Equation of Radiative Transfer
FOV	- Field Of View
ITCZ	- InterTropical Convergence Zone
METOP	- Meteorological Operational
MIMR	- Multi-frequency Imaging Microwave Radiometer
NCAR	- National Center for Atmospheric Research
PW	- Precipitable Water
RTM	- Radiative Transfer Model
SPCZ	- South Pacific Convergence Zone
SSM/I	- Special Sensor Microwave/Imager
SST	- Sea Surface Temperature
T _B	- Brightness Temperature
WS	- Wind Speed

VITA

John Francis Polander, was born in Cleveland, Ohio and attended Cleveland parochial schools. He enlisted in the United States Air Force in June 1978. During his first ten years of service, he was stationed in Ohio and Stuttgart Germany.

While assigned as Non-commissioned Officer-In-Charge of the ROTC detachment at Ohio University, he applied and was accepted into the Airman's Education Commissioning Program.

Polander graduated Cum Laude with a Bachelor of Science degree in Meteorology in December 1989 from Texas A&M University. He subsequently was commissioned a Second Lieutenant in the United States Air Force.

His first assignment as an officer was to Mildenhall Royal Air Force Base, United Kingdom as a Wing Weather Officer. In June 1993, he applied and was accepted into the Air Force Institute of Technology Master's program and sent to Texas A&M University. He became a member of the Microwave Remote Sensing Group and focused his research on developing a rain filter using the SSM/I's 85 GHz channels. Polander was promoted to the rank of Captain in April 1994.

Polander married the former Miss Cynthia Louise Kravec in July 1983. They have two daughters: Emily, born 23 August 1987 and Ellyn, born 1 December 1992.

Correspondence during transitional periods may be sent to: c/o Jeanne Polander, 12313 Worthington Ave., Cleveland, OH 44111.